Control-oriented Modeling of an Air-breathing Hypersonic Vehicle

Praneeth Reddy Sudalagunta

Dissertation submitted to the Faculty of the
Virginia Polytechnic Institute and State University
in partial fulfillment of the requirements for the degree of

Doctor of Philosophy
in
Aerospace Engineering

Cornel Sultan, Chair
Pradeep Raj, Co-chair
Rakesh K. Kapania
Layne T. Watson

July 14, 2016
Blacksburg, Virginia

Keywords: Air-breathing hypersonic vehicles, Control-oriented modeling, Aeroelasticity.

Control-oriented Modeling of an Air-breathing Hypersonic Vehicle

Praneeth Reddy Sudalagunta

(ABSTRACT)

Design and development of future high speed aircraft require the use of advanced modeling tools early on in the design phase to study and analyze complex aeroelastic, thermoelastic, and aerothermal interactions. This phase, commonly referred to as the conceptual design phase, involves using first principle based analytical models to obtain a practical starting point for the preliminary and detailed design phases. These analytical models are expected to, firstly, capture the effect of complex interactions between various subsystems using basic physics, and secondly, minimize computational costs. The size of a typical air-breathing hypersonic vehicle can vary anywhere between 12 ft, like the NASA X-43A, to 100 ft, like the NASP demonstrator vehicle. On the other hand, the performance expectations can vary anywhere between cruising at Mach 5 @ $85,000$ ft to Mach 10 @ $110,000$ ft. Reduction of computational costs is essential to efficiently sort through such a vast design space, while capturing the various complex interactions between subsystems has shown to improve accuracy of the design estimates. This motivates the need to develop modelling tools using first principle based analytical models with "needed" fidelity, where fidelity refers to the extent of interactions captured.

With the advent of multidisciplinary design optimization tools, the need for an integrated modelling and analysis environment for high speed aircraft has increased substantially over the past two decades. The ever growing increase in performance expectations has made the traditional design approach of optimize first, integrate later obsolete. Designing a closed-loop control system for an aircraft might prove to be a difficult task with a geometry that yields an optimal (L/D) ratio, a structure with optimal material properties, and a propulsion system with maximum thrust-weight ratio. With all the subsystems already optimized, there is very little freedom for control designers to achieve their high performance goals. Integrated design methodologies focus on optimizing the overall design, as opposed to individual subsystems. Control-oriented modelling is an approach that involves making appropriate assumptions while modelling various subsystems in order to facilitate the inclusion of control design during the conceptual design phase.

Due to their high lift-to-drag ratio and low operational costs, air-breathing hypersonic vehicles have spurred some interest in the field of high speed aircraft design over the last few decades. Modeling aeroelastic effects for such an aircraft is challenging due to its tightly integrated airframe and propulsion system that leads to significant deflections in the thrust vector caused by flexing of the airframe under extreme aerodynamic and thermal loads. These changes in the orientation of the thrust vector in turn introduce low frequency oscillations in the flight path angle, which make control system design a challenging task. Inclusion of such effects in the vehicle dynamics model to develop accurate control laws is an important part of control-oriented modeling. The air-breathing hypersonic vehicle considered here is assumed to be a thin-walled structure, where deformations due to axial, bending, shear, and torsion are modeled using the six independent displacements of a rigid cross section. Free vibration mode shapes are computed accurately using a novel scheme that uses estimates of natural frequency from the Ritz method as initial guesses to solve the governing equations using SUPORE, a two-point boundary value problem solver. A variational approach involving Hamilton's principle of least action is employed to derive the second order nonlin-

ear equations of motion for the flexible aircraft. These nonlinear equations of motion are then linearized about a given cruise condition, modal analysis carried out on the linearized system, and the coupling between various significant modes studied. Further, open-loop stability analysis in time domain is conducted.

This material is based on research sponsored by Air Force Research Laboratory under agreement number FA8650-09-2-3938. The U.S. Government is authorized to reproduce and distribute reprints for Governmental purposes not withstanding any copyright notation thereon.

The views and conclusions contained herein are those of the authors and should not be interpreted as necessarily representing the official policies or endorsements, either expressed or implied, of Air Force Research Laboratory or the U.S. Government.

Acknowledgments

I would like to convey my heartfelt thanks and sincere gratitude to my advisor, **Dr. Cornel Sultan**, for his endless support and constant motivation over the past four years. I've grown many-fold as a researcher since he had taken me under his wing and helped hone skills that I'm sure will help me in my career going forward. I'd like to thank my co-advisor **Dr. Pradeep Raj** for patiently engaging me in several brain storming sessions that helped me get past numerous road blocks. His suggestion of conducting sanity checks at every juncture has helped me verify most of the results presented in my dissertation. I am grateful to **Dr. Rakesh Kapania** for constantly challenging me to venture into unknown territories, and for being the beacon and showing the way when I get lost. This section woiuld be incomplete without thanking **Dr. Layne T. Watson**, who has patiently reviewed all my publications and in the process taught me writing well rounded technical articles. Apart from being an incredible source of knowledge, my advisory committee has been a constant source of support throughout this endeavor. Most of the results published in this thesis would not have been possible without your valuable feedback. This experience has not only helped me learn how to better conduct research but myself in a professional environment. I can't thank you enough for your guidance.

I will forever be indebted to my loving and caring parents for their endless support and encouragement they have given me over the years. My life in Blacksburg would be incomplete without the many friends I've made, and the memories I'll be carrying with me for the rest of my life. You've helped me make a home away from home and been that support when I needed someone to lean on. Although, we never worked together I've always had my research group with my whenever I needed their help. Last but never the least, I'd like to thank the beautiful town of Blacksburg for cradling me in it's love.

Contents

List of Figures

List of Tables

Chapter 1

Introduction

Air-breathing hypersonic vehicle (AHV) technology finds potential applications in single stage to orbit (SSTO)/two stage to orbit (TSTO) space missions and long range cruise missions. The advancement in aircraft structures and propulsion technology has fueled interest in developing a full scale air-breathing hypersonic vehicle. Although AHVs offer attractive benefits such as making low-earth orbit space missions reliable and affordable,[59] long range cruise missions cheaper,[44] high speed commercial air travel possible,[50] etc., they pose myriad technological challenges in the form of aerothermoelastic effects,[27] integrated airframe and propulsion system,[7] and non minimum phase behaviour of the flight path angle.[20]

An air-breathing hypersonic vehicle is a long, slender lifting body with a sharp leading edge for drag reduction.[34] Such an aircraft would experience aerodynamic heating at the stagnation point, in the nacelle region close to the combustion chamber, and along the aft body panel housing the exhaust nozzle.[7] This would influence the associated flow field over the aircraft and material properties of the structure. Coupling between the unsteady aerodynamics, thermodynamics, and structural dynamics will result in aerothermoelastic effects. Studying such effects requires a trade-off between using simple analytical methods against obtaining reduced order models from high fidelity computational tools.[33]

Figure 1.1 depicts the coupling that exists between various subsystems of an air-breathing hypersonic vehicle at several stages. The AHV model is divided broadly into four subsystems, based on their function, namely structural dynamics, propulsion system, aerothermodynamics, and control system. Each of these subsystems interact with two other subsystems that result in primary coupling effects. The coupling between the structure and control system leads to servoelastic effects, coupling between the structure and the propulsion system is a consequence of the waverider configuration that results in a tightly integrated airframe and propulsion system, coupling between the aerothermodynamic flow field and propulsion system leads to aeropropulsive effects, and coupling between the aerothermodynamic flow field and the control system results in lowering of control authority. These primary effects interact with eachother and give rise to secondary effects like nonminimum phase behavior, aeroservoelasticity, aerothermoelasticity, and low frequency oscillations in

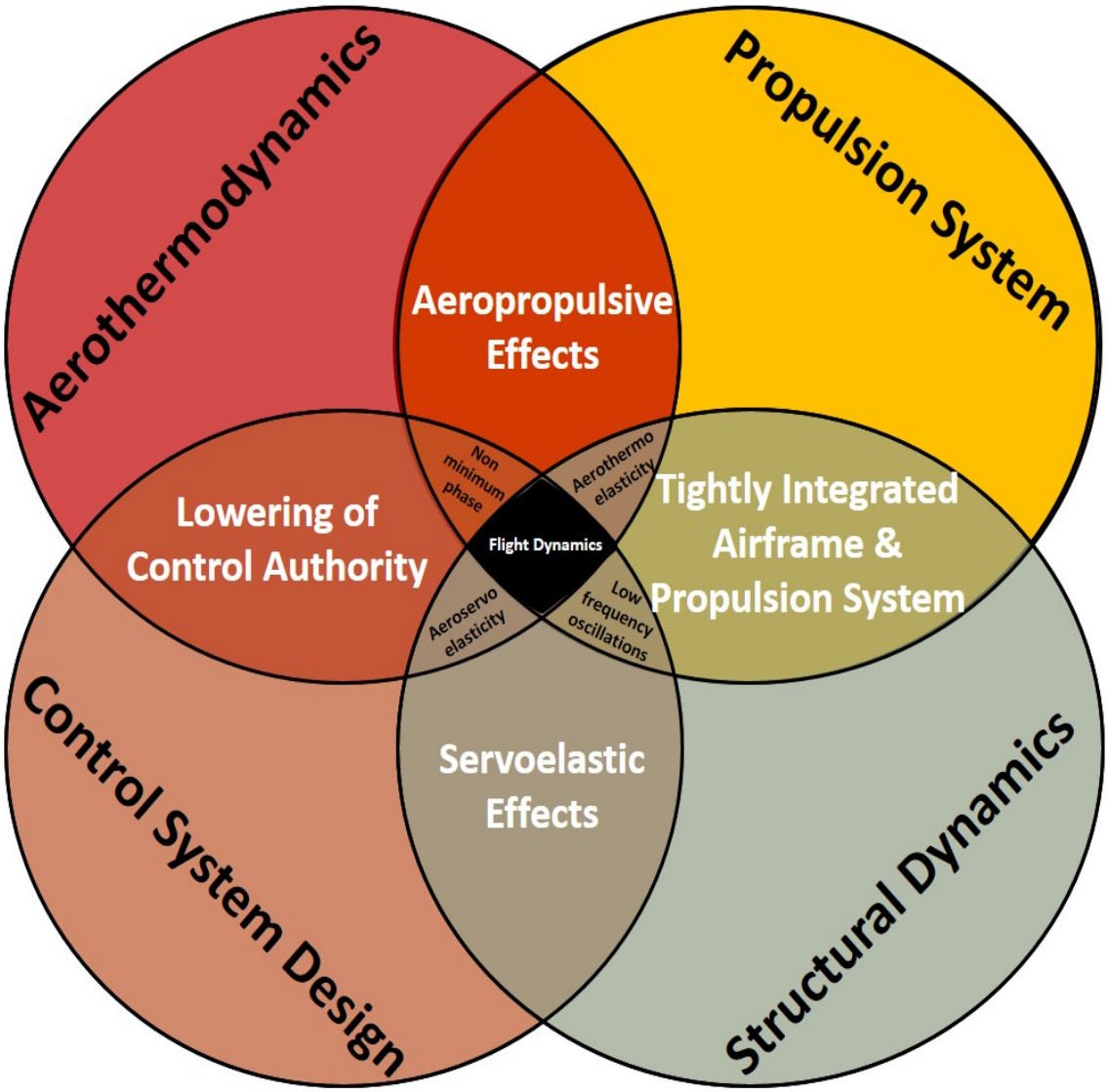

Figure 1.1: AHV coupling between subsystems.

the dynamics of the vehicle. At the center of these four secondary effects rests the model that describes the dynamics of an air-breathing hypersonic vehicle.

1.1 History of Air-breathing Hypersonic Vehicles

The vision to design the first hypersonic vehicle dates back to the end of World War I. It wasn't until the late 1930's did these ideas, which at the time existed only in theory, were put to practice through experimental work. The first experiments were attributed to the development of a pre-World War II German A-series winged aircraft housing a V-2 rocket capable of reaching speeds beyond Mach 4. The modern day air-breathing hypersonic vehicle wasn't conceptualized until the early 1960s, which was fueled by the success of some of the early X-series aircraft developed in United States of America. The subsequent years would see the hypersonic vehicle's flight envelope extended upto Mach 14 through a joint U.S. Air Force and NASA program called ASSET (Aerothermodynamic/elastic Structural Systems Environmental Tests). These flight tests were carried out on aircraft with waverider configuration, however, the propulsion sytem was still rocket based. The hypersonic vehicle concept evolved into using a supersonic scramjet engine, as opposed to the conventional rocket propulsion in lieu of significant fuel savings and weight reduction by completely losing the oxidizer. The projected performance benfefits included, not restricted to, a significant increase in range and endurance, reduction in fuel consumed, making the aircraft reusable, potential to land and take-off like conventional aircraft, reduction in time spent on pre-flight preparations, etc. The benefits of using a scramjet engine were compelling, at the same time they came with their fair share of challenges. The only viable location for the scramjet engine is in the underbelly of the aircraft, this resulted in a tightly integrated airframe and propulsion system. Moreover, the inflow into the engine will be influenced by the forebody flexing effectively coupling the aerothermodynamics, structural dynamics, and propulsion system. The rapid advancement seen in developing a full scale air-breathing hypersonic vehicle in the 1960s was slowed down by two decades of research and experiments that progressively seemed more and more daunting, pushing scramjet powered hypersonic flight far from reality. In order to tackle challenges posed by the tightly integrated airframe and propulsion system, also known as aeropropulsive effects, another joint U.S. Air Force and NASA program called NASP (National Aerospace Plane) was initiated in the early 90s. This period saw the emergence of several mathematical models that dealt with varying levels of complexity in order to model the dynamics of a single stage to orbit (SSTO) hypersonic reentry vehicle. This program ended in the year 1995 due to lack of funding, however, the aeropropulsive models developed would be used later on in the Hyper-X program by NASA. The mission statement of this initiative was to incrementally achieve technological progress, as opposed to developing a full-scale vehicle. The prototypical Hyper-X demonstrator vehicle was 12 feet long and would later on be scaled to a 200 foot long full-scale aircraft. The focus of this period was to tackle several control challenges that seemed too far fetched before. Sub-

sequent efforts in this area were made in developing a two stage to orbit reusable launch vehicle for low-earth orbit space missions by NASA as part of the Hyper-X program, and a longe range high altitude hypersonic cruise vehicle by the U.S. Air Force as part of the HyTech program.

1.2 Review of Literature

Since it's conception the AHV design cycle has gone through several reboots and among the myriad challenges perceived every initiative has focussed on a different challenge. This has resulted in an opulence of literature on the topic, but at the same time left glaring voids between decades of rebooting. In the 1960s, the focus was on developing a full scale rocket powered waverider-like launch vehicle. While the 1970s, saw the rise of scramjet engines and were destined to replace the rocket propulsion system. The scramjet program, in itself, was a very ambitious venture taking two more decades to master it. Once, the scarmjets were seen as a viable option, the myriad challenges they bring with them had to be confronted. In the 1990s, the first of those challenges, called the aeropropulsive effects were addressed. However, the structural modeling was restricted to a simple free-free Euler-Bernoulli beam, and the aerodynamics to that of Newtonian impact theory. The AHV modeling saw a major upgrade in the past two decades, where the aerodynamics modeling evolved from Newtonian impact theory to oblique shock theory to including viscous effects, while the propulsion system modeling evolved from a constant area frictionless duct with heat addition to a dual-mode scramjet engine. The available literature of interest pertaining to the design of AHVs can be broadly classified into three mutually exclusive groups: studies on aerothermoelastic effects, vehicle dynamics modeling, and control system design.

1.2.1 Aerothermoelastic Studies

Studies on aerothermoelastic effects date back to the early 1960s from the rocket powered era. As the focus shifted towards scramjet propulsion, the nature of these effects changed drastically requiring a complete reboot of the aerothermoelastic modeling efforts. Recent efforts by McNamara et. al.[33,34] explored the effects of coupling between unsteady hypersonic aerodynamics and thermodynamics on the structure. Klock et. al.[27] carried out simulations of the aerothermoelastic effects on the longitudinal dynamics of the flexible aircraft. Culler et. al.[11] extended the nonlinear longitudinal dynamics model by Bolender et. al.[7] to acount for the varying effects of mass and average temperature along the trajectory. Notable studies on the effect of aerothermoelasticity on control surface panels for flutter analysis include those by Yang et. al.,[8] Abbas et. al.,[1] and Nathan et. al.[17] Although each of these works contribute to a growing body of literature in theor own way, they consistently fall short of

providing control design worthy models.

1.2.2 Vehicle Dynamics Modeling

Most of the vehicle dynamics models developed in the past two decades are restricted to nonlinear ones describing the aircraft's behavior along the longitudinal direction. Early efforts by Chavez et. al.[9] account for flexibilty effects in the transverse direction and modeled aeropropulsive effects for the first time. Seminal works by Bolender et. al.[6,7] extended this body of work by advancing the aerodynamics model from Newtonian impact theory to oblique shock theory to including vicous effects. Torrez et. al.[54] furthered this work by improving the propulsion system modeling through dual mode scramjet engine. The focus then shifted to control-oriented modeling, where the modeling focus is to facilitate implemetation of efficient control laws.[10,16,44,57,58] The afforementioned works all consistently focus on studying the longitudinal dynamics of the vehicle, the only work that studies the impact of longitudinal, lateral, and directional dynamics is by Keshmiri et. al.[26] However, this work suffers from accounting for low-fidelity flexibilty effects. All efforts unanimously ignore high frequency effects, assuming them to be easily damped out during dynamics. We ackn owledge that this assumption needs to be verified by modeling them and studying the effects of these high frequency modes.

1.2.3 Control System Design

The Hyper-X program's test flights shed some light on the impending control challenges to be tackled in making hypersonic air-breathing flight a reality. Over the past two decades, control system modeling efforts for an air-breathing hypersonic vehicle range from treating the airframe as a rigid body, to modest introduction of the airframe's coupling effects, using a linearized hypersonic aerodynamics model, etc. Works by Fiorentini et. al.[18–20] focus on the nonminimum phase behavior of the aircraft, where they propose to use nonlinear control techniques to compensate for such behavior. Sigthorsson et. al.[47,48] use robust linear and nonlinear control techniques by taking only the first three fundamental modes of vibration into consideration.

The enormous body of literature developed so far despite being diverse leaves out some voids, like studying the effect of high frequency modes on the dynamics, modeling lateral and directional dynamics effects, implementing high fidelity structural modeling sccounting shear effects, etc. It can be seen that there is a need for a comprehensive approach with a computationally tractable, high fidelity model.

1.3 Proposed Model

An air-breathing hypersonic vehicle is characterized by an airframe tightly integrated with a scramjet propulsion system. The aerothermal loads cause relatively large deformations of the forebody that affect the air flow into the inlet, causing significant changes in both magnitude and orientation of the resulting thrust vector. The airframe is modeled as a thin-walled structure assuming that a plane section remains plane and not necessarily perpendicular to it's instantaneous axis taking into account axial, bending, shear, and torsional effects. Six independent displacements of a rigid cross section are used to describe the deformation at a given point on the vehicle making the free vibration problem one-dimensional. The deformation at a given point on the vehicle is expressed as a superposition of the first n significant modes, where each mode is expressed as the product of a mode shape function $\phi(x)$ and a modal coordinate $\eta(t)$. The free vibration problem is solved to compute the mode shapes for the first n significant modes, using the Ritz method to estimate natural frequencies for the first n modes as initial guesses for a two-point boundary value problem solver SUPORE, which solves the governing equations subject to appropriate boundary conditions to accurately compute the mode shapes of the vehicle. These mode shape functions are then integrated over the volume and used in the forced vibraton problem involving six rigid body modes and n flexible modes, measured with respect to an inertial ground frame of reference. The equations of motion for the forced vibration problem are derived using the principle of virtual work, where the virtual work due to applied (aerodynamic, gravitational, and control) forces is equated to the virtual work due to internal forces (inertial effects and elastic forces) using the Lagrangian approach. These form the nonlinear second order dynamics equations of motion for the flexible air-breathing hypersonic vehicle taking into account the interaction between aerodynamic, gravitational, control, inertial, and vibrational effects. The nonlinear equations of motion are then linearized about a given cruise condition to obtain the linearized dynamics model for cruise.

Chapter 2

Geometry of the Vehicle

The air-breathing hypersonic vehicle is assumed to have a long, wedge shaped forebody and a sharp leading edge that creates at the tip of the aircraft an oblique shock that is almost entirely swallowed by the engine inlet.[7] The lower fore body panel acts as a compression ramp for the scramjet engine housed in the under belly of the nacelle region as shown in Fig. 2.1. The aft body is also wedge shaped where its lower panel forms a part of the exhaust nozzle for the engine along which a shear layer is created between the exhaust gases and the adjacent free stream. Figure 2.1 presents the side view of a typical air-breathing hypersonic vehicle, where the line parallel to the nacelle and passing through the fore body tip is considered to be the longitudinal axis of the aircraft. The upper fore body panel extends the entire length of the aircraft with an angle of inclination τ_{1u} with respect to the longitudinal axis, while the lower fore body panel spans the length of the forebody L_f and makes an angle τ_{1l} with the axis. The panel of the lower nacelle region is parallel to the axis and has a length L_n. The lower aft body panel that forms a part of the exhaust nozzle stretches through the length of the aft body L_a and makes an angle τ_2 with the upper forebody panel.

Figure 2.2 shows the top view of the aircraft, where the upper panel is modeled as an isosceles trapezoid with a height equal to the length of the aircraft L, and base lengths equal to the width of the aircraft at the fore body tip and the aft body tip, $l_u(0)$ and $l_u(L)$ respectively. The figure also shows the location of the rudders and elevons located to the aft of the aircraft.

The cross section of an air-breathing hypersonic vehicle is shown in Fig. **??** where the section above the longitudinal axis is modeled as a rectangle and the section below the axis is modeled as an isosceles trapezium. The trapezoidal lower cross section derives from the requirement that a forebody compression ramp needs to be flat in the lateral direction as opposed to being curved. A curved lower cross section would create a shear layer across the forebody compression ramp (laterally) leading to nonuniform flow at the engine inlet. The length of the rectangular section $l_u(x_1)$ is the width of the upper panel of the aircraft at a distance x_1 from the fore body tip of the aircraft, while $l_f(x_1)$, the base of the trapezoidal section, is the width of the lower panel of the aircraft at x_1. The height of the rectangular

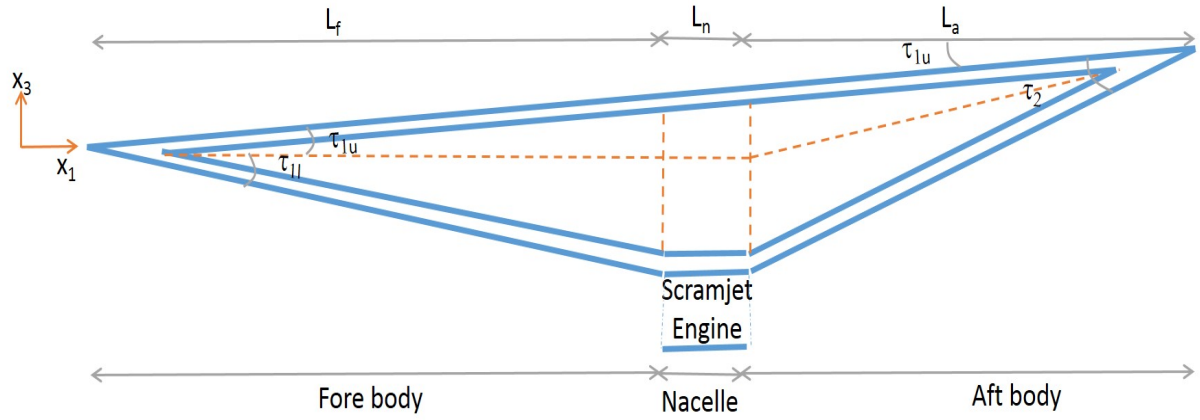

Figure 2.1: Side view of a typical air-breathing hypersonic vehicle (Figure not to scale)

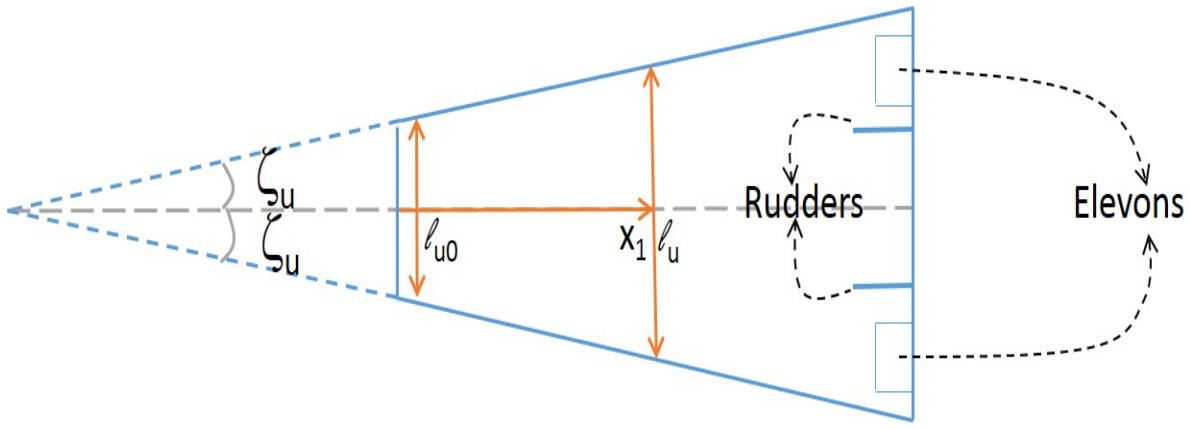

Figure 2.2: Top view of a typical air-breathing hypersonic vehicle (Figure not to scale)

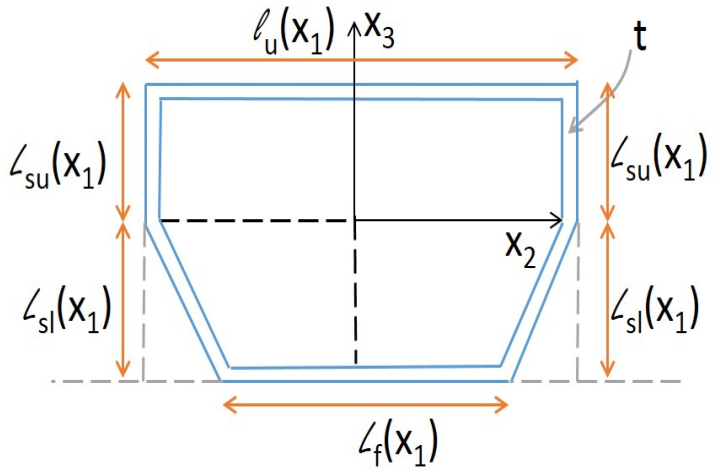

Figure 2.3: Cross section of a typical air-breathing hypersonic vehicle (Figure not to scale)

section $l_{su}(x_1)$ and the height of the trapezoidal section $l_{sl}(x_1)$ are the heights of the upper and lower side panels of the aircraft at a distance x_1 from the forebody tip of the aircraft. It is important to note that $l_{su}(x_1)$ and $l_{sl}(x_1)$ are perpendicular distances from the longitudinal axis (horizontal dotted line, seen in Fig. 2.1) to the upper and lower panels of the aircraft at a distance x_1 from the tip of the aircraft. Using geometry from Fig. 2.1 yields

$$l_{su}(x_1) = \begin{cases} x_1 \tan \tau_{1u}, & 0 \leq x_1 \leq L_f + L_n, \\ (L - x_1)\left(\frac{L_f + L_n}{L_a}\right) \tan \tau_{1u}, & L_f + L_n \leq x_1 \leq L, \end{cases} \tag{2.1}$$

$$l_{sl}(x_1) = \begin{cases} x_1 \tan \tau_{1l}, & 0 \leq x_1 \leq L_f, \\ L_f \tan \tau_{1l}, & L_f \leq x_1 \leq L_f + L_n, \\ (L - x_1)\left(\tan(\tau_2 + \tau_{1u}) - \frac{L}{L_a} \tan \tau_{1u}\right), & L_f + L_n \leq x_1 \leq L. \end{cases} \tag{2.2}$$

Similarly, $l_u(x_1)$ and $l_f(x_1)$ can be derived geometrically using the top view and the bottom view (similar to top view) of the AHV. Using geometry from Fig. 2.3

$$l_u(x_1) = l_{u0} + 2x_1 \tan \zeta_u, \tag{2.3}$$

$$l_f(x_1) = l_{f0} + 2x_1 \tan \zeta_f. \tag{2.4}$$

Table 2.1 lists all the geometric constants required to describe the complete geometry of the AHV, shown in Fig. 2.4.

Table 2.1: Table of geometric constants.

Constant	Value
L_f	47 ft
L_n	20 ft
L_a	33 ft
L	100 ft
t	0.285 in
l_{u0}	17.36 ft
l_{f0}	13.19 ft
τ_{1u}	3^o
τ_{1l}	6.2^o
τ_2	14.41^o
ζ_u	6.93^o
ζ_f	4.17^o

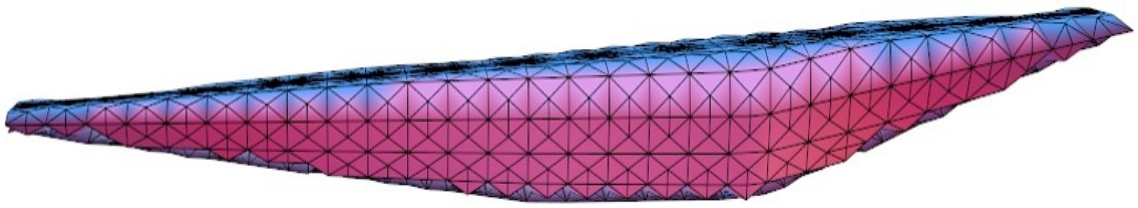

Figure 2.4: Air-breathing hypersonic vehicle geometry reconstructed from the equations and constants listed in Table 2.1

Phase I:

Computing Free Vibration Mode Shapes

Chapter 3

Introduction - Free Vibration

Modeling the dynamics of high speed aircraft, micromachined resonators, structures prone to high ground acceleration/ground velocity (a/v) seismic events, etc. requires accurate computation of higher modes of vibration. High speed aircraft (supersonic/hypersonic) undergo significant structural deformations due to extreme aerothermodynamic loads.[7] Moreover, the shock dynamics are sensitive to deformations at the forebody tip of the aircraft. In order to study the dynamics of such aircraft, it is essential to consider higher modes of vibration to accurately determine the deformations. Micromachined resonators have potential applications as high frequency clock oscillators and resonant sensors in the biomedical industry.[56] Resonators made of high Q (quality factor) materials have reduced damping when excited at higher modes,[43] and are thus other applications that require accurate computation of higher modes of vibration. Tall, flexible chimneys experiencing high a/v ratio seismic events have higher modes of vibration that play a significant role in the structural response compared to the fundamental mode of vibration.[21] The term "higher modes of vibration" for the example of micromachined resonators could signify a mode number as high as 28, while in the case of the chimney could imply a mode number as low as the 5th mode of vibration. Although there is a significant difference in what constitutes a higher mode across various applications, the higher modes that are typically difficult to compute play a major role in certain engineering applications. Hence, there is a need for a relatively inexpensive yet accurate method to compute higher modes of vibration.

Continuous structures (structures with continuous distribution of inertial elements and material properties) have infinitely many degrees of freedom, which would require a set of infinite independent generalized coordinates (IGCs) to describe their position at every instant of time. The equations of motion for the vibration of such structures would be in the form of partial differential equations (PDEs) in the independent spatial variables (x, y, z) and time (t). If damping is ignored, vibrations of such structures as described in Ref. [13] can be represented as modal motions where all the mass elements vibrate at specific frequencies (natural frequencies), while maintaining mode shapes that are unique to each of those frequencies. The structural response of the vibrating structure can then be obtained as a

superposition of the constituent modes. Usually, the modes at very high natural frequencies do not contribute significantly to the structure's response.[13] Hence, the infinite dimensional system is considered to be sufficiently well approximated by a finite dimensional system. It is important to note that in the applications discussed above, the higher modes need to be included in the finite dimensional model of the structure. Free vibration analysis of structures involving the computation of higher modes using conventional methods such as the Ritz and finite element methods either produce inaccurate results or require high computational effort.[37] Hence, there is a need for methods that are both (relatively) inexpensive and accurate.

Computing the free vibration mode shapes for a distributed structure requires a variational formulation of Hamilton's principle,[4] where the action function governing the motion of the structure can be minimized by the solution of a differential eigenvalue problem. More often than not, obtaining a closed form solution for this differential eigenvalue problem is not feasible either due to the nature of the governing equations or due to the nonhomogeneous material and/or geometric properties. The Ritz method approximates the solution of this differential eigenvalue problem using a finite linear combination of trial functions, resulting in an algebraic eigenvalue problem.[37] A detailed derivation of the algebraic eigenvalue problem for the case of a free-free homogeneous Euler-Bernoulli beam can be found in Ref. [53]. The infinitely many trial functions defined in terms of the independent spatial variable(s) of the free vibration problem must be linearly independent and form a complete infinite set.

Trial functions can be eigenfunctions, comparison functions, or admissible functions. A typical differential eigenvalue problem governing the free vibration of a structure comprises a set of governing equations of order $2p$ and boundary conditions characterized as geometric boundary conditions of order $p-1$ and/or natural boundary conditions of order $2p-1$, where p is a natural number.[35,45] The eigenfunctions must satisfy the governing equations as well as all the boundary conditions exactly. This requires solving the governing equations analytically, which may not be feasible for most practical problems. On the other hand, the comparison functions are required to satisfy all the boundary conditions exactly and must be at least $2p$ times differentiable. Although the set of comparison functions is significantly larger than that of the eigenfunctions, in some practical problems it may be difficult to find suitable comparison functions, as in the case of the air-breathing hypersonic vehicle discussed earlier. In general, owing to the restrictive nature of the eigenfunctions and comparison functions one would have to rely on admissible functions, which must be at least p times differentiable and must satisfy only the geometric boundary conditions.[37] Free-free structures have only natural boundary conditions, as is the case with the two examples presented in this article. Since admissible functions do not have to satisfy the natural boundary conditions, they are only required to be at least p times differentiable, linearly independent, and form a complete set. Finding a set of such admissible functions may be easy but the rate of convergence to the solution now depends heavily on the choice of admissible functions.

Quasicomparison functions, defined as finite linear combinations of the admissible functions that satisfy the natural boundary conditions, were suggested to improve the convergence rate of the Ritz method using admissible trial functions. The Ritz method has shown

faster convergence using quasicomparison functions[24,36,38,39,41] over conventional admissible functions and sometimes superior performance over the finite element method.[23] Typical admissible functions used in the Ritz method are polynomial,[3] trigonometric, and hyperbolic functions. Higher order polynomial trial functions yield ill-conditioned mass and stiffness matrices,[40,49] while using a combination of trigonometric and hyperbolic functions was shown to introduce numerical instability during computation of higher modes.[5,15,25] Moreover, using trigonometric trial functions alone may introduce additional geometric constraints on the structure.[40] Alternatively, using a linear combination of trigonometric functions and low order polynomial functions was suggested as a suitable choice[12,14,30,31,40] and shown to exhibit faster convergence rates along with better accuracy for higher modes compared to those using only trigonometric trial functions.

The present work proposes a scheme that uses the Ritz method to obtain estimates for natural frequencies, and a linear two-point boundary value problem (two-point BVP) solver, employing superposition and reorthonormalization, to solve the governing equations and boundary conditions iteratively until the estimates for natural frequencies converge. The governing equations for the mode shapes of one-dimensional problems are linear ordinary differential equations (ODEs) in the only spatial variable. These linear ODEs along with the boundary conditions form a linear two-point boundary value problem in terms of the eigenvalue parameter ω (natural frequency). The linear two-point BVP solver is the FORTRAN 77 code SUPORE designed to solve such problems, given an estimate (initial guess) for the eigenvalue parameter ω. SUPORE solves the two-point BVP iteratively using the modified quasi-Newton method to solve for the eigenvalue parameter. The solution for the two-point BVP is obtained by solving a set of initial value problems (for the homogeneous and particular solution vectors) and a system of linear algebraic equations (for the undetermined coefficients of the homogeneous solution vectors), where the solution vector is written as a superposition, with undetermined coefficients, of linearly independent, homogeneous solutions and a particular solution.[46] The homogeneous and particular solutions are reorthonormalized at regular intervals to ensure that the solution vectors do not lose their numerical linear independence.

The proposed scheme is relevant for applications modeled as thin flexible structures that are isotropic, linear, and elastic. The dynamics of such structures must be represented using governing equations in one independent variable resulting in first order ordinary differential equations. It is also assumed that the higher modes are required to be computed due to their significance in forced vibration analysis as in the case of tall chimneys experiencing high a/v ratio seismic events and/or as a consequence of high fidelity modeling as in the case of air-breathing hypersonic vehicles. Moreover, material damping is assumed to be negligible compared to damping due to external forces that are dissipative in nature and are introduced during forced vibration analysis. Since the analysis presented here is restricted to the free vibration case, damping does not play any role in the dynamics. Reference 53 introduces the proposed scheme, where detailed derivations for the eigenvalue problem and governing equations are presented. This scheme is implemented for two case studies, discussed in the following sections, but the analysis in Ref. [53] was restricted to only one choice of trial func-

tions for the Ritz method. As discussed earlier, the rate of convergence of natural frequencies for the Ritz method is sensitive to the choice of trial functions. Some trial functions result in faster convergence than others, thus providing better estimates. Having better estimates for natural frequencies is beneficial in two ways: first, since the estimates are used as initial guesses by SUPORE, having a guess closer to the solution expedites the iterative process, and second, since for higher modes the difference between estimated and converged frequencies can be too large for the iterative process to work, reducing this gap can increase the number of modes computed accurately using SUPORE. In order to emphasize the need for better estimates, a comparative study on the rates of convergence of natural frequencies and mode shapes for various admissible functions deemed efficient in the literature is presented in the following section. Note that, also Ref. [53] introduces percent integral error between modes as a measure for modal comparison, while the present work uses the modal assurance criterion matrix, which does not require normalizing the modes before comparison.

Chapter 4

Description of the Scheme

The proposed scheme uses the Ritz method to compute estimates for the natural frequencies and these estimates are used as initial guesses by SUPORE (linear two-point BVP solver) to obtain accurate "enough" natural frequencies and mode shapes, as required by the problem. This section presents a description of the two methods used in this scheme, namely, the Ritz method and linear two-point BVP solution using SUPORE.

4.1 Ritz Method

The Ritz method involves a variational formulation of Hamilton's principle,[4] where the action function governing the vibrational motion of a structure can be minimized by the solution of an eigenvalue problem. Consider the Lagrangian $\mathcal{L}$ of the vibrating structure, which is defined as the difference between the kinetic energy T due to deformation and the elastic strain energy V stored in the system. The action function is defined as

$$S = \int_{t_i}^{t_f} (T - V)\, dt \tag{4.1}$$

from initial time t_i to final time t_f. According to Hamilton's principle, the vibrating structure would follow a path that would have a stationary value for the action function. This path would satisfy the condition

$$\delta S = \int_{t_i}^{t_f} (\delta T - \delta V)\, dt = 0 \tag{4.2}$$

as long as there are no nonholonomic constraints enforced on the structure.[22] For the case of a transversely vibrating free-free Euler-Bernoulli beam, the kinetic and elastic strain energies

are given by

$$T = \frac{1}{2}\int_0^L m(x)\left(\frac{\partial w}{\partial t}\right)^2 dx \qquad \text{and} \qquad V = \frac{1}{2}\int_0^L EI(x)\left(\frac{\partial^2 w}{\partial x^2}\right)^2 dx. \tag{4.3}$$

Then Eq. (4.2) becomes

$$\int_{t_i}^{t_f}\int_0^L \left(m(x)\dot{w}\delta\dot{w} - EI(x)w''\delta w''\right) dx\, dt = 0. \tag{4.4}$$

Following Ref. [13], we can write the transverse displacement as

$$w(x,\, t) = Y(x)\, P(t) \tag{4.5}$$

where $Y(x)$ is the mode shape function that defines the shape of the structure for a particular mode and $P(t)$ is the modal coordinate function which is a harmonic function in time that describes the change of mode shape with respect to time. Substituting this in Eq. (4.4) and taking variations with respect to $Y(x)$ and $P(t)$ yields

$$\int_{t_i}^{t_f}\left(\left[\int_0^L m(x)Y(x)^2 dx\right]\ddot{P} + \left[\int_0^L EI(x)Y''(x)^2 dx\right]P\right)\delta P\, dt = 0, \tag{4.6}$$

$$\int_{t_i}^{t_f}\left(\omega^2\left[\int_0^L m(x)Y\delta Y\, dx\right] - \left[\int_0^L EI(x)Y''\delta Y'' dx\right]\right)P(t)^2 dt = 0. \tag{4.7}$$

Equation (4.6) implies that $P(t)$ is a harmonic function in time with a natural frequency ω. The Ritz method assumes the mode shape function to be a linear combination of a set of trial functions that satisfy the essential boundary conditions. The finite dimensional assumed mode shape function is given by

$$Y(x) = \{\phi(x)\}^T\{C\}, \tag{4.8}$$

where $\{\phi(x)\}$ is a vector of n trial functions. Substituting the assumed mode shape function in Eq. (4.7) yields

$$\int_{t_i}^{t_f}\delta C^T\left(\omega^2\left[\int_0^L m(x)\{\phi(x)\}\{\phi(x)\}^T dx\right] - \left[\int_0^L EI(x)\{\phi''(x)\}\{\phi''(x)\}^T dx\right]\right)C\, P(t)^2 dt = 0. \tag{4.9}$$

Equation (4.9) gives the condition for a stationary action function, for any arbitrary variation in δC this condition will be satisfied if and only if

$$\left(\omega^2\left[\int_0^L m(x)\{\phi(x)\}\{\phi(x)\}^T dx\right] - \left[\int_0^L EI(x)\{\phi''(x)\}\{\phi''(x)\}^T dx\right]\right)C = 0. \tag{4.10}$$

Equation (4.10) is an eigenvalue problem of the form

$$\left(\omega^2[M] - [K]\right) C = 0, \tag{4.11}$$

which can be solved for the 'n' mode shapes and their corresponding natural frequencies for the free-free Euler-Bernoulli beam. Due to the finite dimensional approximation (4.8), the Ritz method yields inaccurate results at higher modes.[4] Yet, this method provides estimates for the first n natural frequencies, which will be used as initial guesses for solving the governing equations using SUPORE.

4.2 Linear two-point boundary value problem

As described earlier, a vibrating elastic structure would follow the path that would minimize the action function given in Eq. (4.1). This path can be represented as a linear combination of the constituent modes where each mode is the product of a mode shape and a harmonic function (modal coordinate) of frequency ω. The modal coordinates depend on the forcing functions and can be computed, provided the mode shapes are known. The mode shapes can be computed by solving the governing equations subject to boundary conditions, obtained from Eq. (4.7) using integration by parts twice, yielding

$$\omega^2 m(x)Y(x) - EI''(x)Y''(x) - EI'(x)Y^{(3)}(x) - EI(x)Y^{(4)}(x) = 0, \tag{4.12}$$

$$\left[EI(x)Y''(x)\delta Y'(x)\right]_0^L = 0 \quad \text{and} \quad \left[\left(EI'(x)Y''(x) + EI(x)Y^{(3)}(x)\right)\delta Y(x)\right]_0^L = 0. \tag{4.13}$$

Using Eq. (4.12), the governing equations for a free-free Euler-Bernoulli beam can be expressed as a system of first order linear ordinary differential equations

$$\frac{d}{dx}\begin{Bmatrix} y_1(x) \\ y_2(x) \\ y_3(x) \\ y_4(x) \end{Bmatrix} = \begin{pmatrix} 0 & 1 & 0 & 0 \\ 0 & 0 & 1 & 0 \\ 0 & 0 & 0 & 1 \\ \dfrac{\omega^2 m(x)}{EI(x)} & 0 & -\dfrac{EI''(x)}{EI(x)} & -\dfrac{EI'(x)}{EI(x)} \end{pmatrix} \begin{Bmatrix} y_1(x) \\ y_2(x) \\ y_3(x) \\ y_4(x) \end{Bmatrix}. \tag{4.14}$$

Using Eq. (4.13), the boundary conditions can be expressed in the first order or state-space form[28,29]

$$\begin{pmatrix} 0 & 0 & EI(0) & 0 \\ 0 & 0 & EI'(0) & EI(0) \end{pmatrix} \begin{Bmatrix} y_1(0) \\ y_2(0) \\ y_3(0) \\ y_4(0) \end{Bmatrix} = \begin{Bmatrix} 0 \\ 0 \end{Bmatrix}, \tag{4.15}$$

$$\begin{pmatrix} 0 & 0 & EI(L) & 0 \\ 0 & 0 & EI'(L) & EI(L) \end{pmatrix} \begin{Bmatrix} y_1(L) \\ y_2(L) \\ y_3(L) \\ y_4(L) \end{Bmatrix} = \begin{Bmatrix} 0 \\ 0 \end{Bmatrix}. \tag{4.16}$$

The governing equations and boundary conditions for the mode shapes of a free-free Euler-Bernoulli beam can thus be formulated as the linear two-point boundary value problem Eqs. (4.14)-(4.16).

Chapter 5

SUPORE - Two-point BVP solver

Linear two-point boundary value problems of the form

$$y'(x) = F(x)y(x) + g(x), \tag{5.1a}$$
$$A\,y(a) = \alpha, \tag{5.1b}$$
$$B\,y(b) = \beta \tag{5.1c}$$

can be solved using the superposition principle. By applying the superposition principle, the linear two-point boundary value problem can be decomposed into a set of homogeneous equations

$$u'(x) = F(x)u(x), \tag{5.2a}$$
$$A\,u(a) = 0, \tag{5.2b}$$

and particular equations

$$v'(x) = F(x)v(x) + g(x), \tag{5.3a}$$
$$A\,v(a) = \alpha. \tag{5.3b}$$

The homogeneous and particular equations are a set of initial value problems, which can be numerically integrated from $x = a$ to $x = b$. Theoretically, the solution vectors $u_1, \ldots, u_k$ of the homogeneous equations and the solution v of the particular equations will be linearly independent, and $y(x) = v(x) + \sum_{i=1}^{k} c_i\,u_i(x)$.

The final condition

$$Bv(b) + BU(b)\,c = \beta \tag{5.4}$$

can then be used to solve for the undetermined coefficients c. A flowchart of the method used to solve the linear two-point boundary value problem using superposition can be found

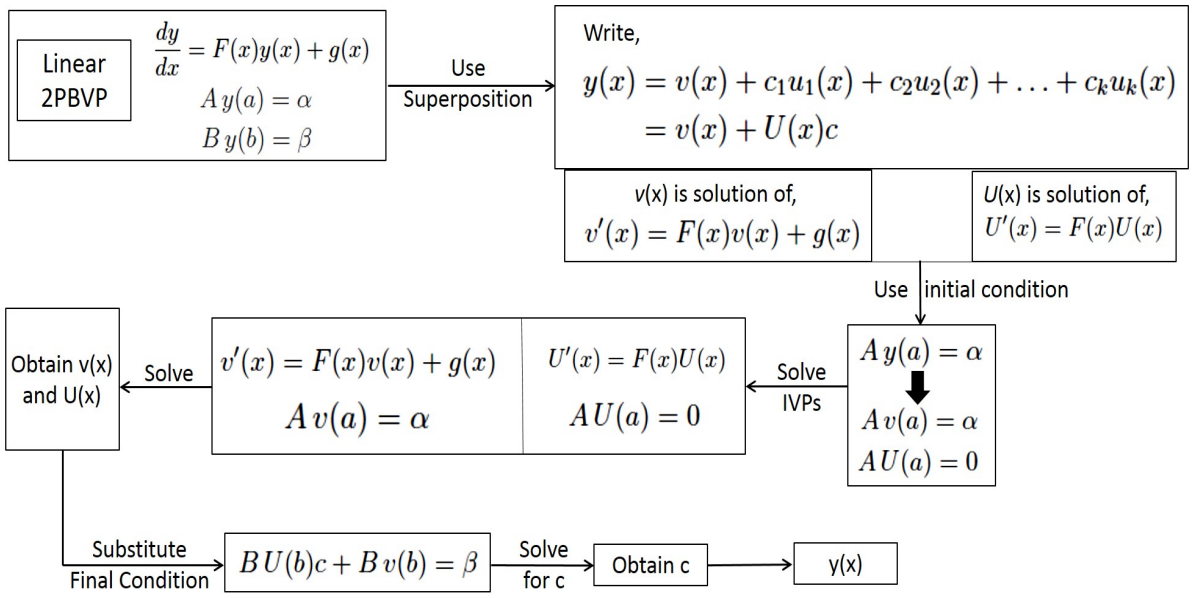

Figure 5.1: Solving linear two-point boundary value problems using superposition.

in Fig. 5.1.

As mentioned earlier, the linear independence of the homogeneous and particular solution vectors is only theoretical. Due to the floating point round off error, the solution vectors may lose their numerical linear independence during the integration process.[46] In order to overcome this challenge, the FORTRAN 77 code SUPORT (SUPerposition coupled with ORThonormalization), on which SUPORE is based, uses Gram-Schmidt orthonormalization to reorthonormalize the solution vectors when their numerical linear independence is insufficient.[46] Orthonormalization here is a means to ensure linear independence of the solution vectors. An example plot is presented for one of the homogeneous solutions u_i in Fig. 5.2 to depict points of reorthonormalization. Numerical integration of the homogeneous and particular equations is carried out starting with the initial conditions at a. At regular intervals, the solution vectors are checked for linear independence. At c the solution vectors have insufficient numerical linear independence and hence are reorthonormalized. Numerical integration now starts from the point c, and continues until the linear independence of the solution vectors is again insufficient at d where they are reorthonormalized again. The integrator reaches the final point b, where the final condition is used to obtain the coefficients for Segment 3. The solution for Segment 3 at d is used as the final condition for Segment 2, which is then used to obtain the coefficients for Segment 2. Similarly, the coefficients for Segment 1 can be computed by using the solution at c, obtained from Segment 2. Now, the solutions from the three segments are pieced together to construct the final solution. Thus, SUPORT uses reorthonormalization to ensure accuracy of the solution over the entire interval $[a, b]$ for a two-point boundary value problem.

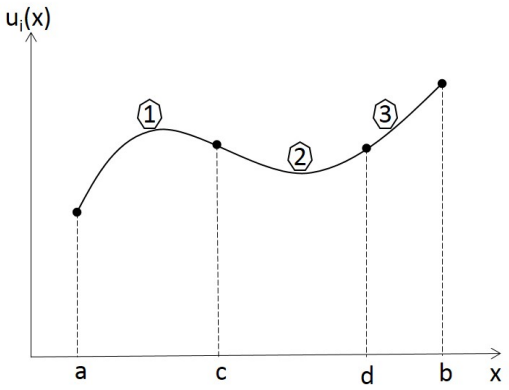

Figure 5.2: Example plot for $u_i(x)$ indicating points of reorthonormalization (c and d)

SUPORT applies to typical linear two-point boundary value problems, but not eigenvalue problems. SUPORE is a modification of SUPORT to iteratively solve the linear two-point BVP until the eigenvalue parameter converges to within the prescribed error tolerance. SUPORE uses the modified quasi-Newton method to compute a zero of the determinant of the product of the coefficient matrix for the final condition and the matrix formed by the homogeneous solution vectors ($\det(B\,U)$). After every iteration, a new estimate for the natural frequency ω is obtained and the updated two-point BVP is solved for the matrix of the homogeneous solution vectors U until the convergence criterion is met.

SUPORE can be used to obtain accurate solutions (within the prescribed error tolerance) for the i^{th} natural frequency ω_i and the corresponding mode shape function $Y_i(x)$. The accuracy of the solutions does not depend on the frequency magnitude of the modes (higher or lower). In other words, SUPORE can obtain accurate solutions for higher modes and lower modes alike, a major advantage of using SUPORE to compute mode shapes for a structure. However, SUPORE can only solve ordinary differential equations, which restricts the structural problem to be one-dimensional. So, there is a trade-off between higher dimensional modeling with fewer modes versus one-dimensional modeling with higher modes.

Chapter 6

Case Study 1: Free-Free Euler Bernoulli Beam

The objective of this case study is to compute the mode shapes up to the 22nd mode for a free-free Euler-Bernoulli beam. The Ritz method is used to compute estimates for the normalized natural frequencies for the first 22 modes, by choosing $n = 22$. The estimates obtained for the normalized natural frequencies of the first 22 modes were used as initial guesses by SUPORE to solve the two-point BVP expressed as a system of first order ordinary differential equations and linear boundary conditions forming a linear two-point BVP

$$\frac{d}{dx}\begin{Bmatrix} y_1(x) \\ y_2(x) \\ y_3(x) \\ y_4(x) \end{Bmatrix} = \begin{pmatrix} 0 & 1 & 0 & 0 \\ 0 & 0 & 1 & 0 \\ 0 & 0 & 0 & 1 \\ \omega_n^2 & 0 & 0 & 0 \end{pmatrix} \begin{Bmatrix} y_1(x) \\ y_2(x) \\ y_3(x) \\ y_4(x) \end{Bmatrix}, \tag{6.1}$$

$$\begin{pmatrix} 0 & 0 & 1 & 0 \\ 0 & 0 & 0 & 1 \end{pmatrix} \begin{Bmatrix} y_1(0) \\ y_2(0) \\ y_3(0) \\ y_4(0) \end{Bmatrix} = \begin{Bmatrix} 0 \\ 0 \end{Bmatrix}, \tag{6.2}$$

$$\begin{pmatrix} 0 & 0 & 1 & 0 \\ 0 & 0 & 0 & 1 \end{pmatrix} \begin{Bmatrix} y_1(1) \\ y_2(1) \\ y_3(1) \\ y_4(1) \end{Bmatrix} = \begin{Bmatrix} 0 \\ 0 \end{Bmatrix}. \tag{6.3}$$

Equations 6.1 – 6.3 form a linear two-point boundary value problem consisting of four first order ordinary differential equations and four boundary conditions, parametrized by the normalized natural frequency ω_n.

The proposed scheme involves three steps, as shown in Fig. 6.1: formulating the free vibration problem as an algebraic eigenvalue problem and estimating the natural frequencies

for the structure, deriving the governing equations and boundary conditions to formulate the linear two-point BVP, and finally solving this two-point BVP using SUPORE and the estimated natural frequencies as initial guesses. SUPORE is equipped to solve such two-point BVPs with eigenvalue parameters by substituting an initial guess for the eigenvalue parameter and solving the resulting two-point BVP by expressing the solution vector as a superposition of homogeneous solution vectors (U, a matrix with homogeneous solution vectors as columns) and a particular solution vector (v) using a vector of undetermined coefficients (c). By employing the superposition principle we transform the linear two-point BVP into a series of IVPs (initial value problems) for U and v, and a system of linear equations for c. Further, the homogeneous and particular solution vectors are reorthonormalized at regular intervals in order to ensure numerical linear independence, which improves the accuracy of the resulting solution. A quasi-Newton approach is employed to improve the estimate for the eigenvalue parameter by solving the two-point BVP iteratively until $det(BU)$ equals zero, where B is the coefficient matrix for the final condition.

The error tolerances for the numerical integrator (Adams or Runge-Kutta-Fehlberg) and the modified quasi-Newton method were set to 10^{-6} in SUPORE. The error tolerance needs to be chosen such that the user considers an error of that order to be acceptable. Figure 6.2 compares the mode shapes obtained from the Ritz method (dashed line) using 22 trial functions and the ones obtained from SUPORE using the proposed scheme. The converged normalized natural frequencies from SUPORE are provided along with each of the subplots in Fig. 6.2. The shaded regions visible for modes 19–22 illustrate the inability of the Ritz method to accurately compute higher modes. The primary objective here is to compute the mode shape for the 22nd mode accurately "enough". It is important to note that this task has been already achieved by SUPORE.

6.1 Percent Integral Error

The integral error for a given mode is defined by

$$\% \text{ Integral error in mode shape} = \frac{\int_0^1 \left|\phi_{Ritz}(x) - \phi_{SUPORE}(x)\right| dx}{\int_0^1 \left|\phi_{SUPORE}(x)\right| dx} \times 100, \tag{6.4}$$

how many Ritz trial functions would be required to obtain a solution with an acceptable integral error of 0.2%? To ensure an integral error less than 0.2% for the 22nd mode, the Ritz method requires at least 52 trial functions. The comparison between the Ritz solution using 52 trial functions and that using 22 trial functions is presented in Fig. 6.3. The shaded region depicts the difference between the solutions obtained using SUPORE and the Ritz method. As the number of trial functions increases from 22 to 52, the Ritz solution

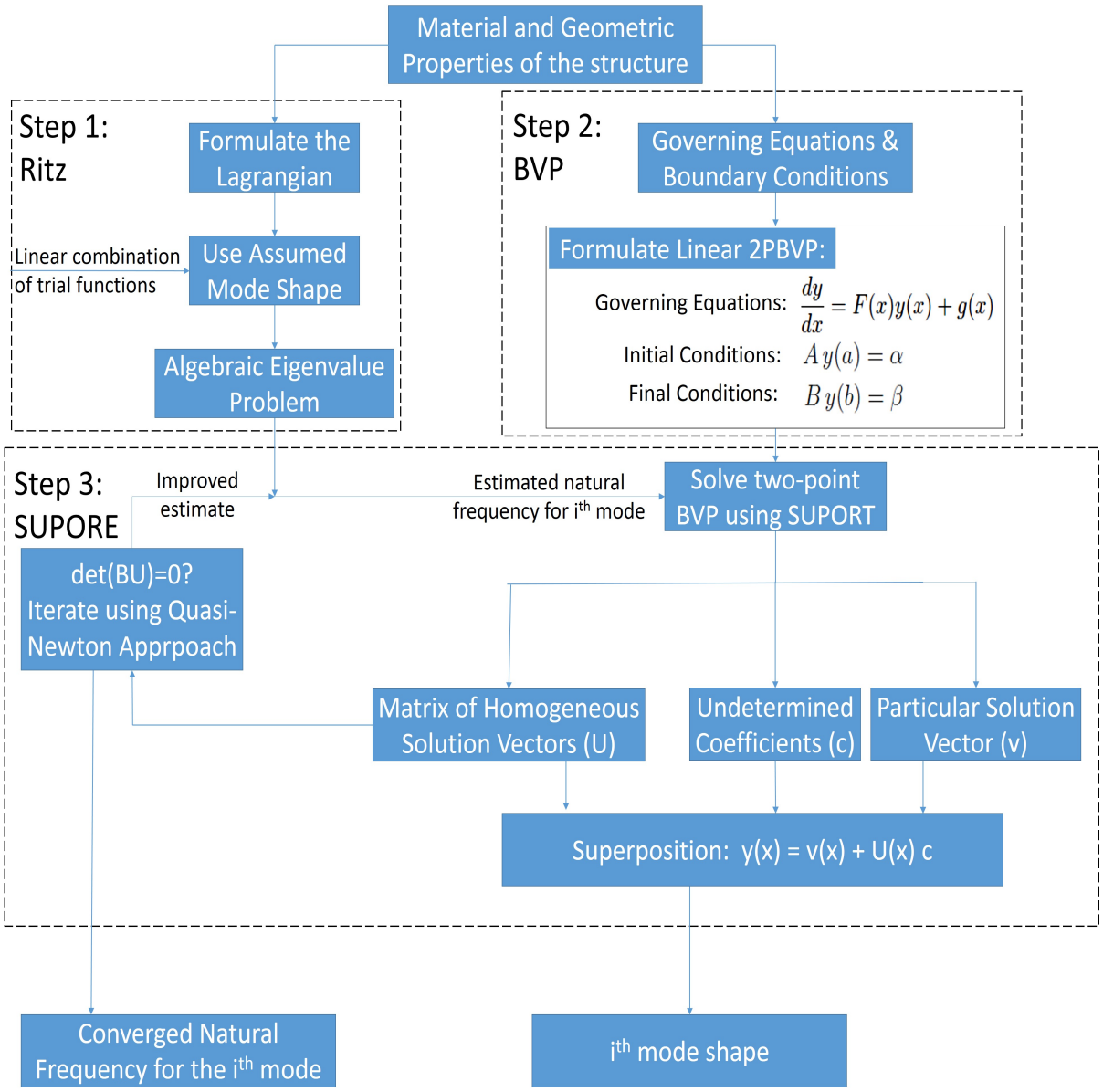

Figure 6.1: A block diagram for the proposed scheme.

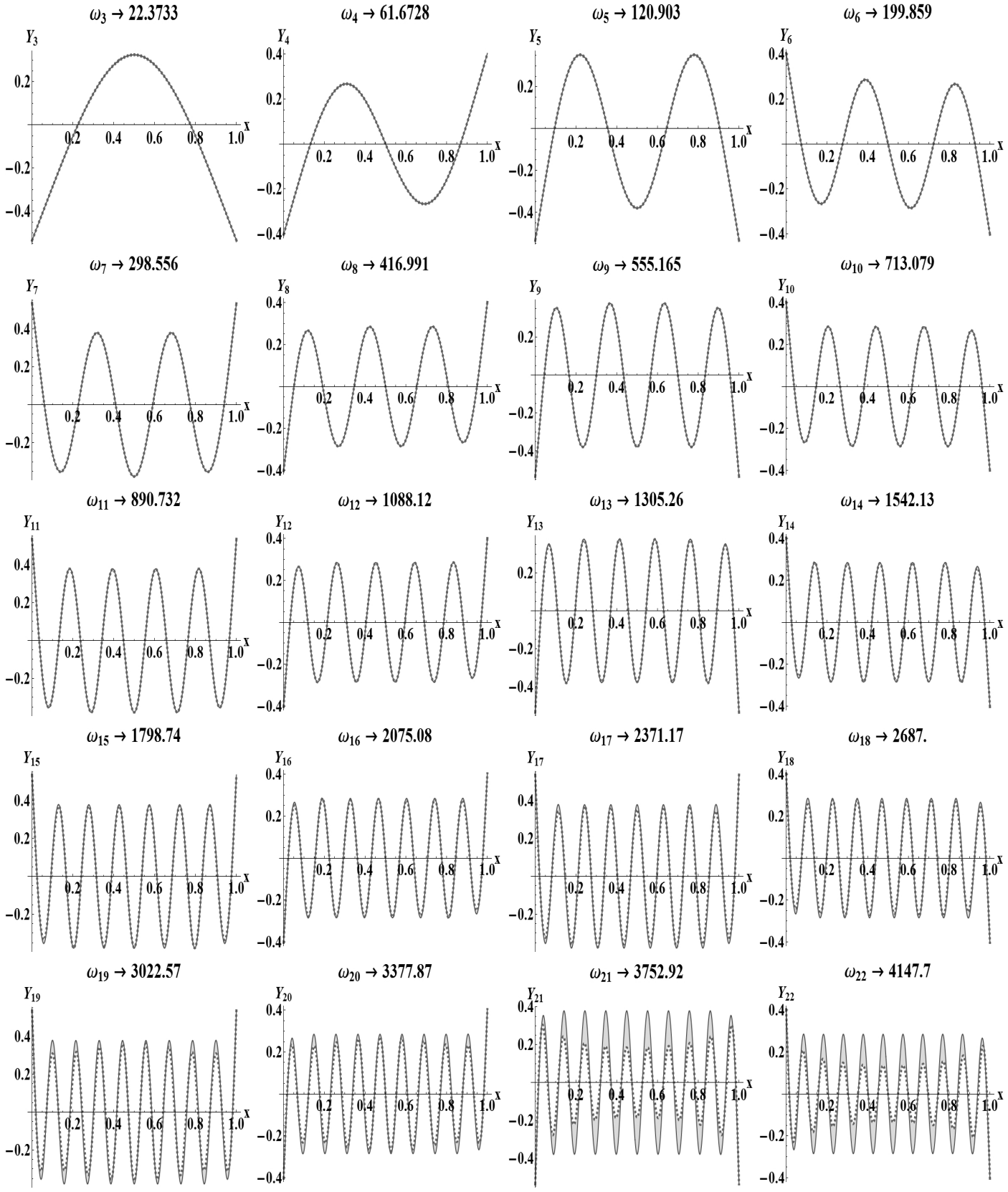

Figure 6.2: Comparison between the mode shapes from SUPORE and the Ritz method (dashed line) using 22 trial functions, along with the converged natural frequencies.

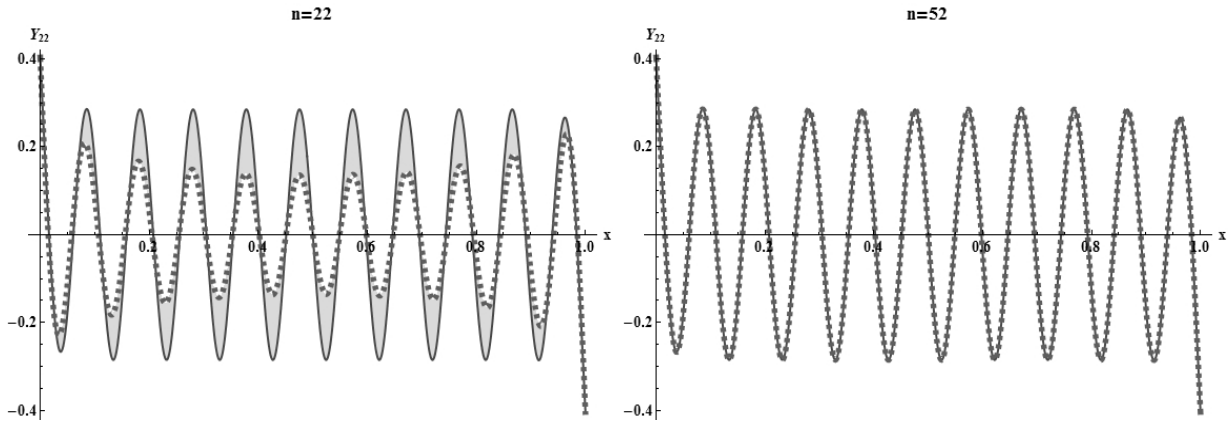

Figure 6.3: Comparison between Ritz solution (dashed line) and solution using SUPORE for the 22nd mode, for the cases with 22 trial functions and 52 trial functions.

gradually approaches the solution obtained from SUPORE. Hence, the solution obtained using SUPORE is more accurate and less expensive in comparison with using Ritz method alone.

Plots for the error in natural frequencies and the integral error in mode shapes (even modes) for the Ritz solution using 52 trial functions in comparison with the one using 22 trial functions are presented in Fig. 6.4.

A study was conducted to find the trend for the least number of Ritz trial functions required to ensure a given accuracy (integral error less than 0.2%) for the highest mode, against the highest mode needed by the finite dimensional model. Figure 6.5 shows that the number of trial functions required by the Ritz method increases almost linearly with the highest mode needed, compared to the proposed scheme where the number of trial functions required is equal to the highest mode needed, as this would suffice for SUPORE. Figure 6.6 compares total CPU time on a log scale for the Ritz method and the proposed scheme. The CPU time for the Ritz method constitutes the time required to solve the eigenvalue problem and compute the integral error, while the CPU time for the proposed scheme includes the time required to compute the Ritz estimates and solve the linear two-point BVP for all the modes up to the highest mode. The shaded regions in Figs. 6.5 and 6.6 show that the Ritz method becomes increasingly expensive with respect to the highest mode required by the finite dimensional model.

6.2 Modal Assurance Criterion

The modal assurance criterion (MAC) is a widely used technique to guage the validity of estimated mode shapes.[2] The MAC is used for modal comparison by measuring the angle

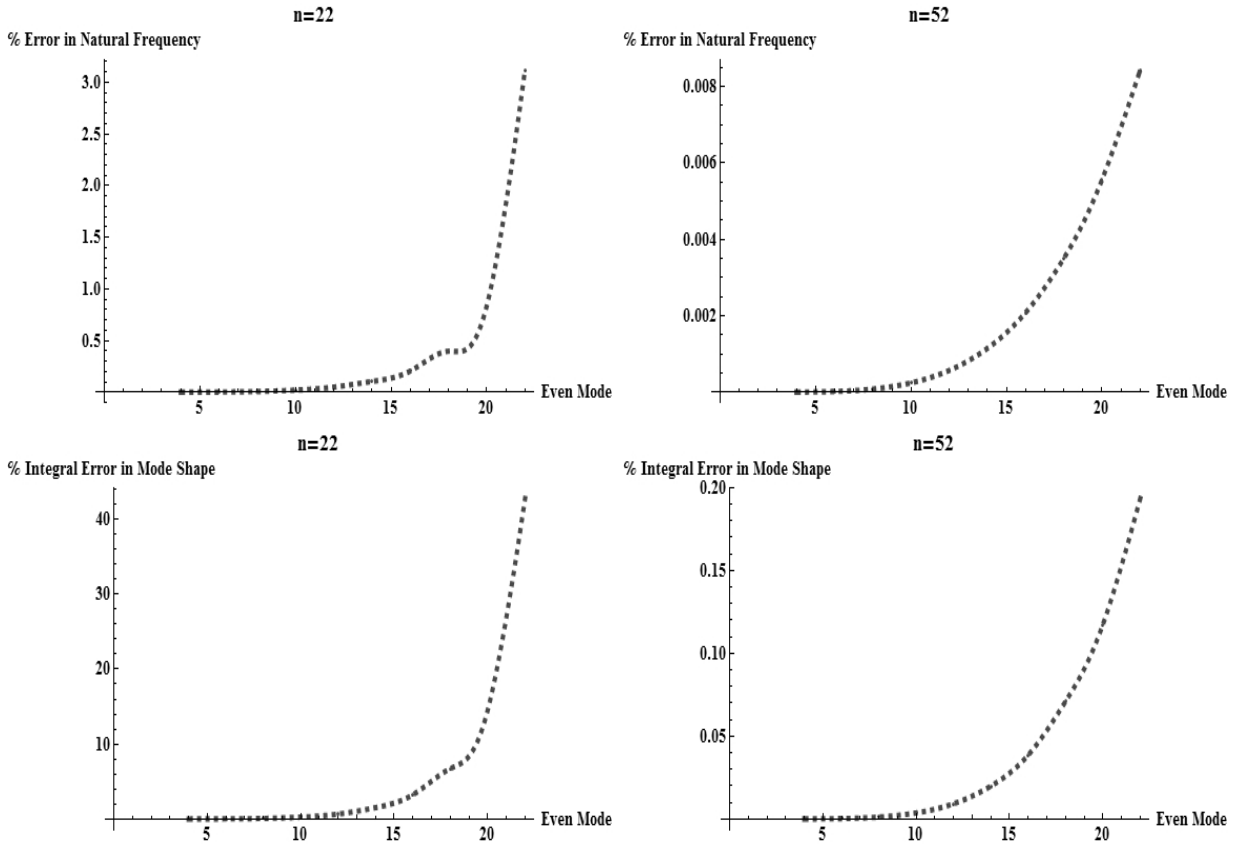

Figure 6.4: Comparison between Ritz solution using 22 trial functions and 52 trial functions, in terms of the error in natural frequencies and integral error in mode shapes.

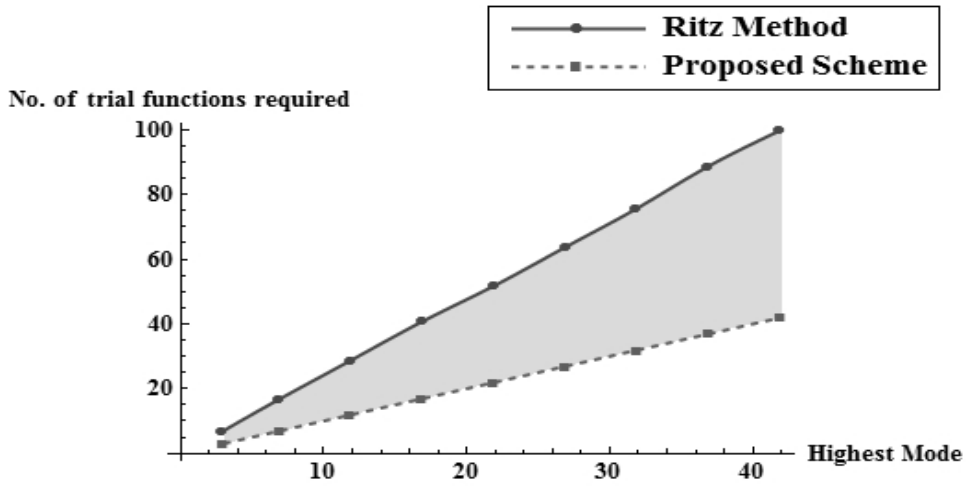

Figure 6.5: Minimum number of trial functions required by Ritz method to obtain solutions accurate up to an integral error of 0.2%, compared with the number of trial functions required by the proposed scheme.

between two vectors, in this context, mode shape vectors computed using the Ritz method and SUPORE. The MAC is a square matrix, whose $(i,\, j)$ element is the square of the cosine of the angle between the i^{th} Ritz mode shape vector $\left\{\phi^{(i)}_{Ritz}\right\}$ and the j^{th} mode shape vector $\left\{\phi^{(j)}_{SUPORE}\right\}$ computed using SUPORE,

$$MAC(i,\, j) = \frac{\left(\left\{\phi^{(i)}_{Ritz}\right\}^T \left\{\phi^{(j)}_{SUPORE}\right\}\right)^2}{\left(\left\{\phi^{(i)}_{Ritz}\right\}^T \left\{\phi^{(i)}_{Ritz}\right\}\right)\left(\left\{\phi^{(j)}_{SUPORE}\right\}^T \left\{\phi^{(j)}_{SUPORE}\right\}\right)}. \tag{6.5}$$

The major advantage in using MAC for modal comparison is that it is not necessary to normalize the solution vectors before comparison. (Note: this measure also has a long history in information retrieval, where it is used to measure the difference between documents.) Ideally, the i^{th} mode shape computed using the Ritz method is the same as the i^{th} mode shape computed using SUPORE and normal to all the other mode shape vectors obtained from SUPORE, resulting in an identity MAC matrix. For all practical purposes, the MAC matrix will not be the identity and the farther it is from an identity matrix the less accurate the solution vectors are. Hence, elementwise absolute values of the difference between the MAC and identity matrices measure dissimilarity between SUPORE and Ritz solutions. Graphical representations of the percent dissimilarities obtained from the MAC matrix for

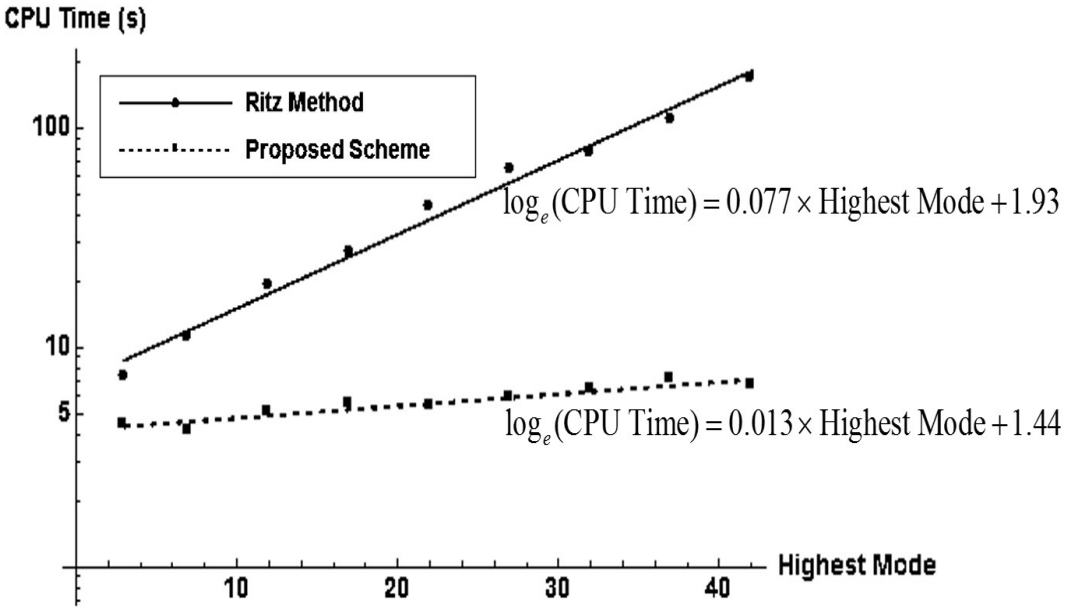

Figure 6.6: Least squares linear fit of CPU time (in seconds on a log scale) for the Ritz method to obtain solutions accurate up to an integral error of 0.2%, compared to the least squares linear fit of CPU time (in seconds on a log scale) for the proposed scheme with respect to the highest mode desired.

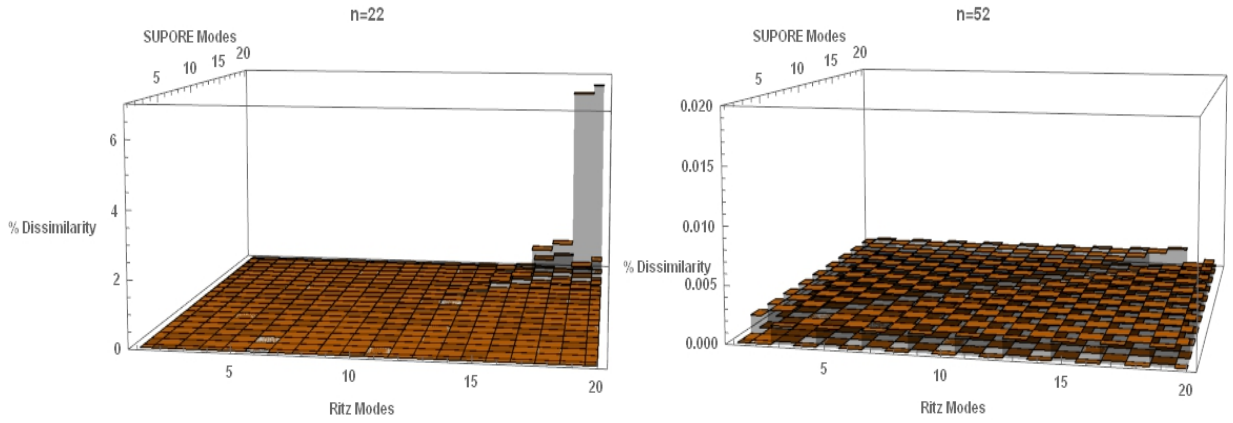

Figure 6.7: A graphical comparison of the percent dissimilarities between the Ritz and SUPORE solution vectors for the first 20 flexible modes, for the cases with 22 trial functions and 52 trial functions.

the first 20 flexible modes of a free-free Euler-Bernoulli beam using 22 and 52 trial functions are presented in Fig. 6.7. The vertical bars represent the percent dissimilarity, while the location of a square on the base grid represents the respective Ritz and SUPORE modes compared. The maximum measure of percent dissimilarity corresponding to the diagonal elements of the MAC matrix for the cases with 22 and 52 trial functions are 6.633% and 1.94×10^{-3}%, respectively. The Ritz solution using 52 trial functions is considered acceptable as the maximum measure of dissimilarity along the diagonal of the MAC matrix is of the order 10^{-5}, which is only an order of magnitude smaller than the absolute and relative error tolerance (1×10^{-6}) used by numerical integrators in SUPORE.

The comparison between the Ritz solution obtained using 52 trial functions and that obtained using 22 trial functions is presented in Fig. 6.8. The shaded region depicts the difference between the solutions obtained using SUPORE and the Ritz method. As the number of trial functions increases from 22 to 52, the Ritz solution gradually approaches the solution obtained from SUPORE. Hence, the solution obtained using SUPORE is more accurate and less expensive in comparison with the sloution obtained using the Ritz method alone. The free vibration mode shapes computed using the Ritz method presented in Fig. 6.2 assume a linear combination of half period sine functions to form the assumed mode shape. It would be interesting to study the effect of various admissible functions on the rate of convergence of the Ritz method. From the myriad of choices available in the literature, four suitable types of admissible functions were chosen for this study: the half period sine functions implemented earlier,[53] the half period cosine functions with a second order polynomial,[40] the half period sine functions with a third order polynomial,[12,14] and an appropriate quasicomparison

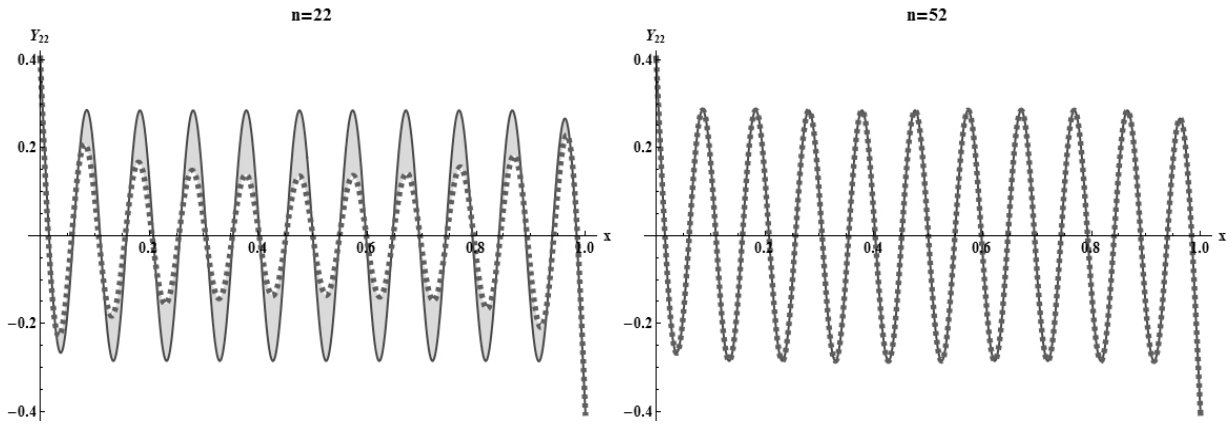

Figure 6.8: Comparison between Ritz solution (dashed line) and solution using SUPORE for the 22nd mode, for the cases with 22 trial functions and 52 trial functions.

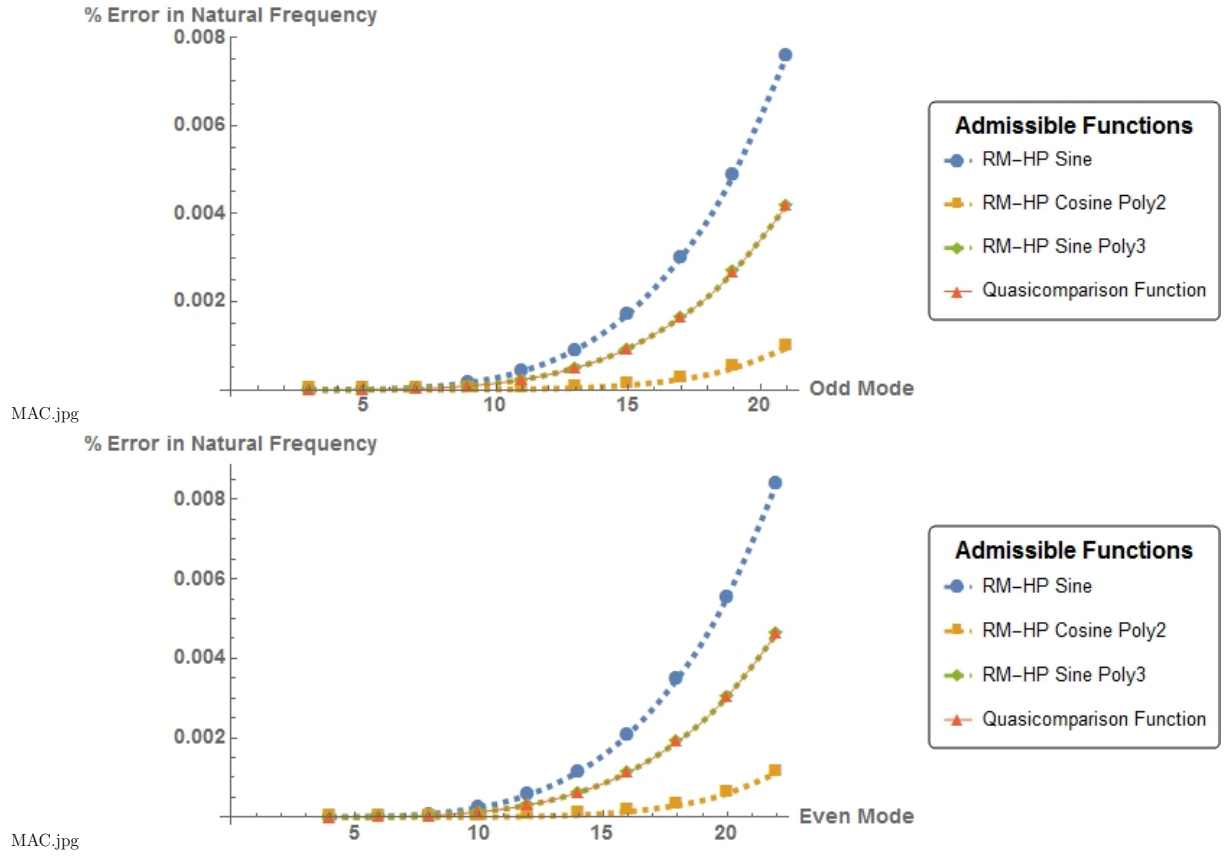

Figure 6.9: Comparative study of the percent error in natural frequencies up to the 22nd mode computed using the Ritz method with 52 trial functions for various admissible functions.

function. The assumed mode shapes for these admissible functions are

$$Y_{\text{HPSin}}(x) = C_1 + C_2 x + \sum_{i=3}^{n} C_i \sin\left((i-2)\pi x\right), \tag{6.6}$$

$$Y_{\text{HPCosPoly2}}(x) = C_1 + C_2 x + C_3 x^2 + \sum_{i=4}^{n} C_i \cos\left((i-3)\pi x\right), \tag{6.7}$$

$$Y_{\text{HPSinPoly3}}(x) = C_1 + C_2 x + C_3 x^2 + C_4 x^3 + \sum_{i=5}^{n} C_i \sin\left((i-4)\pi x\right), \tag{6.8}$$

$$Y_{\text{QCF}}(x) = C_1 + C_2 x + C_4 \cos(\pi x) + C_6 \cos(2\pi x) + \sum_{i=3, i\neq 4, i\neq 6}^{n} C_i \sin\left((i-2)\pi x\right). \tag{6.9}$$

The percent errors in estimating the natural frequencies and percent dissimilarity in mode shapes up to the 22nd mode for the Ritz method with 52 trial functions using the four choices of admissible functions are presented in Figs. 6.9 and 6.10. The half period cosine functions with a second order polynomial show the fastest convergence rate for the natural frequencies and mode shapes, followed by the quasicomparison functions and half period sine functions with a third order polynomial, followed by half period sine functions. It is interesting to note that a linear combination of low order polynomials with trigonometric functions improves the rate of convergence as claimed by Monterrubio and Ilanko.[40]

Finally, a study was conducted to find the trend for the least number of Ritz trial functions required to ensure a given accuracy (measure of dissimilarity of the order 10^{-5}) for the highest mode, against the highest mode needed by the finite dimensional model for various choices of admissible functions. Figure 6.11 shows that the number of trial functions required by the Ritz method increases almost linearly with the highest mode needed for all four choices of admissible functions, compared to the proposed scheme where the number of trial functions required is equal to the highest mode needed, as this would suffice for SUPORE. Figure 6.12 compares total CPU time on a log scale for the Ritz method for the four types of admissible functions and the proposed scheme. The CPU time for the Ritz method consists of the time required to solve the eigenvalue problem and compute the percent dissimilarity, while the CPU time for the proposed scheme consists of the time required to compute the Ritz estimates and solve the linear two-point BVP for all the modes up to the highest mode. Figures 6.11 and 6.12 show that all the four choices of trial functions exhibit comparable computational costs. It is important to note that despite the relative merits and demerits of these four choices of trial functions, they collectively show that the Ritz method, in general, becomes increasingly more expensive than the proposed method with respect to the highest mode required by the finite dimensional model.

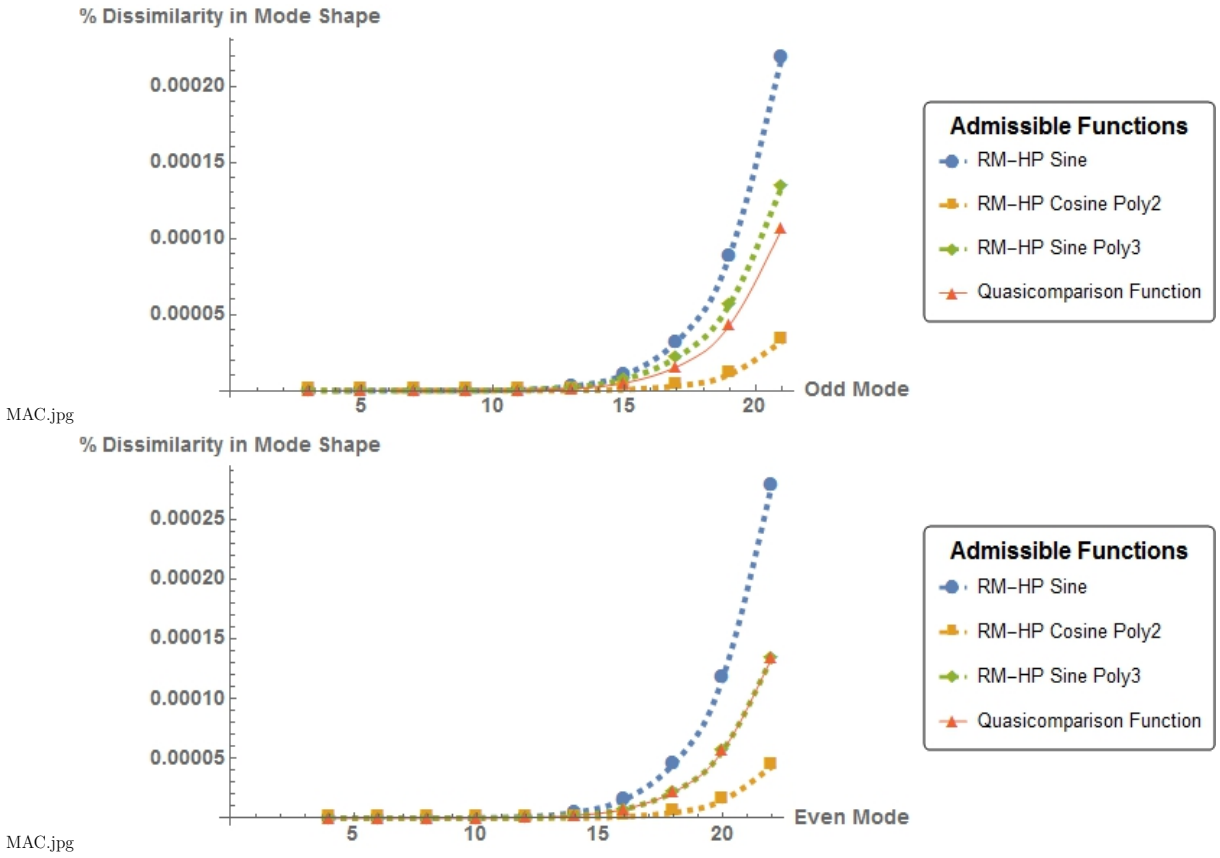

Figure 6.10: Comparative study of the percent dissimilarity in mode shapes up to the 22nd mode computed using the Ritz method with 52 trial functions for various admissible functions.

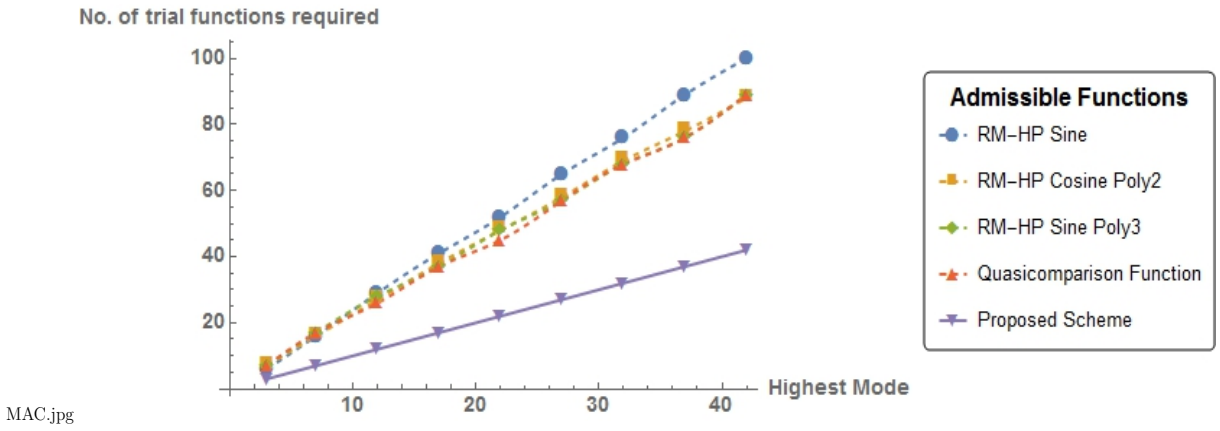

Figure 6.11: Minimum number of trial functions required by Ritz method using various admissible functions to obtain solutions accurate up to a dissimilarity measure of the order 10^{-5}, compared with the number of trial functions required by the proposed scheme.

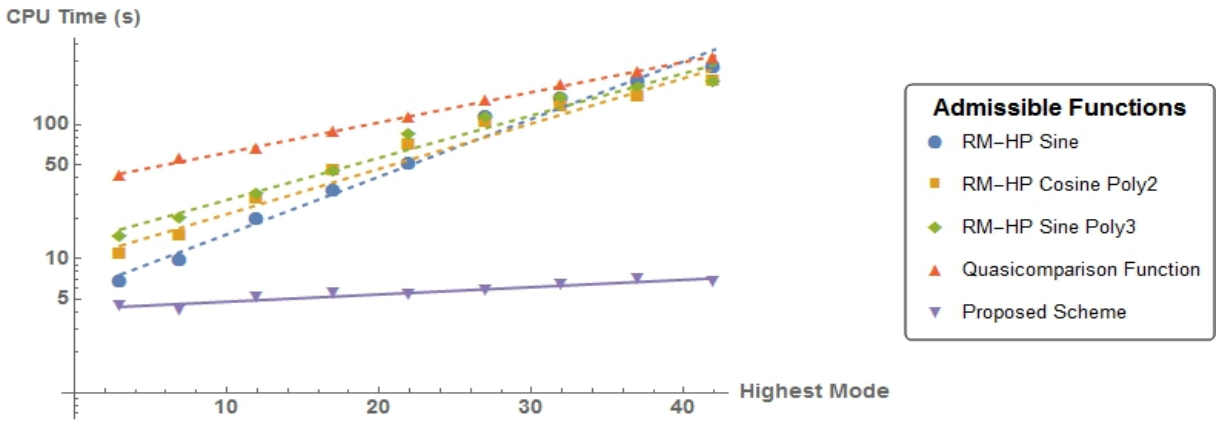

Figure 6.12: Least squares linear fit of CPU time (in seconds on a log scale) for the Ritz method using various admissible functions to obtain solutions accurate up to a dissimilarity measure of the order 10^{-5}, compared to the least squares linear fit of CPU time (in seconds on a log scale) for the proposed scheme with respect to the highest mode desired.

Chapter 7

Case Study 2: Air-breathing Hypersonic Vehicle

A free-free homogeneous Euler-Bernoulli beam is one of the most widely used idealizations in modeling dynamics of flexible structures. However, the increasing need for high fidelity models is driving engineers to improve accuracy by more realistically modeling structures. This case study is one such example where high fidelity modeling is required to compute free vibration mode shapes and natural frequencies. A typical air-breathing hypersonic vehicle experiences extreme aerodynamic and thermal loads that cause significant flexing of the airframe detrimental to the aircraft's performance. Hence, higher order modeling is required to include these flexibility effects and improve the accuracy of the model. The geometry of a typical air-breathing hypersonic vehicle is presented in Fig. 7.1 with a top view, side view, cross-sectional view and all the required dimensions. In order to improve the fidelity of the model, nonstructural masses such as mass of subsystems, fuel tanks, payload, and propulsion system are also included. The distribution of the nonstructural mass and material properties of the airframe are presented in Fig. 7.2.

Owing to the thin-walled nature of the airframe, thin-walled beam theory is used taking into account axial, shear, bending, and torsional vibrations. The airframe is assumed to be made of a linearly elastic and isotropic material. Further, plane sections are assumed to remain planar and the infinitesimal strain assumption is also made. Under these assumptions, the deformations (u_1, u_2, u_3) at a point (x_1, x_2, x_3) are expressed as

$$u_1(x_1, x_2, x_3) = \bar{u}_1(x_1) + x_3\beta_2(x_1) - x_2\beta_3(x_1) + \psi(x_2, x_3)\beta_1'(x_1), \tag{7.1}$$

$$u_2(x_1, x_2, x_3) = \bar{u}_2(x_1) - x_3\beta_1(x_1), \tag{7.2}$$

$$u_3(x_1, x_2, x_3) = \bar{u}_3(x_1) + x_2\beta_1(x_1), \tag{7.3}$$

where $\bar{u}_1$, $\bar{u}_2$, $\bar{u}_3$ are translational displacements and β_1, β_2, β_3 are rotational displacements of the rigid cross-section about x_1, x_2, x_3 axes respectively. The deformations (u_1, u_2, u_3) are used in the strain displacement relations, assuming infinitesimal strains to compute the

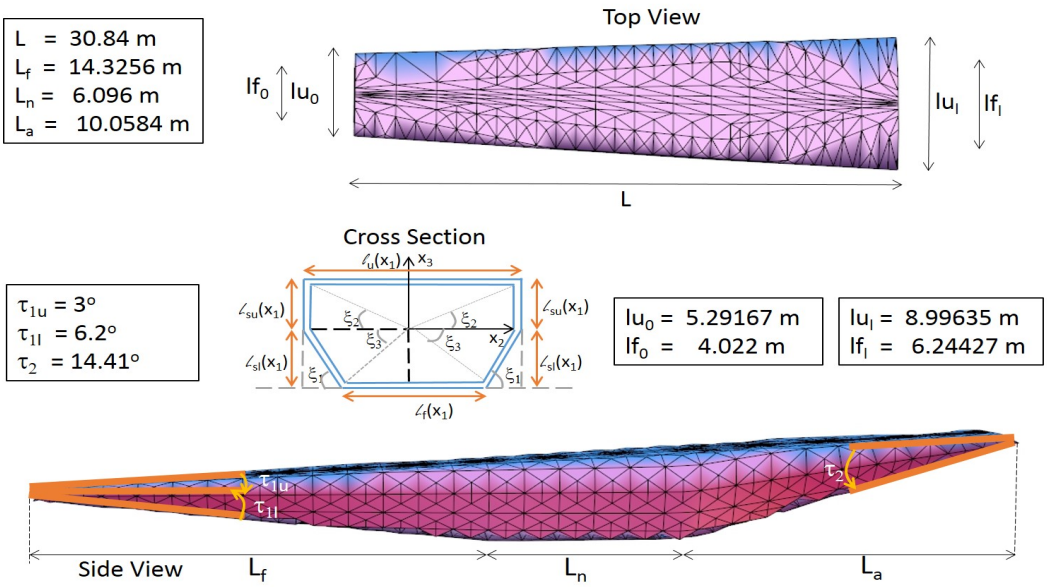

Figure 7.1: Geometry of a typical air-breathing hypersonic vehicle.

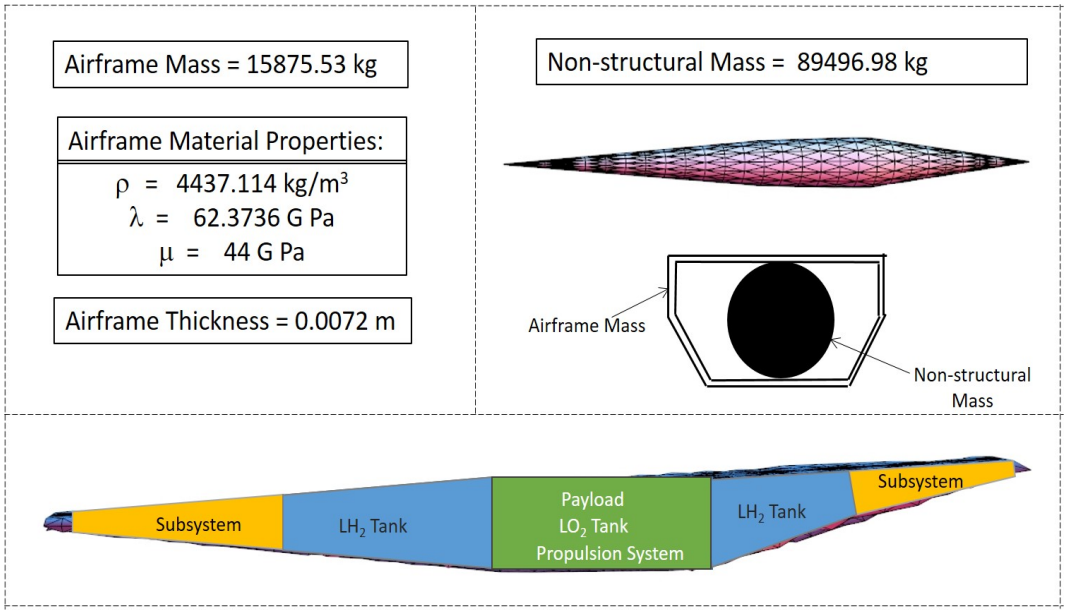

Figure 7.2: Material properties of the airframe and distribution of nonstructural mass.

three out-of-plane strains (ϵ_{11}, γ_{12}, γ_{13}) while the in-plane strains (ϵ_{22}, ϵ_{33}, γ_{23}) are zero due to the rigid plane section assumption. These six strains are substituted in the stress-strain relations to compute the three out-of-plane stresses (σ_{11}, τ_{12}, τ_{13}) and three in-plane stresses (σ_{22}, σ_{33}, τ_{23}), giving

$$\sigma_{11}(x_1, x_2, x_3) = \lambda(x_1)\,(\epsilon_{11} + \epsilon_{22} + \epsilon_{33}) + 2\mu(x_1)\epsilon_{11}, \tag{7.4}$$
$$\sigma_{22}(x_1, x_2, x_3) = \lambda(x_1)\,(\epsilon_{11} + \epsilon_{22} + \epsilon_{33}) + 2\mu(x_1)\epsilon_{22}, \tag{7.5}$$
$$\sigma_{33}(x_1, x_2, x_3) = \lambda(x_1)\,(\epsilon_{11} + \epsilon_{22} + \epsilon_{33}) + 2\mu(x_1)\epsilon_{33}, \tag{7.6}$$
$$\tau_{12}(x_1, x_2, x_3) = \mu(x_1)\,\gamma_{12}, \tag{7.7}$$
$$\tau_{13}(x_1, x_2, x_3) = \mu(x_1)\,\gamma_{13}, \tag{7.8}$$
$$\tau_{23}(x_1, x_2, x_3) = \mu(x_1)\,\gamma_{23}. \tag{7.9}$$

Using the expressions for stresses and strains at a given point (x_1, x_2, x_3), the elastic strain energy (V) of the airframe is given by

$$V = \int_\Omega (\sigma_{11}\epsilon_{11} + \sigma_{22}\epsilon_{22} + \sigma_{33}\epsilon_{33} + \tau_{12}\gamma_{12} + \tau_{13}\gamma_{13} + \tau_{23}\gamma_{23})\, dx_1 dx_2 dx_3, \tag{7.10}$$

where Ω represents the volumne of the aircraft. The kinetic energy (T) of the structure, integrating the kinetic energy of a rigid cross-section along the length of the aircraft, is

$$T = \int_{x_1} \left(m(x_1)\dot{\bar{u}}_1^2 + m(x_1)\dot{\bar{u}}_2^2 + m(x_1)\dot{\bar{u}}_3^2 + J_{11}(x_1)\dot{\beta}_1^2 + J_{22}(x_1)\dot{\beta}_2^2 + J_{33}(x_1)\dot{\beta}_3^2 \right) dx_1 \tag{7.11}$$

where $x_1 \in [0,\, L]$, $m(x_1)$ is the mass of a rigid cross-section at a distance x_1 from the origin and $J_{11}(x_1)$, $J_{22}(x_1)$, $J_{33}(x_1)$ are the principal moments of inertia of a rigid cross-section at a distance x_1 from the origin. The Lagrangian

$$\mathcal{L} = T - V, \tag{7.12}$$

using the expressions for kinetic and potential energies, is used to compute the free vibration mode shapes and natural frequencies by employing the novel scheme described in the previous sections. Figure 7.3 presents the results for the first transverse bending, lateral bending, and torsional modes using the Ritz-SUPORE method with 120 trial functions and a comparison with the Ritz method using 300 trial functions. The half period sine functions are used as admissible functions for this case. The solutions obtained using the Ritz method and SUPORE graphically follow a similar trend, which is sufficient to verify that SUPORE and the Ritz method solved the same problem, but not sufficient to conclude that the error is insignificant.

7.1 Percent Integral Error

Results from a study of the percent error in natural frequency and percent integral error in mode shapes are presented in Fig. 7.4. The asymptotic trend in error growth seen in the case

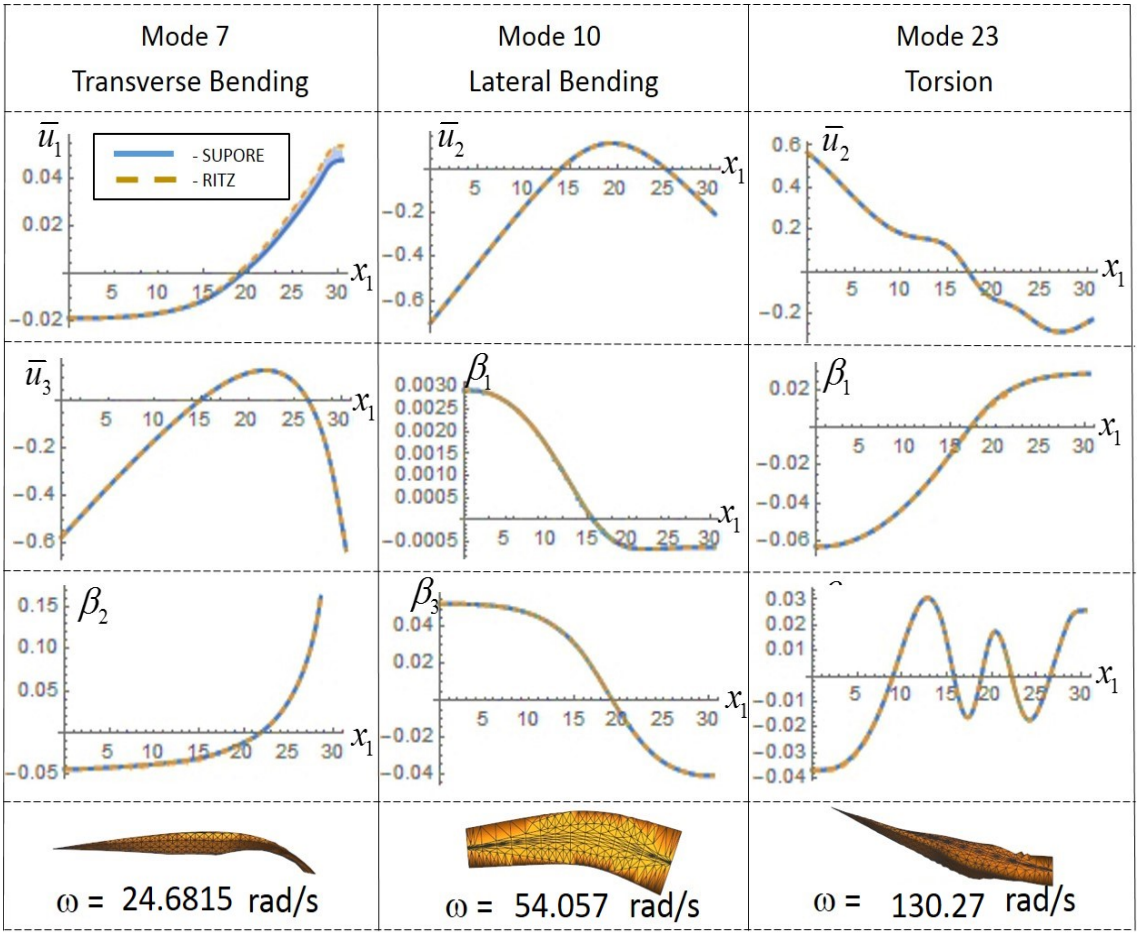

Figure 7.3: Mode shapes and natural frequencies for the first transverse bending, lateral bending, and torsion.

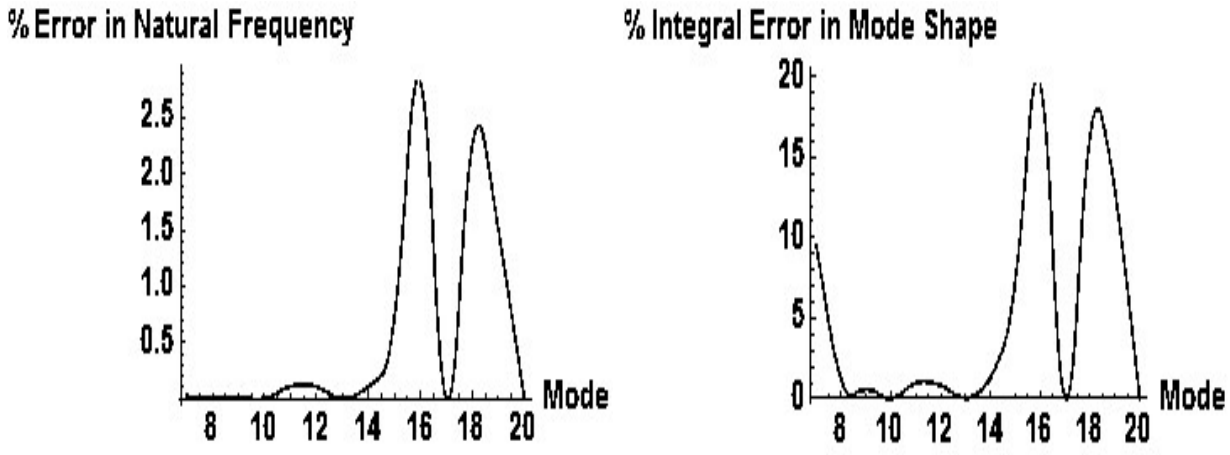

Figure 7.4: Percent error in natural frequencies and percent integral error in mode shapes between Ritz-SUPORE using 120 trial functions and Ritz using 300 trial functions

of the free-free homogeneous beam cannot be observed here. Even though the Ritz method uses up to 300 trial functions, no significant reduction in the error occurs.

7.2 Modal Assurance Criterion

The two suitable choices of admissible functions were the half period sine functions and the half period sine functions with third order polynomial. Figure 7.5 presents results from a study of the percent error in natural frequencies and percent dissimilarity in mode shapes computed using the Ritz method with 300 trial functions for the two suitable admissible function choices. The asymptotic trend in error growth seen in the case of the free-free homogeneous beam cannot be observed here. Even though the Ritz method uses up to 300 trial functions, no significant reduction in the error occurs, although, the half period sine functions with third order polynomial yield better results than the half period sine functions at higher modes. This validates the claims made by Monterrubio and Ilanko[40] regarding improving convergence rates by using a linear combination of low-order polynomial and trigonometric trial functions.

This shows that for such complex structural models using the Ritz method alone may not give "accurate enough" results. Moreover, note that *the accuracy of the Ritz method for the first few modes may be less than that for some higher modes*, as shown in Fig. 7.5. On the other hand, SUPORE ensures that the results for all the modes are within the same prescribed error bounds.

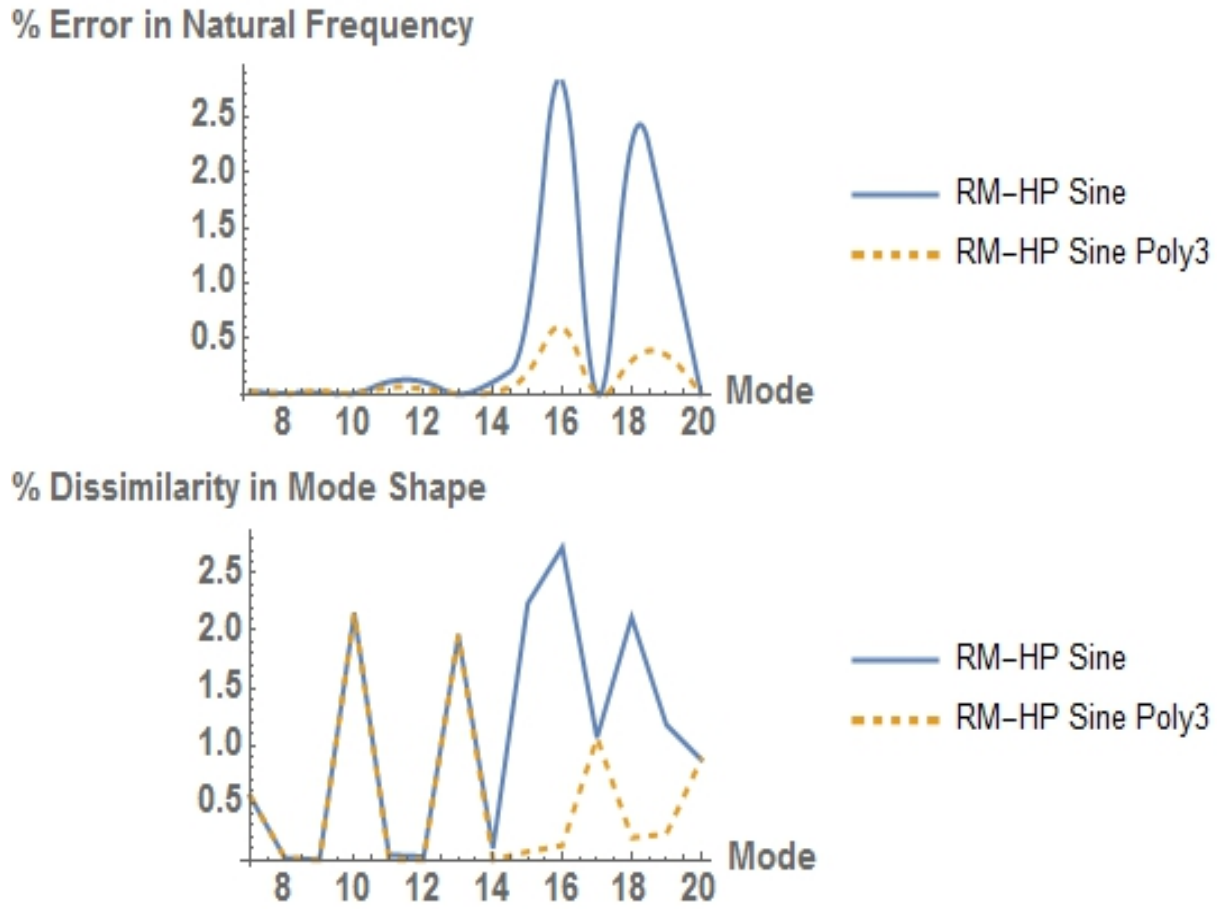

Figure 7.5: Percent error in natural frequencies and percent dissimilarity in mode shapes between Ritz-SUPORE (proposed scheme) using 120 trial functions and Ritz using 300 trial functions, for the cases with half period sine functions and half period sine functions with third order polynomial.

Chapter 8

Free Vibration Analysis

Interaction between aero, thermal, and structural dynamics of an air-breathing hypersonic vehicle has been studied extensively in the literature. Effects of such an interaction are incorporated in vehicle dynamics models[7] using two free-free homogeneous Euler-Bernoulli beams to represent the motion of the fore body and the aft body, respectively. A high-fidelity model is employed to improve the accuracy of the structural response.

According to Hamilton's principle, the vibrating structure would follow a path that would have a stationary value for the action function. Recall that the six independent dispacements describing the motion of a rigid cross section are written as a product of a mode shape and a modal coordinate specific to a given mode. Applying separation of variables and using the variational approach produces twelve governing equations, which are first order linear ordinary differential equations in terms of the independent variable x_1 with an eigenvalue parameter ω and twelve boundary conditions. These equations are solved using SUPORE, an eigenvalue two-point boundary value problem solver that requires initial guesses for the eigenvalues, which were computed using the Ritz method.[53] SUPORE allows the user to choose the relative and absolute error tolerances for the natural frequencies and mode shapes, whereby one may ensure that the solutions have the prescribed level of accuracy. Moreover, SUPORE solves the governing equations for every mode independently ensuring that all modal solutions have the same accuracy. A detailed description of this method was given in Ref. [53] and the results are presented in Figs. 8.1 and 8.2, where the solid line represents a solution from SUPORE and the dashed line represents a solution from the Ritz method. Carefully inspecting the results shows that the mode shapes can be classified into two types, namely axial-transverse vibration modes and torsional-lateral vibration modes. The axial-transverse vibration mode couples $\bar{u}_1$, $\bar{u}_3$, and β_2 , where β_2 alone represents pure transverse bending, $\bar{u}_1$ alone represents axial vibration, and coupling between β_2 and $\bar{u}_3$ represents transverse bending with shear as shown in Fig. 8.1. On the other hand, the torsional-lateral vibration mode couples $\bar{u}_3$, β_1, and β_3 , where β_3 alone represents pure lateral bending, β_1 alone represents torsion, and coupling between β_3 and $\bar{u}_2$ represents lateral bending with shear as shown in Fig. 8.2. The axial-transverse vibration modes are predominant at lower

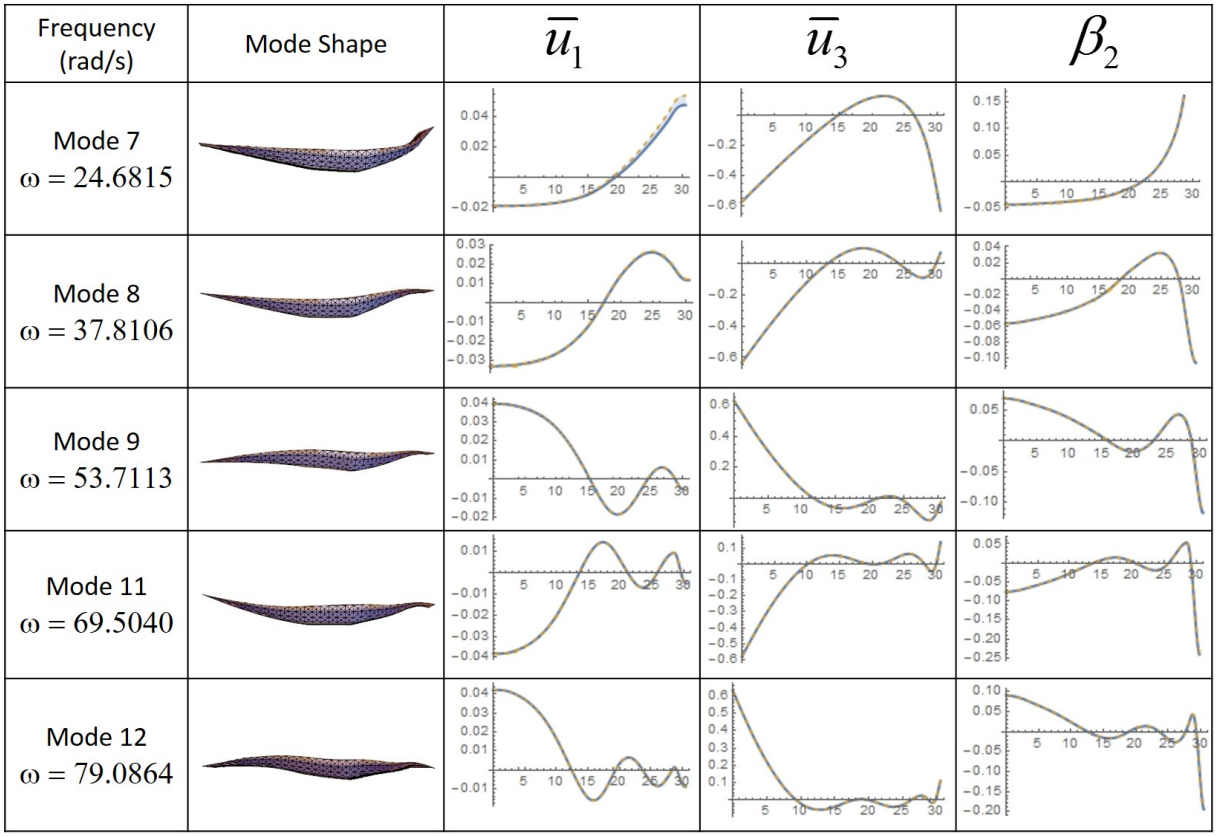

Figure 8.1: Mode shapes and natural frequencies of the first five axial-transverse vibration modes.

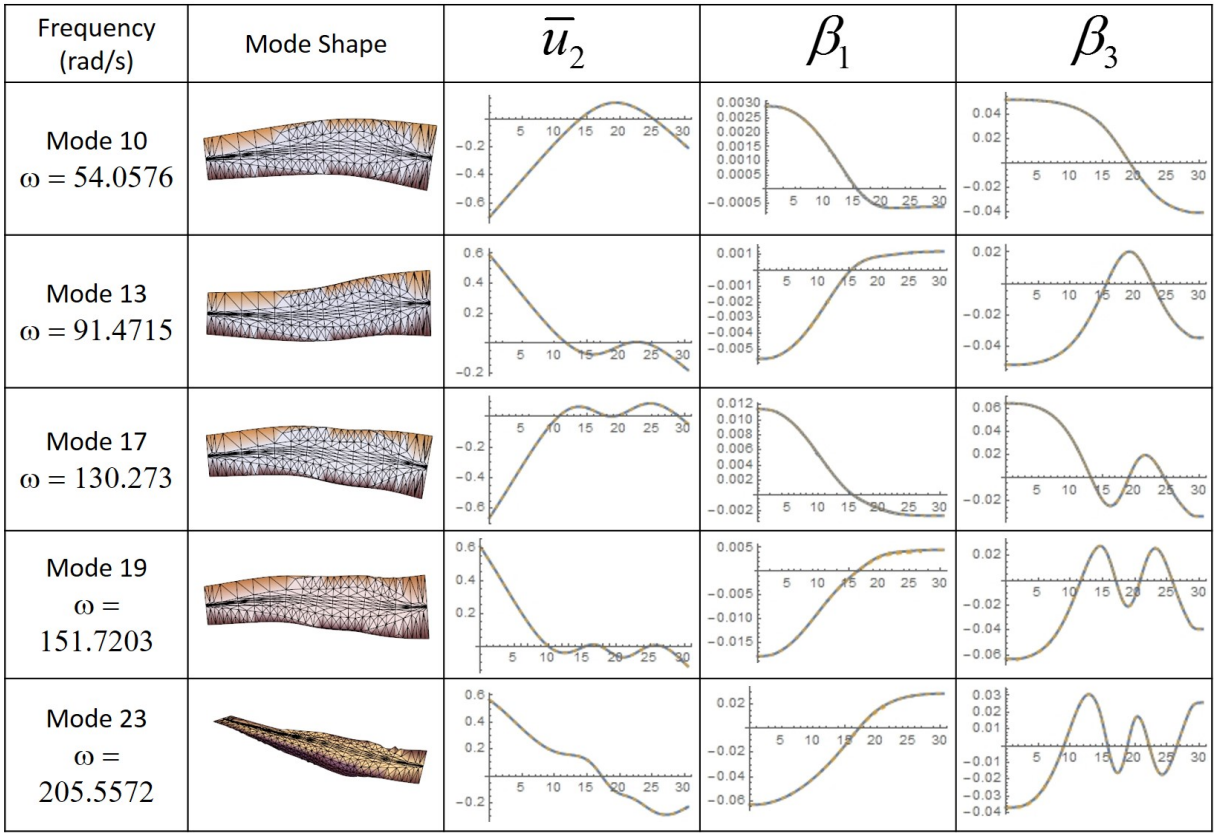

Figure 8.2: Mode shapes and natural frequencies of the first five torsional-lateral vibration modes.

natural frequencies and at higher frequencies the torsional-lateral vibration modes occur more frequently. This gives an insight into the forced structural response of the aircraft depending on the frequency of excitations. At lower excitation frequencies, the motion would be predominantly axial-transvere, while at higher excitation frequencies the motion would be primarily torsional-lateral.

Chapter 9

Forced Vibration : Impulse Response

In order to reiterate the need to include higher modes in air-breathing hypersonic vehicle models, forced virbation analysis is carried out. It is important to note that this analysis is restricted to only studying the impulse response of the structure and is not the in-flight aeroelastic response that requires modeling interactions between the tightly integrated airframe, the propulsion system, and the associated hypersonic flowfield,[6,7,9,10,16,26,33,34,44,52,54,58] which is a growing field of study in itself. However, in order to emphasize the need for higher modes it would suffice to study the impulse response of the structure. The Lagrangian in Eq. (**??**) expressed as an integral of quadratic forms is

$$\begin{aligned}\mathcal{L} = &\int_{x_1} \{\dot{\boldsymbol{\eta}}\}^T_{1\times n} \left[(\Phi)^T_{n\times 6} (\mathcal{M})_{6\times 6} (\Phi)_{6\times n}\right] \{\dot{\boldsymbol{\eta}}\}_{n\times 1}\, dx_1 \\ &- \int_{x_1} \{\boldsymbol{\eta}\}^T_{1\times n} \left[(\Phi')^T_{n\times 6} (\mathcal{K})_{6\times 6} (\Phi')_{6\times n}\right] \{\boldsymbol{\eta}\}_{n\times 1}\, dx_1, \end{aligned} \tag{9.1}$$

where $(\mathcal{M})_{6\times 6}$ and $(\mathcal{K})_{6\times 6}$ are the mass and stiffness coefficient matrices associated with the six independent displacements

$$\left\{\begin{array}{c} \bar{u}_1(x_1,\, t) \\ \bar{u}_2(x_1,\, t) \\ \bar{u}_3(x_1,\, t) \\ \beta_1(x_1,\, t) \\ \beta_2(x_1,\, t) \\ \beta_3(x_1,\, t) \end{array}\right\} = (\Phi(x_1))_{6\times n} \{\boldsymbol{\eta}(t)\}_{n\times 1} \tag{9.2}$$

expressed as a linear combination of the n mode shapes and their corresponding modal coordinates. By substituting the free vibration mode shapes in Eq. (9.1), and integrating the mass and stiffness matrices we can obtain a simplified expression for the Lagrangian

$$\mathcal{L}(\boldsymbol{\eta},\, \dot{\boldsymbol{\eta}}) = \{\dot{\boldsymbol{\eta}}(t)\}^T [M] \{\dot{\boldsymbol{\eta}}(t)\} - \{\boldsymbol{\eta}(t)\}^T [K] \{\boldsymbol{\eta}(t)\}\,. \tag{9.3}$$

Using Hamilton's principle of least action, the equations of motion for the structure are given by

$$[M]\{\ddot{\boldsymbol{\eta}}(t)\} + [K]\{\boldsymbol{\eta}(t)\} = \{\mathbf{Q}(\boldsymbol{\eta}, \dot{\boldsymbol{\eta}}, t)\}, \tag{9.4}$$

where $[M]$ and $[K]$ are mass and stiffness matrices, and $\{\mathbf{Q}\}$ is the generalized force vector with respect to the vehicle fixed frame. In the subsequent forced vibration analysis, two cases are studied: the undamped case and the case with Rayleigh damping. The generalized force vector, for both cases, is an impulse applied at initial time with a magnitude equal to 1×10^{-4} times the weight of the aircraft.

For the undamped case, the stiffness matrix is diagonalized with respect to the mass matrix and the decoupled problem is solved in the Laplace domain. The resulting modal coordinate vector, after carrying out the necessary transformation, can be used in conjunction with the mode shapes to obtain the deformation of the aircraft at a given instant of time. For a typical air-breathing hypersonic vehicle, flexing of the airframe affects the angle of attack and the elevon angle available for control. The angle of attack, measured at the forward tip of the aircraft, is

$$\alpha(t) = \left\{ \frac{\partial \phi_{\bar{u}_3}}{\partial x_1}\bigg|_{x_1=0}^{T} \right\} \boldsymbol{\eta}(t). \tag{9.5}$$

The elevons are the control surfaces for the air-breathing hypersonic vehicle located at the aft region of the aircraft. Flexing of the airframe reduces the effective elevon angle available for control. This loss in control surface angle is equal to the deformation at the aft tip of the aircraft,

$$\theta(t) = \left\{ \frac{\partial \phi_{\bar{u}_3}}{\partial x_1}\bigg|_{x_1=L}^{T} \right\} \boldsymbol{\eta}(t). \tag{9.6}$$

Figure 9.1 presents a comparison between the undamped impulse response computed using the first 5 modes and the first 14 modes, where the angle of attack and the loss of elevon angle are obtained as a function of time. The additional modes included in the model clearly show a significant increase in the angle of attack, while the loss of elevon angle is relatively lower. Every additional mode included will either be in phase or out of phase with respect to the impulse response. This effect can be noticed in Fig. 9.1, where the impulse response with first 5 modes and first 14 modes are out of phase at $t = 0$. Moreover, the additional (higher) modes included increase the frequency of the impulse response.

Although the undamped case shows the need to include higher modes, it is not close to the response observed in flight. The flexing of the airframe in flight is damped out by the aerodynamic forces. In order to take this effect into account, Rayleigh damping is introduced through the generalized force vector in Eq. (9.4).

Figures 9.2 and 9.3 present a comparison for the impulse response with 2% and 5% damping, respectively, using the first 5 modes and the first 14 modes. We can conclude that the effect of higher modes on the angle of attack is significant. Moreover, the shock

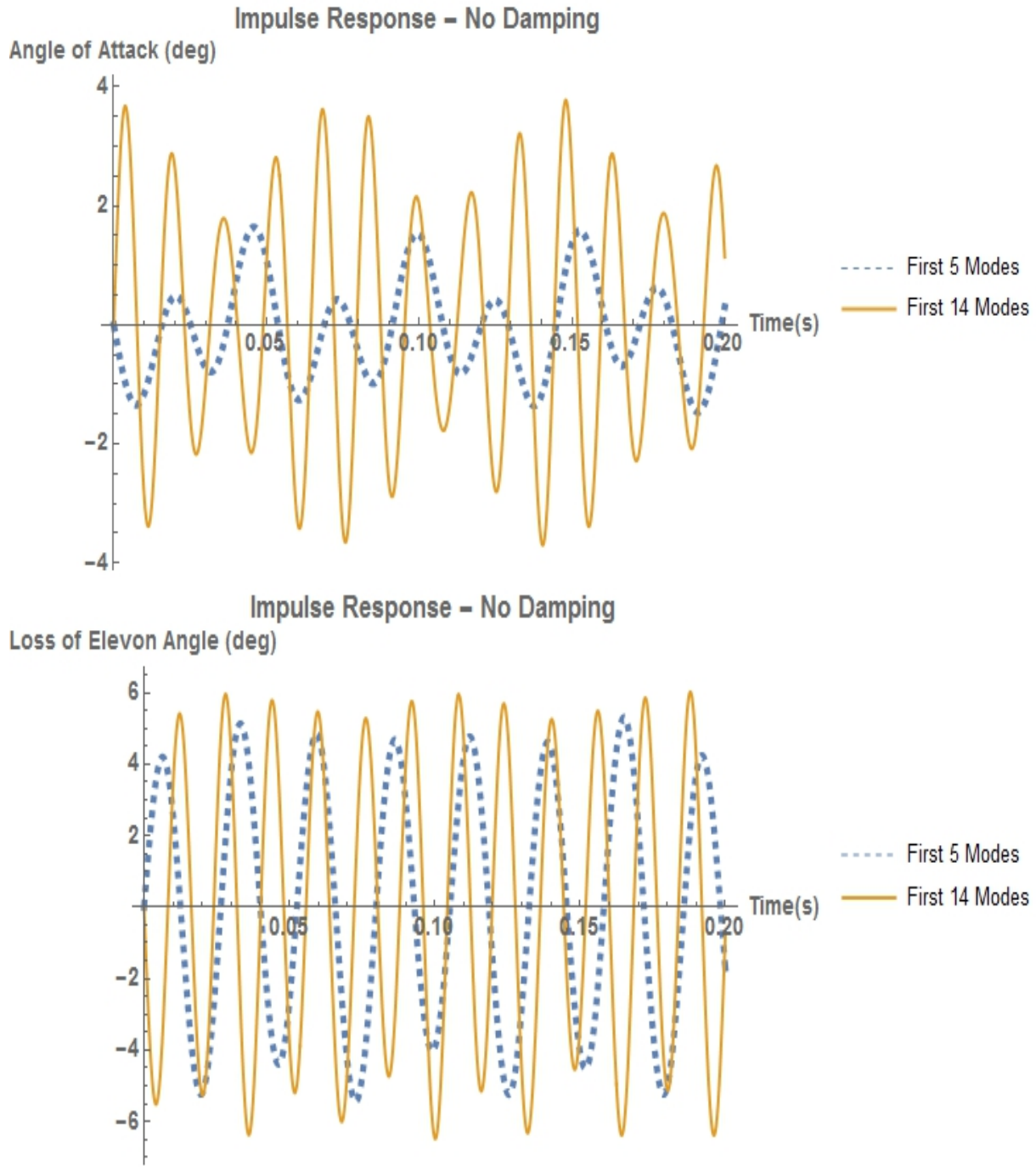

Figure 9.1: A comparison between the undamped impulse response computed using the first 5 modes and the first 14 modes, where the angle of attack and the loss of elevon angle are presented as a function of time.

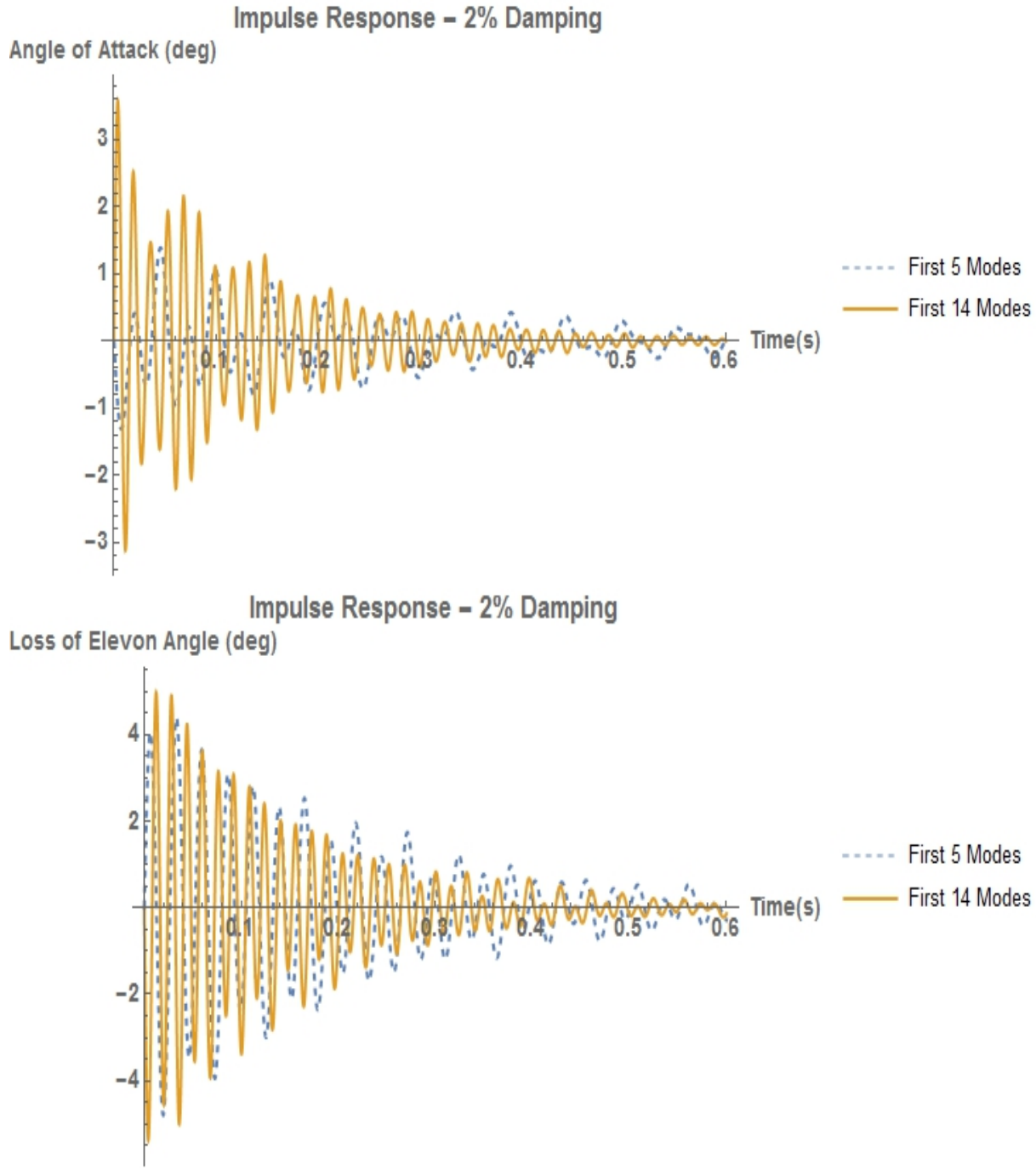

Figure 9.2: A comparison between the impulse response with 2% damping computed using the first 5 modes and the first 14 modes, where the angle of attack and the loss of elevon angle are presented as a function of time.

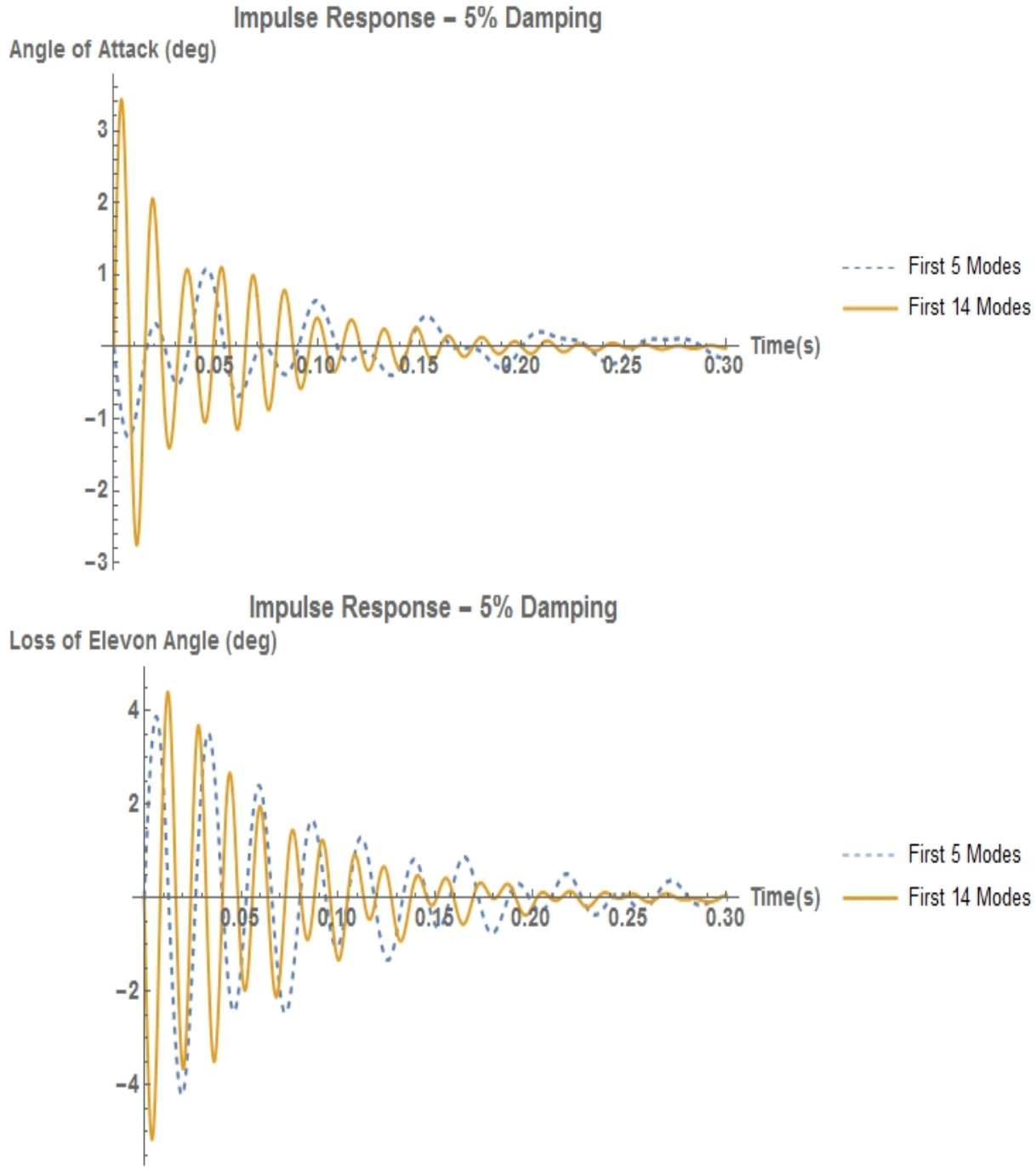

Figure 9.3: A comparison between the impulse response with 5% damping computed using the first 5 modes and the first 14 modes, where the angle of attack and the loss of elevon angle are presented as a function of time.

dynamics are very sensitive to the angle of attack. The nearly twofold increase in the peak overshoot of the response will further have a significant impact on the aerodynamic pressure distribution and the thrust, which in turn will affect the structure's response. The present forced vibration model is not equipped to caputure this coupling effect. However, it can be seen that the effect of the higher modes is significant. On the other hand, the loss of elevon angle due to the higher modes has a marginal effect.

Modal participation factor for a given mode is inversely proportional to the natural frequency of that mode. At higher frequencies this factor would be smaller, making the effect of higher modes insignificant. However, for the case of an air-breathing hypersonic vehicle the natural frequencies are close to each other. The natural frequencies of flexible modes 5 and 14 are 69.29 rad/s and 167.89 rad/s, respectively. This amounts to a percent decrease in $1/\omega_n$ of only 58.73% for a percent increase in natural frequency of 142.3%. In order to put things to perspective, for the case of a free-free Euler-Bernoulli beam the percent decrease in $1/\omega_n$ between 5 and 14 flexible modes is 85.64% for a percent increase in natural frequency of 596.3%. Hence for applications with natural frequencies close to each other, higher vibration modes must be taken into account. Further, higher modes play a significant role in control of lightly damped systems.

Phase II:

Computing Aerodynamic, Thermal, and Control Forces

Chapter 10

Aerodynamic Pressure Distribution

The aerodynamics model implemented in the present work is inherited from Ref. [7] where, oblique shock theory is used for compression and Prandtl-Meyer expansion theory for expansion depending on whether the flow encounters either a concave or a convex corner, respectively. Modeling the aircraft geometry using sharp edges, as shown in Chapter 2, is intentional and is chosen in-part to facilitate making such steady hypersonic flow assumptions, and in-part sharp corners can be mathematically described using piecewise linear functions as opposed to using a curvilinear coordinate system, which significantly simplifies the time spent on integrations involved in computing the aerodynamic forces. The key assumptions made are listed below:

1. Steady inviscid hypersonic flow is assumed throughout the body.
2. It is assumed that the aircraft does not turn in to or away from the flow (side slip neglected).
3. The incident shock wave is assumed to stay attached over the length of the body, which is made possible by choosing a wedge shaped forebody with a sharp leading edge.
4. The oblique shock effects modeled are that of the weak shock only.
5. It is assumed that the air behaves as a perfect gas with a ratio of specific heats, $\gamma = 1.4$.
6. The flow through the diffuser and the exit chamber is assumed to be isentropic (lossless).
7. The flow properties after expansion over a convex corner are determined assuming isentropic flow.
8. The combustion chamber is modeled as a constant area, frictionless duct with heat addition.

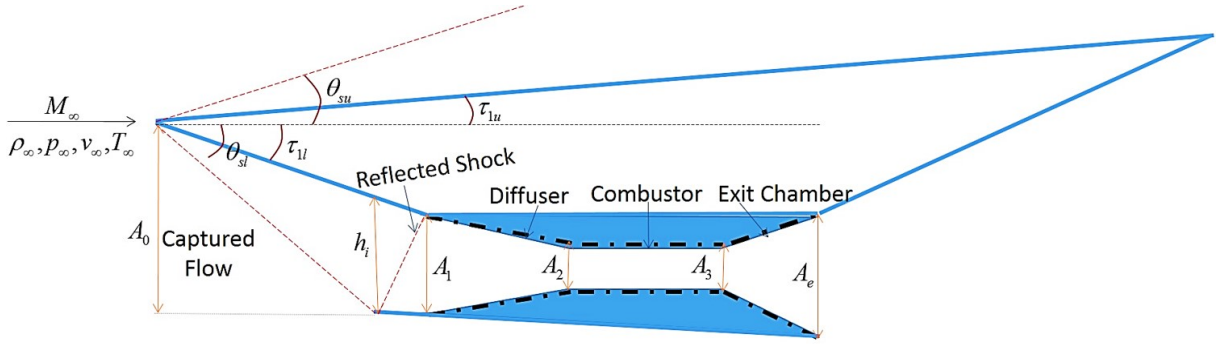

Figure 10.1: Side view of the air-breathing hypersonic vehicle with all the areas and relevant angles clearly labeled, showing the captured flow at zero angle of attack.

9. It is assumed that the mass flow of the fuel is negligible compared to the mass flow of the air.

10. The thrust that is computed using this model is only valid as long as it varies linearly with the fuel equivalence ratio.

11. The design cruise condition is assumed to satisfy the shock on lip condition, at the engine inlet. In other words, the captured flow is completely swallowed by the inlet at the design cruise condition.

Figure 10.1 presents a side view of the air-breathing hypersonic vehicle showing the captured flow incident at zero angle of attack and all the relevant areas and angles clearly labeled.

The flow incident on the sharp leading edge of the AHV would turn the flow on to itself where, the upper surface of the forebody would always see compression due to an oblique shock; while the lower surface experiences compression (oblique shock) if the angle of attack of the incident flow is greater than $-\tau_{1,l}$, and expansion (Prandtl-Meyer expansion theory) if the angle of attack were lesser than or equal to $-\tau_{1,l}$. It is assumed that at design cruise condition the entire oblique shock incident on the engine inlet is swallowed by the inlet and turn the flow parallel to itself. This results in anothther oblique shock, labeled as reflected shock, at the inlet lip of the scramjet engine. This flow that is turned parallel to the inlet passes through the diffuser, which is modeled as a converging nozzle with isentropic flow. The diffuser slows down the supersonic flow enough to achieve combustion in the combustion chamber. The combustion chamber is modeled as a constant area, frictionless duct with heat addition. The flow passes through the exit chamber, which is modeled as a diverging nozzle with isentropic flow. The exhaust then forms a shear layer with the ambient air forming the lower panel for the exhaust nozzle while, the upper panel is that of the aftbody. The subsequent sections clearly detail the expressions used from the literature to compute the aerodynamic pressure, density and temperature profile over the various panels of the air-breathing hypersonic vehicle. It is important to note that these panels experience constant

pressure distribution throughout their length and beadth as they are flat and the associated flow field is modelled as steady flow.

10.1 Oblique Shock Theory

Oblique shock theory is used to compute pressure on the upper forebody panel, pressure immediately after the reflected shock, and pressure on the lower forebody panel when the angle of attack is greater than $-\tau_{1,l}$. In order to compute the shock angle we require the local Mach number, say M_∞ and flow turn angle δ, which is the sum of the lower wedge angle $\tau_{1,l}$ and the angle of attack α for the oblique shock over the lower forebody panel. The shock angle is computed by solving the polynomial equation[7]

$$\sin^6\theta_s + b\sin^4\theta_s + c\sin^2\theta_s + d = 0 \qquad \text{where,} \tag{10.1}$$

$$b = -\frac{M_\infty^2+2}{M_\infty^2} - \gamma\sin^2\delta, \tag{10.2}$$

$$c = \frac{2M_\infty^2+1}{M_\infty^4} + \left(\frac{(\gamma+1)^2}{4} + \frac{\gamma-1}{M_\infty^2}\right)\sin^2\delta, \tag{10.3}$$

$$d = -\frac{\cos^2\delta}{M_\infty^4}. \tag{10.4}$$

Equation (10.1) is a cubic polynomial in $\sin^2\theta_s$ and the solution relevant to present analysis is the second root that corresponds to the weak shock. The expressions for pressure, temperature, and Mach number behind the oblique shock are

$$p_1 = p_\infty\left(\frac{7M_\infty^2\sin^2\theta_s - 1}{6}\right), \tag{10.5}$$

$$T_1 = T_\infty\left(\frac{(7M_\infty^2\sin^2\theta_s - 1)(M_\infty^2\sin^2\theta_s + 5)}{36M_\infty^2\sin^2\theta_s}\right), \tag{10.6}$$

$$M_1 = \frac{1}{|\sin(\theta_s-\delta)|}\sqrt{\frac{M_\infty^2\sin^2\theta_s + 5}{7M_\infty^2\sin^2\theta_s - 1}}, \tag{10.7}$$

respectively.

10.2 Prandtl-Meyer Expansion Theory

When a supersonic fow turns over a convex corner a Prandtl-Meyer expansion fan is generated, which includes an infinite number of Mach waves diverging from a sharp corner. The

Prandtl-Meyer expansion function

$$\nu(M) = \sqrt{\frac{\gamma+1}{\gamma-1}}\tan^{-1}\left(\sqrt{\frac{\gamma+1}{\gamma-1}(M^2-1)}\right) - \tan^{-1}\left(\sqrt{M^2-1}\right) \tag{10.8}$$

determines the angle through which a sonic flow (Mach number =1) must turn over a convex corner to achieve a supersonic Mach number M due to expansion. Hence, a flow turn angle δ can be considered as the angle turned by a sonic flow to achieve the Mach number after expansion M_1 minus the angle turned by a sonic flow to achieve the Mach number before expansion M_0. As we would know the angle by which the flow turns (convex corner angle) and the Mach number before expansion M_0, we can write the angle turned by the sonic flow to achieve the Mach number M_1 after expansion

$$\nu(M_1) = \delta + \nu(M_0) = \sqrt{\frac{\gamma+1}{\gamma-1}}\tan^{-1}\left(\sqrt{\frac{\gamma+1}{\gamma-1}(M_1^2-1)}\right) - \tan^{-1}\left(\sqrt{M_1^2-1}\right) \tag{10.9}$$

By solving the above nonlinear algebraic equation in M_1, we can compute the Mach number after expansion. The expressions for pressure and temperature are

$$p_1 = p_0\left(\frac{1+M_0^2(\gamma-1)/2}{1+M_1^2(\gamma-1)/2}\right)^{\gamma/(\gamma-1)}, \tag{10.10}$$

$$T_1 = T_0\left(\frac{1+M_0^2(\gamma-1)/2}{1+M_1^2(\gamma-1)/2}\right), \tag{10.11}$$

respectively from isentropic flow relations.

10.3 Supersonic Flow through a Converging/Diverging Nozzle

In order to model the flow through a converging/diverging nozzle, the continuity equation (conservation of mass) is used to determine the Mach number after the flow passes through the diffuser and the exit chamber, which are modeled as converging and diverging nozzles, respectively. The flow is assumed to be isentropic within these chambers. The area ratio A_r is defined as the ratio of the exit area of the chamber to the inlet area of the chamber. It is important to note that the area ratio for the converging nozzle is less than 1, while the area ratio for the diverging nozzle is greater than 1. The continuity equation across a converging/diverging nozzle with an initial Mach number M_0 before entering the chamber and a Mach number M_1 at the exit point of the chamber is

$$\frac{(1+M_0^2(\gamma-1)/2)^{(\gamma+1)/(\gamma-1)}}{M_0^2} = A_r\frac{(1+M_1^2(\gamma-1)/2)^{(\gamma+1)/(\gamma-1)}}{M_1^2}. \tag{10.12}$$

The above nonlinear algebraic equation in M_1 is solved to compute the Mach number at the exit point of the chamber. The pressure and temperature from isentropic flow relations are

$$p_1 = p_0 \left(\frac{1 + M_0^2(\gamma - 1)/2}{1 + M_1^2(\gamma - 1)/2} \right)^{\gamma/(\gamma-1)}, \tag{10.13}$$

$$T_1 = T_0 \left(\frac{1 + M_0^2(\gamma - 1)/2}{1 + M_1^2(\gamma - 1)/2} \right), \tag{10.14}$$

respectively.

10.4 Supersonic Combustion

The combustion chamber is modeled as a constant area, frictionless duct with heat addition, where Rayleigh flow is used to model the effect of heat addition. Rayleigh flow describes the change in Mach number with respect to the change in stagnation temperature T_0 using the differential equation

$$\frac{dM^2}{dM} = \frac{1 + \gamma M^2}{1 - M^2} \left(1 + \frac{\gamma - 1}{2} M^2 \right) \frac{dT_0}{T_0}. \tag{10.15}$$

The solution to the above equation is

$$\frac{T_0}{T_0^*} = \frac{2(\gamma + 1)M^2}{(1 + \gamma M^2)^2} \left(1 + \frac{\gamma - 1}{2} M^2 \right) \tag{10.16}$$

where, T_0^* is the stagnation temperature at which the flow through the duct would start thermally choking and is a constant for a given case. Thermal choking is a phenomenon typically observed when a supersonic flow turns subsonic or a subsonic flow turns supersonic inside a duct due to heat addition. In case of supersonic flows, heat addition lowers the Mach number eventually making the flow subsonic. In case of subsonic flows, heat addition increases the Mach number eventually making the flow supersonic. The former case is relevant to the phenomenon observed in scramjet engines. Adding heat to a flow in a constant area duct increases the total enthalpy of the system, which in turn increases the total stagnation temperature. In the following analysis subscript *ac* refers to conditions after combustion and subscript *bc* refer to conditions before combustion. The effect of heat addition is captured in the equation for stagnation temperatures before and after combustion

$$(T_0)_{ac} = (T_0)_{bc} + \Delta T. \tag{10.17}$$

By dividing the above equation with T_0^*

$$\frac{(T_0)_{ac}}{T_0^*} = \frac{(T_0)_{bc}}{T_0^*} + \frac{\Delta T}{T_0^*} \tag{10.18}$$

From Eq. (10.16),

$$\frac{2(\gamma+1)M_{ac}^2}{(1+\gamma M_{ac}^2)^2}\left(1+\frac{\gamma-1}{2}M_{ac}^2\right)=\frac{2(\gamma+1)M_{bc}^2}{(1+\gamma M_{bc}^2)^2}\left(1+\frac{\gamma-1}{2}M_{bc}^2\right)+\frac{\Delta T}{T_0^*}, \tag{10.19}$$

$$\frac{1}{T_0^*}=\frac{1}{(T_0)_{bc}}\frac{2(\gamma+1)M_{bc}^2}{(1+\gamma M_{bc}^2)^2}\left(1+\frac{\gamma-1}{2}M_{bc}^2\right). \tag{10.20}$$

Eliminating T_0^* from the above equations and using the relationship between stagnation and static temperatures

$$(T_0)_{bc}=T_{bc}\left(1+\frac{\gamma-1}{2}M_{bc}^2\right), \tag{10.21}$$

we have

$$\frac{M_{ac}^2}{(1+\gamma M_{ac}^2)^2}\left(1+\frac{\gamma-1}{2}M_{ac}^2\right)=\frac{M_{bc}^2}{(1+\gamma M_{bc}^2)^2}\left(1+\frac{\gamma-1}{2}M_{bc}^2\right)+\frac{M_{bc}^2}{(1+\gamma M_{bc}^2)^2}\left(\frac{\Delta T}{T_{bc}}\right). \tag{10.22}$$

However, we do not have direct control over ΔT and hence, we represent the heat adiition term in the above equation in terms of the normalized fuel equivalence ratio Φ,

$$\frac{\Delta T}{T_{bc}}=f_{st}\Phi\left(\frac{H_f\eta_c/T_{bc}-\left(1+\frac{\gamma-1}{2}M_{bc}^2\right)}{1+f_{st}\Phi}\right) \tag{10.23}$$

where, f_{st} is the stochiometric fuel to air ratio, η_c is the combustor efficiency, c_p is the specific heat, and H_f is the fuel lower heating value. By solving the nonlinear algebraic Eqs. (10.22) and (10.23), we can compute the Mach number after combustion. The pressure and temperature after combustion are

$$p_{ac}=p_{bc}\left(\frac{1+\gamma M_{bc}^2}{1+\gamma M_{ac}^2}\right), \tag{10.24}$$

$$T_{ac}=T_{bc}\left(\frac{M_{ac}^2(1+\gamma M_{bc}^2)}{M_{bc}^2(1+\gamma M_{ac}^2)}\right), \tag{10.25}$$

respectively.

10.5 Lower Aftbody Panel

The exhaust plume from the exit chamber of the scramjet engine forms a shear layer with the freestream flow forming the lower surface of the exhaust nozzle. While the lower aftbody panel forms the upper surface of the exhaust nozzle. The shear layer is formed due to balalncing of the plume and freestream pressures. Therefore, the pressure distribution along

Table 10.1: Table of constants for the atmospheric model.

Profile	Alt Range (k ft)	Base Alt, h_0 (ft)	p_0 (lb-f/ft^2)	T_0 (^{0}R)	ρ_0 (slug/ft^3)	K_0 (^{0}R/ft)
1	$0-36$	36089.239	2116.22	518.67	0.00237691	-0.00356616
2	$36-65$	65616.798	472.6758	389.97	0.0007061	0
1	$65-104$	104986.878	114.343	389.97	0.0001708	0.00054864
1	$104-154$	154199.475	18.12831	411.57	2.566003×10^{-5}	-0.00356616
2	$154-170$	170603.675	2.31620	487.17	2.76975×10^{-6}	0
1	$170-200$	200131.234	1.23219	487.17	1.47347×10^{-6}	-0.00109728
1	$200-259$	259186.352	0.3803	454.17	4.87168×10^{-7}	-0.00219456
2	$259-295$	295000	0.0215739	325.17	3.867149×10^{-8}	0

the aftbody panel is a function of the position of the shear layer. A reasonable approximation for the aftbody pressure distribution is presented in Ref. [**?**]

$$p_a(x_1) = \frac{p_e}{1 + (x_1 - L_f - L_n)\tan(\tau_2 + \tau_{1,u})/L_a(p_e/p_\infty - 1)} \tag{10.26}$$

where, x_1 is the coordinate along the longitudinal axis.

10.6 Atmospheric Model

The present analysis requires trimming the air-breathing hypersonic vehicle at a wide range of altitudes. Hence, it is important to choose an atmospheric model that can estimate the freestream conditions for altitudes ranging from $85,000$ ft to $110,000$ ft. The following atmospheric model estimates freestream conditions upto 295, 000 ft, popular for modeling the dynamics of reentry vehicles.[60] The freestream temperature, pressure, and density at a given altitude are

1. Profile 1:

$$T_\infty = T_0\left(1 + K_0\left(\frac{h_g - h_0}{T_0}\right)\right), \tag{10.27}$$

$$p_\infty = p_0\left(1 + K_0\left(\frac{h_g - h_0}{T_0}\right)\right)^{-g/(K_0 R)}, \tag{10.28}$$

$$\rho_\infty = \rho_0\left(1 + K_0\left(\frac{h_g - h_0}{T_0}\right)\right)^{-g/(K_0 R)-1}, \tag{10.29}$$

2. Profile 2:

$$T_\infty = T_0, \tag{10.30}$$
$$p_\infty = p_0 \exp^{-g(h_g - h_0)/(T_0 R)}, \tag{10.31}$$
$$\rho_\infty = \rho_0 \exp^{-g(h_g - h_0)/(T_0 R)}, \tag{10.32}$$

where, the geopotential altitiude

$$h_g = \frac{h R_e}{h + R_e}, \tag{10.33}$$

g is the acceleration due to gravity, and R is the specific gas constant.

10.7 Computing Thrust: A Test Case

The expression for the thrust is obtained from the momentum therorem from fluid mechanics applied to a control volume that houses the scramjet engine. The expression for the thrust includes the propulsive force generated due to the ejected mass and the inlet drag. The thrust per unit width of the inlet is

$$\mathcal{T} = \dot{m}_a (V_e - V_\infty) + (p_e - p_\infty) A_e - (p_1 - p_\infty) h_i \tag{10.34}$$

where, $\dot{m}_a$ is the captured mass flow rate, V_e is the exhaust velocity, V_∞ is the velocity of the captured freestream flow, p_e is the pressure past the exit chamber, p_1 is the pressure before the reflected shock, p_∞ is the freestream pressure, A_e is the area per unit width of the exit chamber, and h_i is the inlet height. A test case of the thrust computations are presented below, at the following conditions

$\alpha = 0^o$, $M_\infty = 10$, $h = 110,000\,\text{ft}$, $\phi = 1.0$, $\tau_{1,l} = 6.2^o$, $\gamma = 1.4$, $L_f = 47\,\text{ft}$, $h_i = 3.25\,\text{ft}$, $A_n = 2.9$, $A_d = 0.1$, $A_e = 0.449\,\text{ft}$, $\delta_l = \tau_{1,l} + \alpha$ (Flow-turn Angle), $A_1 = 1.5493\,\text{ft}$.

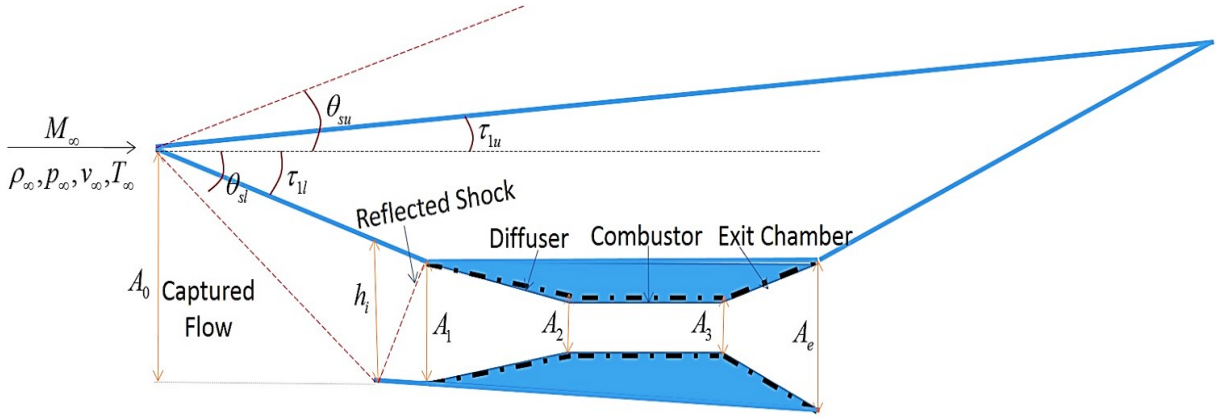

Figure 10.2: Side view of the air-breathing hypersonic vehicle with all the areas clearly labeled.

From oblique shock theory,

$$\sin^6\theta_s + b\sin^4\theta_s + c\sin^2\theta_s + d = 0$$

$$b = -\frac{M_\infty^2+2}{M_\infty^2} - \gamma\sin(\delta_l) = -1.03633$$

$$c = \frac{2M_\infty^2+1}{M_\infty^4} + \left[\frac{(\gamma+1)^2}{4} + \frac{\gamma-1}{M_\infty^2}\right]\sin^2\delta_l = 0.0369426$$

$$d = -\frac{\cos^2\delta_l}{M_\infty^4} = -0.0000988336$$

$$\theta_s = 10.6178^o$$

$$\tan^{-1}\left(\frac{L_f\tan(\tau_{1,l}) + h_i}{L_f}\right) = 10.3761^o \approx \theta_s \quad \text{(Shock on lip condition satisfied!)}$$

$$p_\infty = 14.8354\,\text{lb-f/ft}^2$$

$$T_\infty = 418.388\,^oR$$

$$p_l = p_\infty\left(\frac{7M_\infty^2\sin^2\theta_s - 1}{6}\right) = 55.6272\,\text{lb-f/ft}^2$$

$$T_l = T_\infty\left(\frac{(7M_\infty^2\sin^2\theta_s - 1)(M_\infty^2\sin^2\theta_s + 5)}{36M_\infty^2\sin^2\theta_s}\right) = 650.921\,^oR$$

$$M_l = \frac{1}{\sin(\theta_s - \delta_l)}\sqrt{\frac{M_\infty^2\sin^2\theta_s + 5}{7M_\infty^2\sin^2\theta_s - 1}} = 8.02209$$

When this oblique shock impinges on the lip of the nacelle, there will be a reflected shock which turns the flow parallel to the nacelle.

$$\begin{aligned}
\delta_1 &= \theta_s - \alpha \\
\sin^6\theta_1 + b_1\sin^4\theta_1 + c_1\sin^2\theta_1 + d_1 &= 0 \\
b_1 &= -\frac{M_l^2+2}{M_l^2} - \gamma\sin(\delta_1) \\
c_1 &= \frac{2M_l^2+1}{M_l^4} + \left[\frac{(\gamma+1)^2}{4} + \frac{\gamma-1}{M_l^2}\right]\sin^2\delta_1 \\
d_1 &= -\frac{\cos^2\delta_1}{M_l^4} \\
\theta_1 &= 11.7891^o
\end{aligned}$$

$$\begin{aligned}
p_1 &= p_l\left(\frac{7M_l^2\sin^2\theta_1 - 1}{6}\right) = 165.065\,\text{lb-f/ft}^2 \\
T_1 &= T_l\left(\frac{(7M_l^2\sin^2\theta_1 - 1)(M_l^2\sin^2\theta_1 + 5)}{36M_l^2\sin^2\theta_1}\right) = 921.103\,^oR \\
M_1 &= \frac{1}{\sin(\theta_1-\delta_1)}\sqrt{\frac{M_l^2\sin^2\theta_1 + 5}{7M_l^2\sin^2\theta_1 - 1}} = 6.74638.
\end{aligned}$$

Using the results from flow through a frictionless converging duct,

$$\begin{aligned}
A_d &= 0.1 \\
\frac{\left(1+\frac{\gamma-1}{2}M_2^2\right)^{(\gamma+1)/(\gamma-1)}}{M_2^2} &= A_d^2\frac{\left(1+\frac{\gamma-1}{2}M_1^2\right)^{(\gamma+1)/(\gamma-1)}}{M_1^2} \\
M_2 &= 3.78697 \\
p_2 &= p_1\left(\frac{1+\frac{\gamma-1}{2}M_1^2}{1+\frac{\gamma-1}{2}M_2^2}\right)^{\gamma/(\gamma-1)} = 4752.21\,\text{lb-f/ft}^2 \\
T_2 &= T_1\left(\frac{1+\frac{\gamma-1}{2}M_1^2}{1+\frac{\gamma-1}{2}M_2^2}\right) = 2405.66\,^oR
\end{aligned}$$

Using the results from flow through a constant area, frictionless duct with heat addition,

$$H_f = 51,500\,\text{BTU/lbm}, \quad f_{st} = 0.0291, \quad c_p = 0.24\,\text{BTU/(lbm}^o\text{R)}, \quad \eta_c = 0.9$$

$$\frac{\Delta T_t}{T_{t2}} = \frac{T_{t3}}{T_{t2}} - 1 = \frac{1 + H_f \eta_c f_{st}\phi/(c_p T_{t2})}{1 + f_{st}\phi} - 1 = \frac{f_{st}\phi}{1 + f_{st}\phi}\left(\frac{H_f \eta_c}{c_p T_{t2}} - 1\right)$$

$$\Delta T_t = \frac{f_{st}\phi}{1 + f_{st}\phi}\left(\frac{H_f \eta_c}{c_p} - T_{t2}\right) \quad \text{(Total change in temperature)}$$

$$\frac{\Delta T_t}{T_2} = \frac{f_{st}\phi}{1 + f_{st}\phi}\left(\frac{H_f \eta_c}{c_p T_2} - \frac{T_{t2}}{T_2}\right) = \frac{f_{st}\phi}{1 + f_{st}\phi}\left(\frac{H_f \eta_c}{c_p T_2} - \left(1 + \frac{\gamma - 1}{2} M_2^2\right)\right)$$

$$\frac{M_3^2\left(1 + \frac{\gamma-1}{2} M_3^2\right)}{(\gamma M_3^2 + 1)^2} = \frac{M_2^2\left(1 + \frac{\gamma-1}{2} M_2^2\right)}{(\gamma M_2^2 + 1)^2} + \frac{M_2^2}{(\gamma M_2^2 + 1)^2}\frac{\Delta T_t}{T_2}$$

$$M_3 = 1.40038$$

$$p_3 = p_2 \frac{1 + \gamma M_2^2}{1 + \gamma M_3^2} = 26743\,\text{lb-f/ft}^2$$

$$T_3 = T_2 \frac{M_3^2}{M_2^2}\left(\frac{1 + \gamma M_2^2}{1 + \gamma M_3^2}\right)^2 = 10417.6\,^o R$$

Using the results from flow through a frictionless diverging duct,

$$\frac{\left(1 + \frac{\gamma-1}{2} M_e^2\right)^{(\gamma+1)/(\gamma-1)}}{M_e^2} = A_n^2 \frac{\left(1 + \frac{\gamma-1}{2} M_3^2\right)^{(\gamma+1)/(\gamma-1)}}{M_3^2}$$

$$M_e = 2.71672$$

$$p_e = p_3\left(\frac{1 + \frac{\gamma-1}{2} M_3^2}{1 + \frac{\gamma-1}{2} M_e^2}\right)^{\gamma/(\gamma-1)} = 3564.33\,\text{lb-f/ft}^2$$

$$T_e = T_3\left(\frac{1 + \frac{\gamma-1}{2} M_3^2}{1 + \frac{\gamma-1}{2} M_e^2}\right) = 5857.37\,^o R$$

Computing thrust from Mach numbers and pressures,

$$R = 1716.49 \text{ ft lb-f slug}^{-1\,o}\text{R}^{-1}$$

$$c(T) = \sqrt{\gamma R T} \text{ ft/s}$$

$$A_0 = h_i \frac{\sin\theta_s \cos\delta_l}{\sin(\theta_s - \delta_l)} = 7.79179\,\text{ft}$$

$$\dot{m}_a = \left(\frac{p_\infty}{R T_\infty}\right) A_0 M_\infty c(T_\infty)$$

$$V_e - V_\infty = M_e\, c(T_e) - M_\infty\, c(T_\infty)$$

$$\mathcal{T} = \dot{m}_a(V_e - V_\infty) + (p_e - p_\infty)A_e - (p_1 - p_\infty)h_i = 1629.05\,\text{lb-f/ft}$$

Chapter 11

Control Surface Forces

The air-breathing hypersonic vehicle has four control surfaces; two elevons and two rudders located at the aft region of the aircraft as shown in Fig. 11.1. Along with the fuel equivalence ratio responsible for generating thrust, we have a total of five control inputs making the system underactuated.

The control surfaces are modeled as rigid flat plates, hinged at the mid-chord location and are free to rotate about their axis. Although the hinged point on the flexible airframe can deform in flight, accounting for the flexibility effect of the structure as a whole on the control surface. The airframe's deformation reduces the total available control surface deflection for implementing closed-loop control. It is assumed that all the control surfaces are located wide enough on the fuselage so that the freestream hypersonic flow would be incident on the control surfaces, as opposed to a mixture of freestream and associated flow field over the airframe.

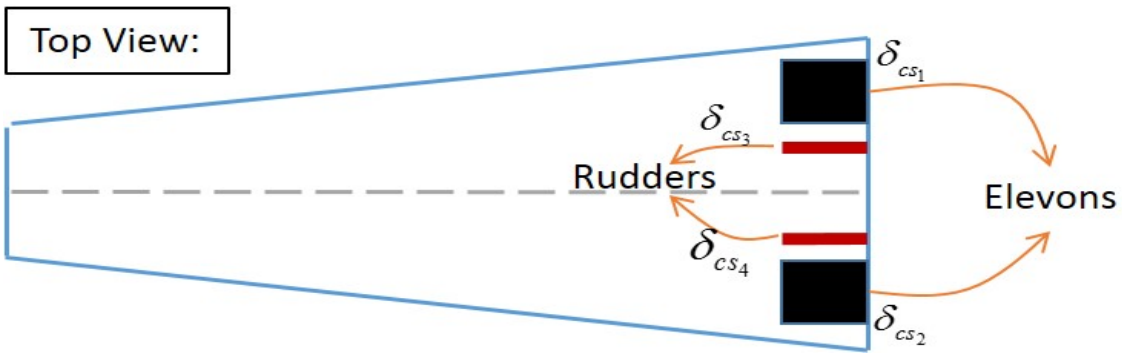

Figure 11.1: Top view of the air-breathing hypersonic vehicle showing the location of the four control surfaces.

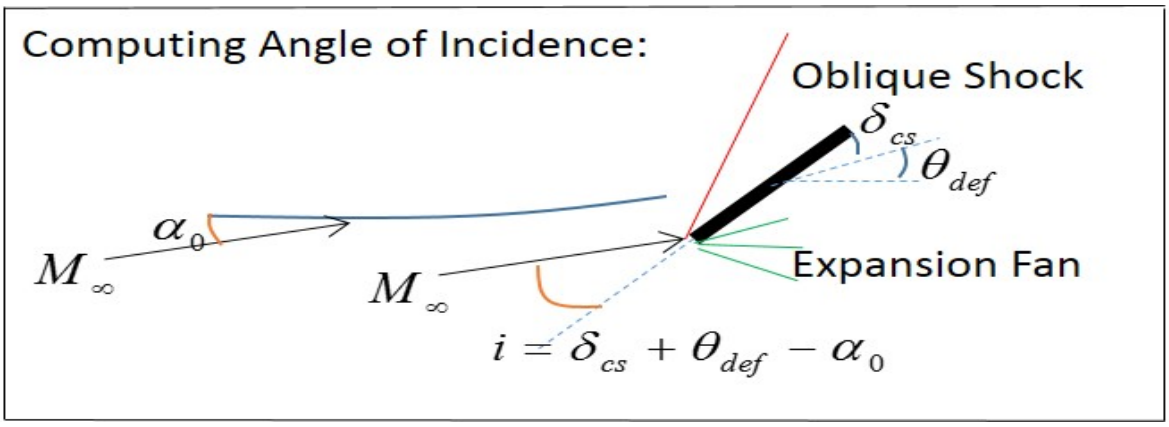

Figure 11.2: Side view of the neutral axis and the elevon, showing the angle of incidence.

11.1 Elevons

Figure 11.2 shows a side view of the elevon with the effect of the neutral axis bending captured through the angle θ_{def}. The blue line is the neutral axis and the black slab is the elevon, where α_0 is the angle of attack of the undeformed aircraft, M_∞ is the freestream Mach number, δ_{cs} is the deflection of the elevon about its mid chord point, θ_{def} is the angle with which the neutral axis deforms at the hinged location as shown in Fig. 11.3, and i is the angle of incidence of the local flow with respect to the elevon. When the angle of incidence is greater than zero, the upper surface experiences compression due to an oblique shock as described in Section 10.1 and the lower surface sees a Prandtl-Meyer expansion fan as described in Section 10.2. When the angle of incidence is less than zero, the upper surfaces experiences expansion and the lower surface experiences compression.

11.2 Rudders

The rudders are modeled as flat plates hinged about their mid point and rotated freely about the vertical axis. Both the surfaces of the rudder would experience compression due to an oblique shock as described in Section 10.1.When the angle of incidence is greater than zero, the inward surface experiences compression due to an oblique shock as described in Section 10.1 and the outward surface sees a Prandtl-Meyer expansion fan as described in Section 10.2. When the angle of incidence is less than zero, the outward surface experiences expansion and the inward surface experiences compression. The displacement of the rudders due to fuselage deformation is given by γ_{def} as shown in Fig. 11.4

The location and size of It is important to note that the flexibility effects of the control surface and the loss of controllability associated with it are neglected. Also, complex

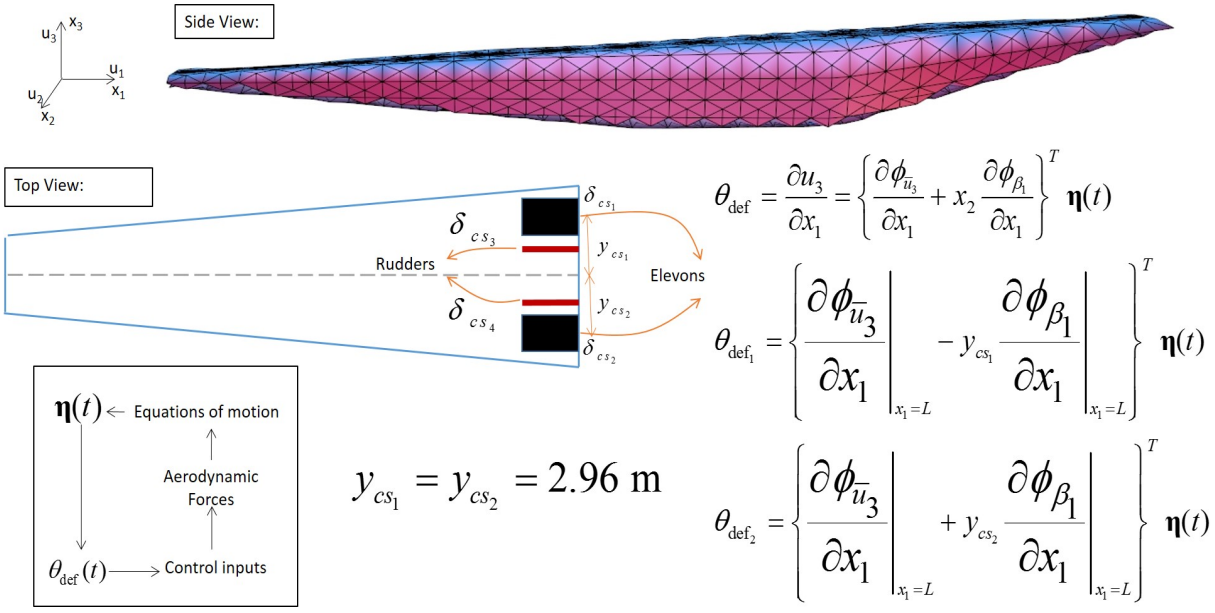

Figure 11.3: Top view of the air-breathing hypersonic vehicle showing the location of the four control surfaces.

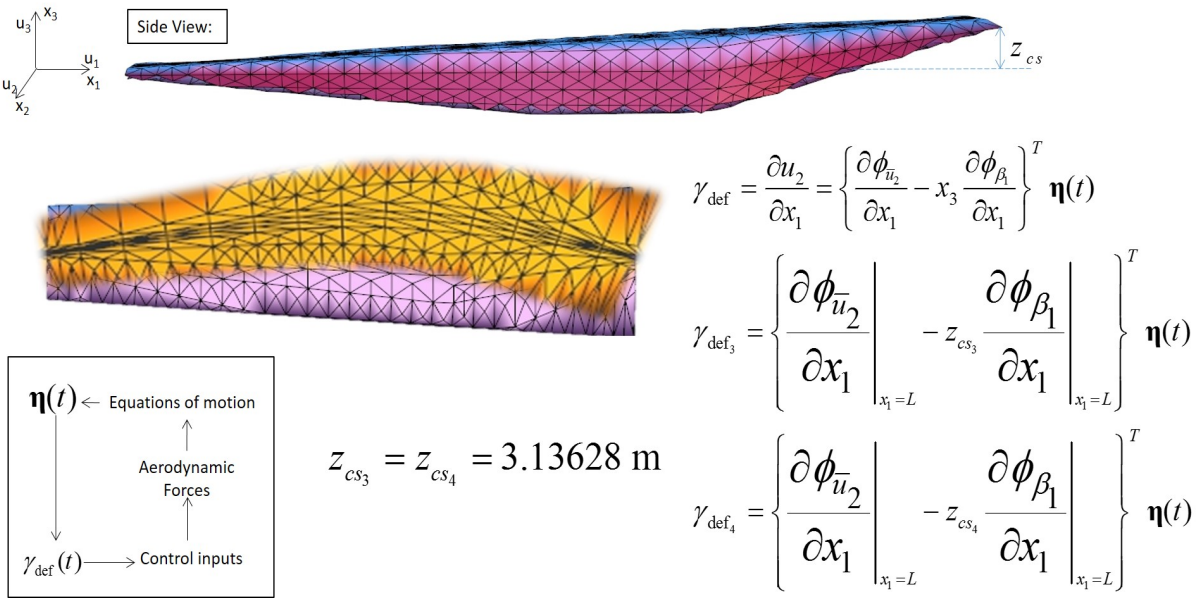

Figure 11.4: Top view of the air-breathing hypersonic vehicle showing the location of the four control surfaces.

phenomenon like control surface flutter are not captured using this model.

Phase III:

Deriving Nonlinear Equations of Motion

Chapter 12

Lagrangian Approach - Internal Forces

The primary difference between the free vibration problem and the forced vibration problem is the introduction of applied forces. Since the aircraft is modeled as a free-free thin-walled structure, the body fixed frame of reference will experience acceleration due to these applied forces, which is a consequence of Newton's second law of motion. Therefore, the body fixed frame is a noninertial frame of reference and a suitable inertial frame must be chosen. Moreover, the surface of the earth is assumed to be flat and the effect of its rotation on the dynamics of the aircraft is neglected. Hence, it would be appropriate to choose an inertial ground frame of reference, which is fixed to the surface of the earth and moves at a constant velocity with the aircraft, as the dynamics of the aircraft about the cruise condition is considered.

Figure 12.1 shows the location of the body fixed frame, henceforth referred to as the vehicle frame V, relative to the inertial ground frame I, where the position and orientation of V with respect to I are given by vectors $\mathbf{p}_v$ and $\boldsymbol{\theta}_{V,I}$ respectively.

12.1 Kinetic Energy

Consider a point P on the body of the aircraft whose location is given by the vector $\mathbf{p}'$ with respect to I and vector $\mathbf{p}$ with respect to V as shown in Fig. 12.1. The vector $\mathbf{p}$ gives the instantaneous position of the point P on a flexible structure, which can be decomposed into

$$\left(\mathbf{p}\,\middle|_{\mathrm{V}}\right) = \left(\mathbf{p}_{RB}\,\middle|_{\mathrm{V}}\right) + \left(\mathbf{d}_E\,\middle|_{\mathrm{V}}\right), \tag{12.1}$$

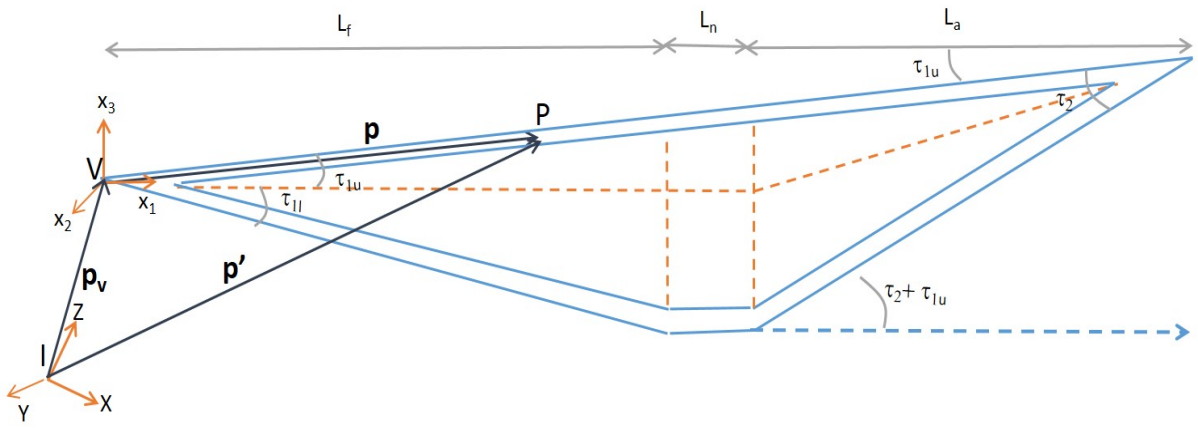

Figure 12.1: Location of vehicle frame and ground frame (Figure not to scale).

where $\mathbf{p}_{RB}$ is the position vector of the point P on the undeformed aircraft and $\mathbf{d}_E$ is the deformation at that location. From Fig. 12.1, the location of P with respect to I is given by

$$\left(\mathbf{p}' \Big|_{\mathrm{I}}\right) = \left(\mathbf{p}_v \Big|_{\mathrm{I}}\right) + \left(\mathbf{p} \Big|_{\mathrm{V}}\right) \tag{12.2}$$

$$= \left(\mathbf{p}_v \Big|_{\mathrm{I}}\right) + \left(\mathbf{p_{RB}} \Big|_{\mathrm{V}}\right) + \left(\mathbf{d_E} \Big|_{\mathrm{V}}\right) \tag{12.3}$$

$$= \left(\mathbf{p}_v \Big|_{\mathrm{I}}\right) + \left(R\,\mathbf{p_{RB}} \Big|_{\mathrm{I}}\right) + \left(\mathbf{d_E} \Big|_{\mathrm{V}}\right), \tag{12.4}$$

where, $R(\boldsymbol{\theta}_{V,I})$ is a rotation matrix that transforms a vector from the vehicle frame V to the inertial frame I. Moreover, the deformation $\mathbf{d}_E$ is expressed as

$$\left(\mathbf{d_E} \Big|_{\mathrm{V}}\right) = \left(\Phi\,\boldsymbol{\eta} \Big|_{\mathrm{V}}\right), \tag{12.5}$$

where Φ is a $3 \times n$ matrix of mode shape functions and $\boldsymbol{\eta}$ is an $n \times 1$ vector of modal coordinates. The location of P with respect to I can be expressed as

$$\left(\mathbf{p}' \Big|_{\mathrm{I}}\right) = \left(\mathbf{p}_v \Big|_{\mathrm{I}}\right) + \left(R\,\mathbf{p_{RB}} \Big|_{\mathrm{I}}\right) + \left(\Phi\,\boldsymbol{\eta} \Big|_{\mathrm{V}}\right), \tag{12.6}$$

where $\mathbf{p}_{RB}$ is obtained from the geometry of the vehicle in Chapter 2 and Φ is obtained from the free vibration mode shapes computed in Chapter 7. Hence, the location of any point P on the aircraft with respect to I can be expressed in terms of $\mathbf{p}_v$, $\boldsymbol{\theta}_{V,I}$, and $\boldsymbol{\eta}$. The location of all points on the aircraft at a given instant of time is called the configuration of the vehicle and a generalized coordinate vector is composed of variables required to define

this configuration. The generalized coordinate vector $\mathbf{q}$ has size $6+n$ and is given by

$$\mathbf{q} = \left\{ \begin{array}{c} \mathbf{p}_v \\ \boldsymbol{\theta}_{V,I} \\ \boldsymbol{\eta} \end{array} \right\}. \tag{12.7}$$

Since $\mathbf{q}(t)$ describes the configuration of the vehicle for all time, the kinetic energy T of the vehicle is expressed in terms of $\dot{\mathbf{q}}$ and $\mathbf{q}$ by

$$T(\dot{\mathbf{q}},\, \mathbf{q}) = \frac{1}{2}\dot{\mathbf{q}}^T \mathcal{M}(\mathbf{q})\dot{\mathbf{q}}, \tag{12.8}$$

where

$$\mathcal{M}(\mathbf{q}) = \left(\begin{array}{ccc} m\,\mathbb{I}_{3\times 3} & \left(I_p + I_d(\boldsymbol{\eta})\right)_{3\times 3} & \left(I_\Phi\right)_{3\times n} \\ \left(I_p^T + I_d^T(\boldsymbol{\eta})\right)_{3\times 3} & \left(I_{pp} + I_{dd}(\boldsymbol{\eta}) + (I_{pd}(\boldsymbol{\eta}) + I_{pd}^T(\boldsymbol{\eta}))\right)_{3\times 3} & \left(I_{p\Phi} + I_{d\Phi}(\boldsymbol{\eta})\right)_{3\times n} \\ \left(I_\Phi^T\right)_{n\times 3} & \left(I_{p\Phi}^T + I_{d\Phi}^T(\boldsymbol{\eta})\right)_{n\times 3} & \left(I_{\Phi\Phi}\right)_{n\times n} \end{array} \right), \tag{12.9}$$

$$I_p = \int_V \left(\mathbf{p}_{RB}{}^\times\right)^T \rho\, dV + \int_{V_{ns}} \left(\mathbf{p}_{RB}{}^\times\right)_{ns}^T \rho_{ns}\, dV_{ns}, \tag{12.10}$$

$$I_d = \int_V \left(\mathbf{d}_E{}^\times\right)^T \rho\, dV, \tag{12.11}$$

$$I_\Phi = \int_V \Phi\rho\, dV, \tag{12.12}$$

$$I_{pp} = \int_V \left(\mathbf{p}_{RB}{}^\times\right)^T \left(\mathbf{p}_{RB}{}^\times\right) \rho\, dV + \int_{V_{ns}} \left(\mathbf{p}_{RB}{}^\times\right)_{ns}^T \left(\mathbf{p}_{RB}{}^\times\right)_{ns} \rho_{ns}\, dV_{ns}, \tag{12.13}$$

$$I_{dd} = \int_V \left(\mathbf{d}_E{}^\times\right)^T \left(\mathbf{d}_E{}^\times\right) \rho\, dV, \tag{12.14}$$

$$I_{pd} = \int_V \left(\mathbf{p}_{RB}{}^\times\right)^T \left(\mathbf{d}_E{}^\times\right) \rho\, dV, \tag{12.15}$$

$$I_{p\Phi} = \int_V \left(\mathbf{p}_{RB}{}^\times\right) \Phi\rho\, dV, \tag{12.16}$$

$$I_{d\Phi} = \int_V \left(\mathbf{d}_E{}^\times\right) \Phi\rho\, dV, \tag{12.17}$$

$$I_{\Phi\Phi} = \int_V \Phi^T\Phi\rho\, dV, \tag{12.18}$$

$\mathbb{I}_{3\times 3}$ is a 3×3 identity matrix, and $(\mathbf{y}^\times)$ is a 3×3 skew symmetric matrix such that $(\mathbf{y}^\times)\mathbf{w} = \vec{\mathbf{y}} \times \vec{\mathbf{w}}$ where $\mathbf{y}$ and $\mathbf{w}$ are 3-dimensional vectors. The terms due to the subscript ns arise due to the kinetic energy of the rigid nonstructural mass.

12.2 Elastic Strain Energy

The elastic strain energy U_e possessed by the vehicle is given by

$$U_e(\mathbf{q}) = \frac{1}{2}\boldsymbol{\eta}^T \left[\Omega^2 \mathbf{I}_{\Phi\Phi}\right] \boldsymbol{\eta}, \tag{12.19}$$

where Ω is an $n \times n$ diagonal matrix of natural frequencies for the first n significant modes computed in Chapter 7. The derivation for Eq. (12.19) is obtained from first principles using the definition of strain energy

$$U_e = \frac{1}{2}\int_V \boldsymbol{\sigma}^T \boldsymbol{\epsilon}\, dV, \tag{12.20}$$

where

$$\boldsymbol{\sigma} = \begin{Bmatrix} \sigma_{xx} \\ \sigma_{yy} \\ \sigma_{zz} \\ \sigma_{yz} \\ \sigma_{xz} \\ \sigma_{xy} \end{Bmatrix} \quad \text{and} \quad \boldsymbol{\epsilon} = \begin{Bmatrix} \epsilon_{xx} \\ \epsilon_{yy} \\ \epsilon_{zz} \\ \gamma_{yz} \\ \gamma_{xz} \\ \gamma_{xy} \end{Bmatrix}.$$

Expanding the expression for strain energy yields

$$\begin{aligned} U_e = &\frac{1}{2}\int_V \sigma_{xx}\epsilon_{xx}\, dV + \frac{1}{2}\int_V \sigma_{yy}\epsilon_{yy}\, dV + \frac{1}{2}\int_V \sigma_{zz}\epsilon_{zz}\, dV \\ &+ \frac{1}{2}\int_V \sigma_{xy}\gamma_{xy}\, dV + \frac{1}{2}\int_V \sigma_{zx}\gamma_{zx}\, dV + \frac{1}{2}\int_V \sigma_{yz}\gamma_{yz}\, dV. \end{aligned} \tag{12.21}$$

Substituting the strain-displacement relations in Eq. (12.21) yields

$$\begin{aligned} U_e = &\frac{1}{2}\int_V \sigma_{xx}\frac{\partial u}{\partial x}\, dV + \frac{1}{2}\int_V \sigma_{xy}\frac{\partial u}{\partial y}\, dV + \frac{1}{2}\int_V \sigma_{zx}\frac{\partial u}{\partial z}\, dV \\ &+ \frac{1}{2}\int_V \sigma_{xy}\frac{\partial v}{\partial x}\, dV + \frac{1}{2}\int_V \sigma_{yy}\frac{\partial v}{\partial y}\, dV + \frac{1}{2}\int_V \sigma_{yz}\frac{\partial v}{\partial z}\, dV \\ &+ \frac{1}{2}\int_V \sigma_{zx}\frac{\partial w}{\partial x}\, dV + \frac{1}{2}\int_V \sigma_{yz}\frac{\partial w}{\partial y}\, dV + \frac{1}{2}\int_V \sigma_{zz}\frac{\partial w}{\partial z}\, dV. \end{aligned} \tag{12.22}$$

Using integration by parts on the first term in Eq. (12.22)

$$\begin{aligned} \frac{1}{2}\int_V \sigma_{xx}\frac{\partial u}{\partial x}\, dV &= \frac{1}{2}\int_S \left(\int_x \sigma_{xx}\frac{\partial u}{\partial x}\, dx\right) dS \\ &= -\frac{1}{2}\int_V \frac{\partial \sigma_{xx}}{\partial x}\, u\, dV + \frac{1}{2}\int_S [\sigma_{xx}u]_{x=0}^{L}\, dS. \end{aligned}$$

Note that $\sigma_{xx}\Big|_{x=0}$ and $\sigma_{xx}\Big|_{x=L}$ are identically zero as the problem is that of a free-free structure, so

$$\frac{1}{2}\int_V \sigma_{xx}\frac{\partial u}{\partial x}\,dV = -\frac{1}{2}\int_V \frac{\partial \sigma_{xx}}{\partial x}\,u\,dv. \tag{12.23}$$

Similarly, by using integration by parts for the remaining terms, the strain energy is

$$\begin{aligned} U_e = &-\frac{1}{2}\int_V \left(\frac{\partial \sigma_{xx}}{\partial x}+\frac{\partial \sigma_{xy}}{\partial y}+\frac{\partial \sigma_{zx}}{\partial z}\right) u\,dV - \frac{1}{2}\int_V \left(\frac{\partial \sigma_{xy}}{\partial x}+\frac{\partial \sigma_{yy}}{\partial y}+\frac{\partial \sigma_{yz}}{\partial z}\right) v\,dV \\ &-\frac{1}{2}\int_V \left(\frac{\partial \sigma_{zx}}{\partial x}+\frac{\partial \sigma_{yz}}{\partial y}+\frac{\partial \sigma_{zz}}{\partial z}\right) w\,dV \end{aligned}$$

Consider the dynamic equilibrium equations for a structure in Cartesian coordinates,

$$\frac{\partial \sigma_{xx}}{\partial x}+\frac{\partial \sigma_{xy}}{\partial y}+\frac{\partial \sigma_{zx}}{\partial z} = \rho\frac{\partial^2 u}{\partial t^2}, \tag{12.24}$$

$$\frac{\partial \sigma_{xy}}{\partial x}+\frac{\partial \sigma_{yy}}{\partial y}+\frac{\partial \sigma_{yz}}{\partial z} = \rho\frac{\partial^2 v}{\partial t^2}, \tag{12.25}$$

$$\frac{\partial \sigma_{zx}}{\partial x}+\frac{\partial \sigma_{yz}}{\partial y}+\frac{\partial \sigma_{zz}}{\partial z} = \rho\frac{\partial^2 w}{\partial t^2}. \tag{12.26}$$

Substituting Eqs. (12.24) – (12.26) in the expression for strain energy yields

$$U_e = -\frac{1}{2}\int_V \left(\frac{\partial^2 u}{\partial t^2}u+\frac{\partial^2 v}{\partial t^2}v+\frac{\partial^2 w}{\partial t^2}w\right)\rho\,dV. \tag{12.27}$$

Writing Eq. (12.27) in vector notation previously defined produces

$$U_e = -\frac{1}{2}\int_V \left(\frac{\partial^2 \mathbf{d_E}}{\partial t^2}\,\Big|_{\mathrm{V}}\right)^T \left(\mathbf{d_E}\,\Big|_{\mathrm{V}}\right)\rho\,dV \tag{12.28}$$

Substituting Eq. (12.5) in Eq.(12.28) gives

$$U_e = -\frac{1}{2}\int_V \left(\frac{\partial^2 \boldsymbol{\eta}}{\partial t^2}\,\Big|_{\mathrm{V}}\right)^T \left(\Phi^T\Phi\right)\left(\boldsymbol{\eta}\,\Big|_{\mathrm{V}}\right)\rho\,dV \tag{12.29}$$

Note that $\boldsymbol{\eta}$ is a vector of harmonic functions in time with n natural frequencies, simplifying,

$$U_e = -\frac{1}{2}\left(\boldsymbol{\eta}\,\Big|_{\mathrm{V}}\right)^T \left[\Omega^2\int_V \left(\Phi^T\Phi\right)\rho\,dV\right]\left(\boldsymbol{\eta}\,\Big|_{\mathrm{V}}\right). \tag{12.30}$$

Using the definition of $I_{\Phi\Phi}$ from Eq. (12.18) produces finally

$$U_e(\mathbf{q}) = \frac{1}{2}\boldsymbol{\eta}^T\left[\Omega^2\mathbf{I}_{\Phi\Phi}\right]\boldsymbol{\eta}. \tag{12.31}$$

12.3 Virtual Work due to Internal Forces

The Lagrangian for the aircraft is defined as

$$\mathcal{L}(\dot{\mathbf{q}},\, \mathbf{q}) = T(\dot{\mathbf{q}},\, \mathbf{q}) - U_e(\mathbf{q}). \tag{12.32}$$

The action function for the motion is the integral of the Lagrangian from initial time t_i to to final time t_f,

$$\mathcal{S} = \int_{t_i}^{t_f} \mathcal{L}(\dot{\mathbf{q}},\, \mathbf{q})\, dt. \tag{12.33}$$

According to the Hamilton's principle of least action, any body following the laws of classical dynamics in order to go from an initial state to a final state will follow a path that will minimize the action function. Solve for the extremum by taking the first variation of the action function and equating it to zero,

$$\delta\mathcal{S} = \delta\left(\int_{t_i}^{t_f} \mathcal{L}(\dot{\mathbf{q}},\, \mathbf{q})\, dt\right) = 0. \tag{12.34}$$

As there are no nonholonomic constraints for the problem, the first variation can be taken inside the integral, resulting in

$$\int_{t_i}^{t_f} \delta\mathcal{L}(\dot{\mathbf{q}},\, \mathbf{q})\, dt = 0. \tag{12.35}$$

Using the chain rule yields

$$\int_{t_i}^{t_f} \left(\frac{\partial\mathcal{L}}{\partial\dot{\mathbf{q}}}(\dot{\mathbf{q}},\, \mathbf{q})\delta\dot{\mathbf{q}} + \frac{\partial\mathcal{L}}{\partial\mathbf{q}}(\dot{\mathbf{q}},\, \mathbf{q})\delta\mathbf{q}\right) dt = 0. \tag{12.36}$$

Using integration by parts yields

$$\left[\frac{\partial\mathcal{L}}{\partial\dot{\mathbf{q}}}(\dot{\mathbf{q}},\, \mathbf{q})\delta\mathbf{q}\right]_{t_i}^{t_f} - \int_{t_i}^{t_f} \left(\frac{d}{dt}\left(\frac{\partial\mathcal{L}}{\partial\dot{\mathbf{q}}}(\dot{\mathbf{q}},\, \mathbf{q})\right) - \frac{\partial\mathcal{L}}{\partial\mathbf{q}}(\dot{\mathbf{q}},\, \mathbf{q})\right)\delta\mathbf{q}\, dt = 0. \tag{12.37}$$

Given the initial and final configurations of the system, by assumption from Hamilton's principle of least action, $\delta\mathbf{q}\Big|_{t_i}$ and $\delta\mathbf{q}\Big|_{t_i}$ are zero. Equation (12.37) will yield

$$\frac{d}{dt}\left(\frac{\partial\mathcal{L}}{\partial\dot{\mathbf{q}}}(\dot{\mathbf{q}},\, \mathbf{q})\right) - \frac{\partial\mathcal{L}}{\partial\mathbf{q}}(\dot{\mathbf{q}},\, \mathbf{q}) = 0 \tag{12.38}$$

for internal mechanism. Substituting the kinetic and strain energy expressions in Eq. (12.38) yields

$$\text{LHS} := \begin{pmatrix} m\,\mathbb{I}_{3\times3} & I_p + I_d & I_\Phi \\ I_p^T + I_d^T & I_{pp} + I_{dd} + I_{pd} + I_{pd}^T & I_{p\Phi} + I_{d\Phi} \\ I_\Phi^T & I_{p\Phi}^T + I_{d\Phi}^T & I_{\Phi\Phi} \end{pmatrix} \ddot{\mathbf{q}} + \begin{pmatrix} \mathbf{0}_{3\times3} & \dot{I}_d & \mathbf{0}_{3\times n} \\ \dot{I}_d^T & \dot{I}_{dd} + \dot{I}_{pd} + \dot{I}_{pd}^T & \dot{I}_{d\Phi} \\ \mathbf{0}_{n\times3} & \dot{I}_{d\Phi}^T & \mathbf{0}_{n\times n} \end{pmatrix} \dot{\mathbf{q}} - \frac{1}{2} \begin{Bmatrix} \dot{\mathbf{q}}^T \left(\frac{\partial \mathcal{M}}{\partial q_1}\right) \dot{\mathbf{q}} \\ \dot{\mathbf{q}}^T \left(\frac{\partial \mathcal{M}}{\partial q_2}\right) \dot{\mathbf{q}} \\ \vdots \\ \dot{\mathbf{q}}^T \left(\frac{\partial \mathcal{M}}{\partial q_{n+6}}\right) \dot{\mathbf{q}} \end{Bmatrix} - \begin{Bmatrix} \mathbf{0}_{3\times1} \\ \mathbf{0}_{3\times1} \\ I_{\Phi\Phi}\boldsymbol{\eta} \end{Bmatrix} \tag{12.39}$$

Chapter 13

Virtual Work - External Forces

The principle of virtual work is used to derive the equations of motion for the flexible air-breathing hypersonic vehicle by equating the virtual work due to the external forces and internal forces. Virtual work due to external forces is used in this chapter to derive expressions for the generalized forces. The three external forces experienced by the aircraft are gravitational, aerodynamic, and control forces.

13.1 Gravitational Forces

The gravitational force is a conservative force field, it can be expressed in terms of a potential function

$$U_g(\mathbf{q}) = -m\mathbf{g}^T\mathbf{p}_v - \mathbf{g}^T\mathbf{C}_{RB} - \mathbf{g}^T[\mathbf{I}_\Phi]\boldsymbol{\eta}, \tag{13.1}$$

where $\mathbf{C}_{RB}$ is the first moment of inertia of the undeformed aircraft, and $\mathbf{g}$ is the gravity vector, which is a function of the orientation of the aircraft. The generalized force vector in terms of the gravitational potential is given by

$$\mathbf{Q}_g = -\frac{\partial U_g}{\partial \mathbf{q}}. \tag{13.2}$$

The expression for the generalized gravitational force in vector form is

$$\mathbf{Q}_g = \begin{Bmatrix} m\mathbf{g} \\ \left(\frac{\partial \mathbf{g}}{\partial \boldsymbol{\Theta}_{V,I}}\right)^T (\mathbf{p}_v + \mathbf{C}_{RB} + \mathbf{I}_\Phi\boldsymbol{\eta}) \\ \mathbf{I}_\Phi^T\mathbf{g} \end{Bmatrix}. \tag{13.3}$$

13.2 Aerodynamic Forces

Chapter 10 presents the derivations for aerodynamic pressures of various panels throughout the length of the body. It is important to note that the aircraft geometry is divided in to three segments along its length; forebody, nacelle, and aftbody. The aerodynamic pressure distribution over a given cross section vary based on the section. Hence, the equivalent forces and moment expressions are obtained for these three section separately.

13.2.1 Forebody

The forces and moments per unit length over a cross section located at a distance x_1 from the tip of the aircraft along the longitudinal axis are

$$
\begin{aligned}
N_1 &= p_u(M_\infty) l_u(x_1) \sin(\tau_{1,u} + p_l(M_\infty) l_l(x_1) \sin(\tau_{1,l}),\\
N_2 &= 0,\\
N_3 &= p_l(M_\infty) l_l(x_1) \cos(\tau_{1,l}) + 2p_{sl}(M_\infty) l_{sl}(x_1) \cos(\xi_1) - p_u(M_\infty) l_u(x_1) \cos(\tau_{1,u}),\\
M_1 &= 0,\\
M_2 &= p_l(M_\infty) l_l(x_1) l_{sl}(x_1) \sin(\tau_{1,l}) - p_u(M_\infty) l_u(x_1) l_{su}(x_1) \sin(\tau_{1,u}),\\
M_3 &= 0,\\
V_2 &= p_l(M_\infty) l_l(x_1) \sin(\tau_{1,l}) - p_u(M_\infty) l_u(x_1) \sin(\tau_{1,u}),\\
V_3 &= 0,
\end{aligned}
$$

where N_1, N_2, N_3 are axial force densities along x_1, x_2, x_3 respectively, M_1, M_2, M_3 are moment densities about x_1, x_2, x_3 respectively, and V_2, V_3 are out of plane shear forces per unit length.

13.2.2 Nacelle

The forces and moments per unit length over a cross section located at a distance x_1 from the tip of the aircraft along the longitudinal axis are

$$
\begin{aligned}
N_1 &= p_u(M_\infty) l_u(x_1) \sin(\tau_{1,u},\\
N_2 &= 0,\\
N_3 &= p_l(M_\infty) l_l(x_1) + 2p_{sl}(M_\infty) l_{sl}(x_1) \cos(\xi_1) - p_u(M_\infty) l_u(x_1) \cos(\tau_{1,u}),\\
M_1 &= 0,\\
M_2 &= -p_u(M_\infty) l_u(x_1) l_{su}(x_1) \sin(\tau_{1,u}),\\
M_3 &= 0,\\
V_2 &= -p_u(M_\infty) l_u(x_1) \sin(\tau_{1,u}),\\
V_3 &= 0,
\end{aligned}
$$

where N_1, N_2, N_3 are axial force densities along x_1, x_2, x_3 respectively, M_1, M_2, M_3 are moment densities about x_1, x_2, x_3 respectively, and V_2, V_3 are out of plane shear forces per unit length.

13.2.3 Aftbody

The forces and moments per unit length over a cross section located at a distance x_1 from the tip of the aircraft along the longitudinal axis are

$$
\begin{aligned}
N_1 &= p_u(M_\infty) l_u(x_1) \sin(\tau_{1,u} + p_l(M_\infty) l_l(x_1) \sin(\tau_2 + \tau_{1,u}),\\
N_2 &= 0,\\
N_3 &= p_l(M_\infty) l_l(x_1) \cos(\tau_2 + \tau_{1,u}) + 2 p_{sl}(M_\infty) l_{sl}(x_1) \cos(\xi_1) - p_u(M_\infty) l_u(x_1) \cos(\tau_{1,u}),\\
M_1 &= 0,\\
M_2 &= p_l(M_\infty) l_l(x_1) l_{sl}(x_1) \sin(\tau_2 + \tau_{1,u}) - p_u(M_\infty) l_u(x_1) l_{su}(x_1) \sin(\tau_{1,u}),\\
M_3 &= 0,\\
V_2 &= p_l(M_\infty) l_l(x_1) \sin(\tau_2 + \tau_{1,u}) - p_u(M_\infty) l_u(x_1) \sin(\tau_{1,u}),\\
V_3 &= 0,
\end{aligned}
$$

where N_1, N_2, N_3 are axial force densities along x_1, x_2, x_3 respectively, M_1, M_2, M_3 are moment densities about x_1, x_2, x_3 respectively, and V_2, V_3 are out of plane shear forces per unit length.

The expressions for force and moment per unit length must be used to compute virtual work due to generalized force and moment densities expressed in terms of the body frame, in order to obtain the generalized forces with respect to the inertial frame. The expression for virtual work due to the aerodynamic generalized force and moment densities is

$$
\begin{aligned}
\delta W_a = &\left(R \int_{x_1} \left\{ \begin{array}{c} N_1 \\ N_2 \\ N_3 \end{array} \right\} dx_1 \right)^T \delta \mathbf{p}_v + \left(R \int_{x_1} \left\{ \begin{array}{c} M_1 \\ M_2 \\ M_3 \end{array} \right\} dx_1 \right)^T \delta \boldsymbol{\theta}_{V,I} \\
&+ \int_{x_1} \left(M_1 \, \delta\beta_1 + (V_2 \, lsl(x_1) + M_2) \delta\beta_2 + \left(V_3 \left(\frac{l_u(x_1)}{2} \right) - M_3 \right) \delta\beta_3 \right) dx_1 \\
&+ \int_{x_1} \left(N_1 \delta\bar{u}_1 + N_2 \delta\bar{u}_2 + N_3 \delta\bar{u}_3 \right) dx_1. \qquad (13.4)
\end{aligned}
$$

By writing Eq. (13.4) in vector form, we can compute the generalized force vector for the aerodynamic forces

$$\mathbf{Q}_a = \left\{ \begin{array}{c} \int_{x_1} \left\{ \begin{array}{c} N_1 \\ N_2 \\ N_3 \end{array} \right\} R\, dx_1 \\ \int_{x_1} \left\{ \begin{array}{c} M_1 \\ M_2 \\ M_3 \end{array} \right\} R\, dx_1 \\ \int_{x_1} \left(M_1 \left\{ \phi_{\beta_1} \right\} + \left(V_2\, lsl(x_1) + M_2 \right) \left\{ \phi_{\beta_2} \right\} + \left(V_3 \left(\frac{l_u(x_1)}{2} \right) - M_3 \right) \left\{ \phi_{\beta_2} \right\} \right) dx_1 \\ + \int_{x_1} \left(N_1 \left\{ \phi_{\bar{u}_1} \right\} + N_2 \left\{ \phi_{\bar{u}_2} \right\} + N_3 \left\{ \phi_{\bar{u}_3} \right\} \right) dx_1 \end{array} \right\} \tag{13.5}$$

13.3 Control Forces

Aerothermoelastic effects, aeropropulsive effects, and nonminimum phase behavior make control system design for an air-breathing hypersonic vehicle a challenging task. The complex interaction between aerothermal loads and the airframe achieve a reduction in frequencies of flexible modes, thus moving them closer to the rigid body modes and increase the coupling between them. The aeropropulsive effects, on the other hand, induce low frequency oscillations in the aircraft's dynamics. As the propulsion system is located in the underbelly of the aircraft, there is a large moment arm for the thrust resulting in a significant nose-up moment. The presence of an unstable zero in the transfer function of the flight path angle, results in nonminimum phase behavior. Control designers have only five control inputs at their disposal to compensate for all effects , which include and are restricted to fuel equivalence ratio(thrust), two elevon deflections and two rudder deflections.The expression for the generalized control force vector is

$$\mathbf{Q}_c = \left\{ \begin{array}{c} \mathbf{T}_{3\times 1} \\ \mathbf{M}_{\mathbf{T}3\times 1} \\ \mathbf{0}_{n\times 1} \end{array} \right\} + \left\{ \begin{array}{c} \mathbf{F}_{\mathbf{cs}3\times 1} \\ \mathbf{M}_{\mathbf{cs}3\times 1} \\ \mathbf{0}_{n\times 1} \end{array} \right\} \tag{13.6}$$

where, the control saurface force vector in the body frame is

$$\begin{aligned}
(\mathbf{F_{cs_1}})_{\text{body}} &= (p_{cs_1,l} - p_{cs_1,u})\, S_{cs_1} \sin(\delta_{cs_1} + \theta_{\text{def}_1}) \\
&\quad + (p_{cs_2,l} - p_{cs_2,u})\, S_{cs_2} \sin(\delta_{cs_2} + \theta_{\text{def}_2}) \\
&\quad + (p_{cs_3,o} - p_{cs_3,i})\, S_{cs_3} \cos(\delta_{cs_3} + \gamma_{\text{def}_3}) \\
&\quad - (p_{cs_4,o} - p_{cs_4,i})\, S_{cs_4} \cos(\delta_{cs_4} + \gamma_{\text{def}_4}), \qquad (13.7) \\
(\mathbf{F_{cs_2}})_{\text{body}} &= (p_{cs_3,o} - p_{cs_3,i})\, S_{cs_3} \sin(\delta_{cs_3} + \gamma_{\text{def}_3}) \\
&\quad - (p_{cs_4,o} - p_{cs_4,i})\, S_{cs_4} \sin(\delta_{cs_4} + \gamma_{\text{def}_4}), \qquad (13.8) \\
(\mathbf{F_{cs_3}})_{\text{body}} &= (p_{cs_1,l} - p_{cs_1,u})\, S_{cs_1} \cos(\delta_{cs_1} + \theta_{\text{def}_1}) \\
&\quad + (p_{cs_2,l} - p_{cs_2,u})\, S_{cs_2} \cos(\delta_{cs_2} + \theta_{\text{def}_2}), \qquad (13.9)
\end{aligned}$$

and the control surface moment vector in the body frame is

$$\begin{aligned}
(\mathbf{M_{cs_1}})_{\text{body}} &= (p_{cs_1,l} - p_{cs_1,u})\, S_{cs_1} y_{cs_1} \cos(\delta_{cs_1} + \theta_{\text{def}_1}) \\
&\quad - (p_{cs_2,l} - p_{cs_2,u})\, S_{cs_2} y_{cs_2} \cos(\delta_{cs_2} + \theta_{\text{def}_2}), \qquad (13.10) \\
(\mathbf{M_{cs_2}})_{\text{body}} &= (p_{cs_1,l} - p_{cs_1,u})\, S_{cs_1} (\mathrm{x}_{cs_1} \cos(\delta_{cs_1} + \theta_{\text{def}_1}) - \mathrm{z}_{cs_1} \sin(\delta_{cs_1} + \theta_{\text{def}_1})) \\
&\quad + (p_{cs_3,o} - p_{cs_3,i})\, S_{cs_3} z_{cs_3} \cos(\delta_{cs_3} + \gamma_{\text{def}_3}) \\
&\quad + (p_{cs_2,l} - p_{cs_2,u})\, S_{cs_2} (\mathrm{x}_{cs_2} \cos(\delta_{cs_2} + \theta_{\text{def}_2}) - \mathrm{z}_{cs_2} \sin(\delta_{cs_2} + \theta_{\text{def}_2})) \\
&\quad - (p_{cs_4,o} - p_{cs_4,i})\, S_{cs_4} z_{cs_4} \cos(\delta_{cs_4} + \gamma_{\text{def}_4}), \qquad (13.11)
\end{aligned}$$

$$\begin{aligned}
(\mathbf{M_{cs_3}})_{\text{body}} &= (p_{cs_4,o} - p_{cs_4,i})\, S_{cs_4} y_{cs_4} \sin(\delta_{cs_4} + \gamma_{\text{def}_4}) \\
&\quad - (p_{cs_3,o} - p_{cs_3,i})\, S_{cs_3} y_{cs_3} \sin(\delta_{cs_3} + \gamma_{\text{def}_3}). \qquad (13.12)
\end{aligned}$$

Putting Eqs. (13.3), (13.5), and (13.6), we have the expression for the generalized force vector

$$\text{RHS} := \mathbf{Q}_g + \mathbf{Q}_a + \mathbf{Q}_c. \qquad (13.13)$$

The second order nonlinear equations of motion for a flexible aircraft are of the form

$$\mathcal{M}(\mathbf{q})\ddot{\mathbf{q}} + \mathbf{C}(\mathbf{q}, \dot{\mathbf{q}}) - \mathbf{Q}_a(\mathbf{q}, \dot{\mathbf{q}}, \alpha) + \mathbf{P}(\mathbf{q}) = \mathbf{Q}_c(\mathbf{q}, \dot{\mathbf{q}}, \alpha, \mathbf{u}), \qquad (13.14)$$

where $\mathbf{u}$ is the vector of control inputs, α is the angle of attack, $\mathbf{C}(\mathbf{q}, \dot{\mathbf{q}})$ represents the Coriolis forces, $\mathbf{P}(\mathbf{q})$ represents forces due to the conservative force fields, gravitational potential energy and elastic strain energy. The effect of the airframe tightly integrated with the propulsion system described earlier is modeled here through the angle of attack α, which depends on the structural deflection at the forebody tip of the aircraft, and to which the thrust is sensitive. Therefore, this model captures the effect of a flexible airframe on the thrust and through that the effect on the overall dynamics of the aircraft. It is important

to note that α is a function of $\boldsymbol{\eta}$, and hence depends on $\mathbf{q}$. The expression for the angle of attack is given by

$$\alpha(t) = \alpha_0 + \left\{ \frac{\partial \phi_{\bar{u}_3}}{\partial x_1} \Big|_{x_1=0}^{T} \right\} \boldsymbol{\eta}(t). \tag{13.15}$$

The nonlinear equations of motion determine the evolution of the shape of the aircraft over time through the modal coordinate vector $\boldsymbol{\eta}(t)$. Equation (13.15) presents the relation between the modal coordinate vector and instantaneous angle of attack that is used to compute the aerodynamics forces, which in turn impact the evolution of the modal coordinate vector through the nonlinear equations of motion. Thus, initiating a constant exchange of energy between the structure and the associated flow field.

Phase IV:

Stability Analysis

Chapter 14

Equilibrium Conditions

A typical air-breathing hypersonic vehicle's mission profile is predominantly cruise. Hence, it would be appropriate to use cruise as the desired trajectory and design an appropriate closed-loop control system to ensure that the aircraft tracks this chosen desired trajectory. At cruise, the aircraft does not accelerate and hence, attains dynamic equilibrium which is characterized by zero net acceleration. The aircraft would be required to be trimmed at this desired cruise condition (no rotation) and it is assumed that the aircraft has structurally reached a steady state, vibrations are damped out. These conditions are expressed mathematically as

$$\begin{aligned} \ddot{\mathbf{q}}_{eq} &= \mathbf{0}, \\ \dot{\boldsymbol{\theta}}_{V,I_{eq}} &= \mathbf{0}, \\ \dot{\boldsymbol{\eta}}_{eq} &= \mathbf{0}. \end{aligned}$$

The above conditions are substituted into the nonlinear equations of motion, to obtain a set of $n+6$ noninear algebraic equations

$$\mathcal{M}(\mathbf{q})\ddot{\mathbf{q}} + \cancel{\mathbf{C}(\mathbf{q}, \dot{\mathbf{q}})} + \mathbf{P}(\mathbf{q}) = -\mathbf{Q}_{aero}(\mathbf{q}, \dot{\mathbf{q}}) + \mathbf{Q}_{cs}(\mathbf{q}, \dot{\mathbf{q}}, \mathbf{u}_{cs}, \text{FER}) \tag{14.1}$$

in $n+14$ variables — three components of $\mathbf{p}_{v_{eq}}$, three components of $\dot{\mathbf{p}}_{v_{eq}}$, three Euler angles $\boldsymbol{\theta}_{V,I}$, fuel equivalence ratio ϕ, two rudder and two elevon deflections $\mathbf{u}_{cs}$, and n modal coordinates.

In order to find a unique solution for the equilibrium condition, some of the variables were conveniently chosen as shown in Fig. 14.1. The sequence of rotation for the Euler angles is chosen to be $3-2-1$ and the three angles were chosen to be zero. The three component position vector is replaced with altitude h and the velocity vector is replaced with cruise speed v_∞. Thus, reducing the total number of variables to $n+7$. From a design stand point it would be desirable to choose cruise velocity and altitude, so that the appropriate equilibrium conditions can be computed. Due to the simplifying assumptions at equilibrium the n equations for the modal coordinates are decoupled from the 6 rigid body

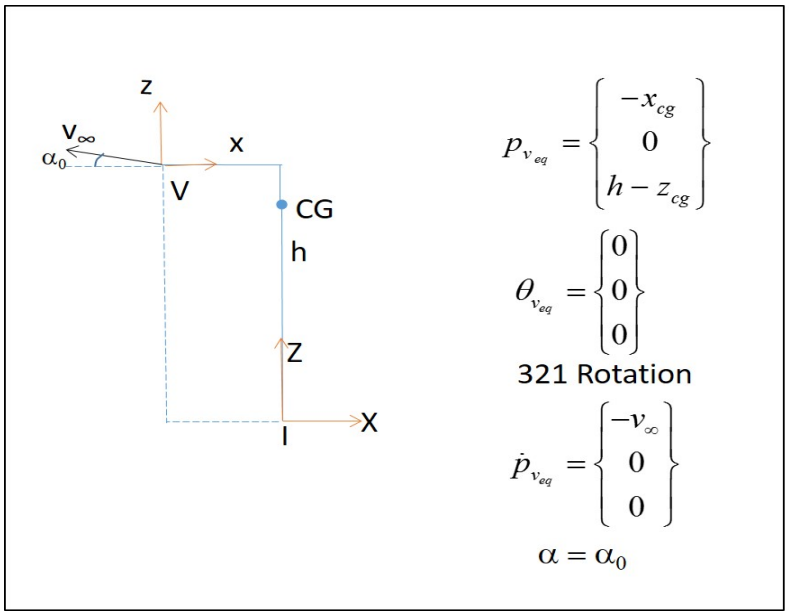

Figure 14.1: Simplifying assumptions at Equilibrium.

modes resulting in the following expression

$$\boldsymbol{\eta}_{eq} = \left[I_{\Phi\Phi}\Omega^2\right]^{-1} \left\{\mathbf{Q}_{aero_{7-n}}(h,\, v_\infty,\, \text{FER})\right\}. \tag{14.2}$$

This leaves the following 6 equations

$$\begin{Bmatrix} 0 \\ 0 \\ W \\ P_4(h,\, v_\infty,\, \boldsymbol{\eta}_{eq}) \\ P_5(h,\, v_\infty,\, \boldsymbol{\eta}_{eq}) \\ P_6(h,\, v_\infty,\, \boldsymbol{\eta}_{eq}) \end{Bmatrix} = \begin{Bmatrix} D(h,\, v_\infty,\, \text{FER}) \\ 0 \\ L(h,\, v_\infty,\, \text{FER}) \\ Q_{aero_4}(h,\, v_\infty,\, \text{FER}) \\ Q_{aero_5}(h,\, v_\infty,\, \text{FER}) \\ Q_{aero_6}(h,\, v_\infty,\, \text{FER}) \end{Bmatrix} + \begin{Bmatrix} -T(h,\, v_\infty,\, \text{FER}) \\ 0 \\ 0 \\ 0 \\ M_T(h,\, v_\infty,\, \text{FER}) \\ 0 \end{Bmatrix} + \begin{Bmatrix} Q_{cs_1}(h,\, v_\infty,\, \boldsymbol{\eta}_{eq},\, \mathbf{u}_{cs}) \\ Q_{cs_2}(h,\, v_\infty,\, \boldsymbol{\eta}_{eq},\, \mathbf{u}_{cs}) \\ Q_{cs_3}(h,\, v_\infty,\, \boldsymbol{\eta}_{eq},\, \mathbf{u}_{cs}) \\ Q_{cs_4}(h,\, v_\infty,\, \boldsymbol{\eta}_{eq},\, \mathbf{u}_{cs}) \\ Q_{cs_5}(h,\, v_\infty,\, \boldsymbol{\eta}_{eq},\, \mathbf{u}_{cs}) \\ Q_{cs_6}(h,\, v_\infty,\, \boldsymbol{\eta}_{eq},\, \mathbf{u}_{cs}) \end{Bmatrix}. \tag{14.3}$$

The second, fourth, and sixth equations are associated with side slip, roll, and yaw. These three equations are identically equal to zero, due to the symmertry about the vertical axis.

Figure 14.2: An exaggerated side view of the air-breathing hypersonic vehicle at equilibrium compared to the undeformed aircraft.

This reduces the problem to three coupled nonlinear algebraic equations

$$
\begin{aligned}
&D(h,\, v_\infty,\, \text{FER},\, \alpha_0) - T(h,\, v_\infty,\, \text{FER},\, \alpha_0) + Q_{cs_1}(h,\, v_\infty,\, \boldsymbol{\eta}_{eq},\, \mathbf{u}_{cs},\, \alpha_0) = 0,\\
&-W + L(h,\, v_\infty,\, \text{FER},\, \alpha_0) + Q_{cs_3}(h,\, v_\infty,\, \boldsymbol{\eta}_{eq},\, \mathbf{u}_{cs},\, \alpha_0) = 0,\\
&-P_5(h,\, v_\infty,\, \boldsymbol{\eta}_{eq}) + Q_{aero_5}(h,\, v_\infty,\, \text{FER},\, \alpha_0) + M_T(h,\, v_\infty,\, \text{FER},\, \alpha_0) + Q_{cs_5}(h,\, v_\infty,\, \boldsymbol{\eta}_{eq},\, \mathbf{u}_{cs},\, \alpha_0) = 0.
\end{aligned}
$$

in four variables; α, FER, $\mathbf{u}_{cs_1}$, and $\mathbf{u}_{cs_2}$. Since the roll equation is identically equal to zero at equilibrium, we need to ensure that $\mathbf{u}_{cs_1}$, and $\mathbf{u}_{cs_2}$ are equal. This yields three equations in three variables.

For a desired cruise altitude of 110, 000 ft and cruise Mach numer of 10, we have the following equilibrium conditions:

$$
\begin{aligned}
&h_{eq} = 110,\, 000\,\text{ft}, \qquad \alpha_{eq} = -0.4308^0, \qquad M_{\infty_{eq}} = 10, \qquad \text{FER}_{eq} = 0.94,\\
&\mathbf{u}_{cs_{1_{eq}}} = \mathbf{u}_{cs_{1_{eq}}} = -4.5916^0, \qquad \mathbf{u}_{cs_{3_{eq}}} = \mathbf{u}_{cs_{4_{eq}}} = 2^0,
\end{aligned}
$$

Due to symmetry, sideslip and yaw moments cancel eachother out. Nonzero values for rudder deflections are chosen to avoid null column vectors in the control coefficent matrix B. This is a consequence of linearization and doesn't arise if analysis was carried out on the nonlinear system.

An exaggerated side view of the deformed aircraft at equilibrium is presented in Fig. 14.2 and compared to the shape of the undeformed aircraft in the background. Notice the change in angle of attack at the front and the displacement of elevons at the back due to deformation.

Chapter 15

Linearized Equations of Motion

The primary performance expectation from a typical air-breathing hypersonic vehicle is to travel between two farthest land targets in about two hours, by consuming less than 50% of liquid hydrogen (LH_2) fuel available at take-off. Such extreme expectations are typical of high-speed, high-altitude, long range aircrafts. This narrows down the mission profile to cruising at a very high altitude and a high Mach number, like the ones obtained in the previous chapter. At $110,000$ ft, due to highly rarefied atmosphere, the threat of high speed winds and gusts perturbing the aircraft from it's equilibrium state is significantly lowered. The typical wind speeds above $100,000$ ft are about $50-60$ knots, as found experimentally in Ref. [51]. The effect of gusts of magnitude $30-60$ m/s on the dynamics of an aircraft weighing $107,000$ kg, travelling at speeds as large as 3000 m/s can be studied by linearizing the nonlinear equations of motion derived in Phase 3 about the equilibrium conditions obtained in the previous chapter.

We start with the nonlinear equations of motion derived earlier, which are of the form

$$\mathcal{M}(q(t))\ddot{q}(t) + \mathcal{C}\left(q(t),\, \dot{q}(t)\right) + \mathcal{P}\left(q(t)\right) = \mathcal{Q}_a\left(q(t),\, \dot{q}(t)\right) + \mathcal{Q}_c\left(q(t), \dot{q}(t),\, u(t)\right), \tag{15.1}$$

where $\mathcal{M}(q(t))$ is the matrix that represents the translational, rotational, and vibrational inertia of the aircraft, $\mathcal{C}(q(t),\, \dot{q}(t))$ is a vector that represents coriolis forces and gyroscopic moments, $\mathcal{P}(q(t))$ represents gravitational and elastic forces, $\mathcal{Q}_a(q(t),\, \dot{q}(t))$ represents the aerodynamic forces, and $\mathcal{Q}_c(q(t),\, \dot{q}(t),\, u(t))$ represents the control forces. Equations (15.1) are linearized about an equilibrium $(\bar{q},\, \dot{\bar{q}})$ using small perturbation theory, where the state variables are expanded using a Taylor series approximation. By neglecting second order and higher order terms, we obtain a system of linear equations that represent the dynamics of the system of nonlinear Eqs. (15.1) accurately enough, provided the perturbations are small. This paradigm fits aptly for the case of a flexible air-breathing hypersonic vehicle cruising at very high altitudes, as mentioned earlier, due to the rarefied atmosphere encountered at such high altitudes the perturbation forces, which are usually in the form of gusts, are small compared to the inertia of the aircraft. Having said that, it is important to study the dynamics of the aircraft under the influence of such small perturbations and design feedback

control laws capable of ensuring that the vehicle stays on course. The linearized equations of motion about an equilibrium state are given by

$$M_e \, \ddot{\delta q}(t) + C_e \, \dot{\delta q}(t) + K_e \delta q(t) = B_e \delta u(t) \tag{15.2}$$

where

$$\begin{aligned} M_e =& \mathcal{M}(\bar{q}), && (15.3)\\ C_e =& \nabla_{\dot{q}} \mathcal{C}\left(\bar{q}, \, \dot{\bar{q}}\right) - \nabla_{\dot{q}} \mathcal{Q}_a \left(\bar{q}, \, \dot{\bar{q}}\right) - \nabla_{\dot{q}} \mathcal{Q}_c \left(\bar{q}, \, \dot{\bar{q}}, \, \bar{u}\right), && (15.4)\\ K_e =& \nabla_q \mathcal{P}\left(\bar{q}\right) + \nabla_q \mathcal{C}\left(\bar{q}, \, \dot{\bar{q}}\right) - \nabla_q \mathcal{Q}_a \left(\bar{q}, \, \dot{\bar{q}}\right) - \nabla_q \mathcal{Q}_c \left(\bar{q}, \, \dot{\bar{q}}, \, \bar{u}\right), && (15.5)\\ B_e =& \nabla_u \mathcal{Q}_c \left(\bar{q}, \, \dot{\bar{q}}, \, \bar{u}\right). && (15.6) \end{aligned}$$

Note that only M_e is a symmetric, positive definite matrix, while C_e, K_e, B_e are asymmetric matrices. The matrix $\nabla_{\dot{q}} \mathcal{C}(\bar{q}, \, \dot{\bar{q}})$ is strictly skew-symmetric as it consists of coriolis forces and gyroscopic moments, while the matrices $\nabla_{\dot{q}} \mathcal{Q}_a(\bar{q}, \, \dot{\bar{q}})$ and $\nabla_{\dot{q}} \mathcal{Q}_c(\bar{q}, \, \dot{\bar{q}}, \, \bar{u})$ depend on the aerodynamic and control force vectors, respectively. The Jacobian matrix of the aerodynamic force vector with respect to $\dot{q}$ doesn't (necessarily) turn out to be a symmetric matrix and the control force vector is populated by point forces that effect the evolution of only the first six states. As a consequence of such a functional dependence, the resulting linearized "damping" matrix C_e is asymmetric. The matrix $\nabla_q \mathcal{P}(\bar{q})$ is symmetric, but the matrices $\nabla_q \mathcal{C}(\bar{q}, \, \dot{\bar{q}})$, $\nabla_q \mathcal{Q}_a(\bar{q}, \, \dot{\bar{q}})$, and $\nabla_q \mathcal{Q}_c(\bar{q}, \, \dot{\bar{q}}, \, \bar{u})$ are asymmetric for the reasons stated above resulting in an asymmetric linearized "stiffness" matrix K_e. For most mechanical sytems, the second order equations of motion exhibit rich mathematical structure, via M_e, K_e, and seldom through C_e matrices. With only M_e being symmetric, the benefits of working with a second order dynamical system are outnumbered by the advantages of transforming the system into it's first order counterpart, which has historically been a preferred choice for mathematicians since the very first control theoretic principles were conceptualized. This choice was motivated by the transformability of higher order sytems into first order ones.

A typical first-order dynamical system is given by

$$\dot{x}(t) = Ax(t) + Bu(t). \tag{15.7}$$

Equations. (15.2) when transformed into a first order system, assume the form described by Eq. (15.7), where

$$A = \begin{pmatrix} 0_{n\times n} & I_{n\times n} \\ -\left(Me^{-1}K_e\right)_{n\times n} & -(M_e^{-1}C_e)_{n\times n} \end{pmatrix}, \quad B = \begin{pmatrix} 0_{n\times m} \\ (B_e)_{n\times m} \end{pmatrix}, \quad x(t) = \begin{Bmatrix} \delta q(t) \\ \delta \dot{q}(t) \end{Bmatrix}.$$

For the analysis presented in subsequent chapters, the perturbed air-breathing hypersonic vehicle dynamics are represented by a linearized system consisting of 12 rigid body modes, with six displacements and six velocities describing motion in a six degree of freedom space, and 28 flexible modes, where 14 of them represent vibrational dispacement, while the other 14 represent vibrational velocities.

Chapter 16

Open-loop Stability Analysis

Equation (15.2) governs the behavior of the system under the influence of perturbed initial conditions that are small in magnitude. The linearized system is modeled by taking into account longitudinal, lateral, and directional dynamics coupled with transverse and lateral bending, transverse and lateral shear, and torsion. Theoretically, such a system would be infinite dimensional. However, by neglecting higher order flexible modes, which get damped out rapidly during motion, we have a system that has a dimension 40. Further, five control inputs are used to compensate for deviations from the equilibrium during cruise, given by the normalized fuel equivalence ratio, two elevon deflections, and two rudder deflections. Figure 16.1 presents a plot of the 40 eigenvalues in the complex plane, showing a few highly unstable modes in the right half plane. The dependence of these modes on the state variables will be studied by carrying out selective modal analysis.

Early efforts in estimating relative participation of a given mode on a particular state in linear time-invariant systems (LTI) date back to the early 1980s, where van Ness et al.[42] and Verghese et al.[55] carried out modal analysis to estimate the extent of impact unstable modes have on state variables of systems that model the dynamics of large scale complex power system networks. On one hand, the method implemented by van Ness et al.[42] utilizes the relative magnitudes of an eigenvector associated with a certain mode to estimate the relative impact on state variables if that particular mode was excited. This approach only quantifies the impact a given mode would have on the relative response of a certain state variable. When dealing with large scale coupled systems, it is important to study the relative distribution of modal energies among state variables as the dynamics of such systems are driven by constant exhange of energy between modes. The method implemented by Verghese et al.[55] extend the works of MacFarlane[32] to carry out selective modal analysis of large scale, coupled, and linear time invariant systems.

Table 16.1 presents a comparison between the first 12 free vibration frequencies and forced vibration frequencies. Upon careful inspection, we can safely conclude that these

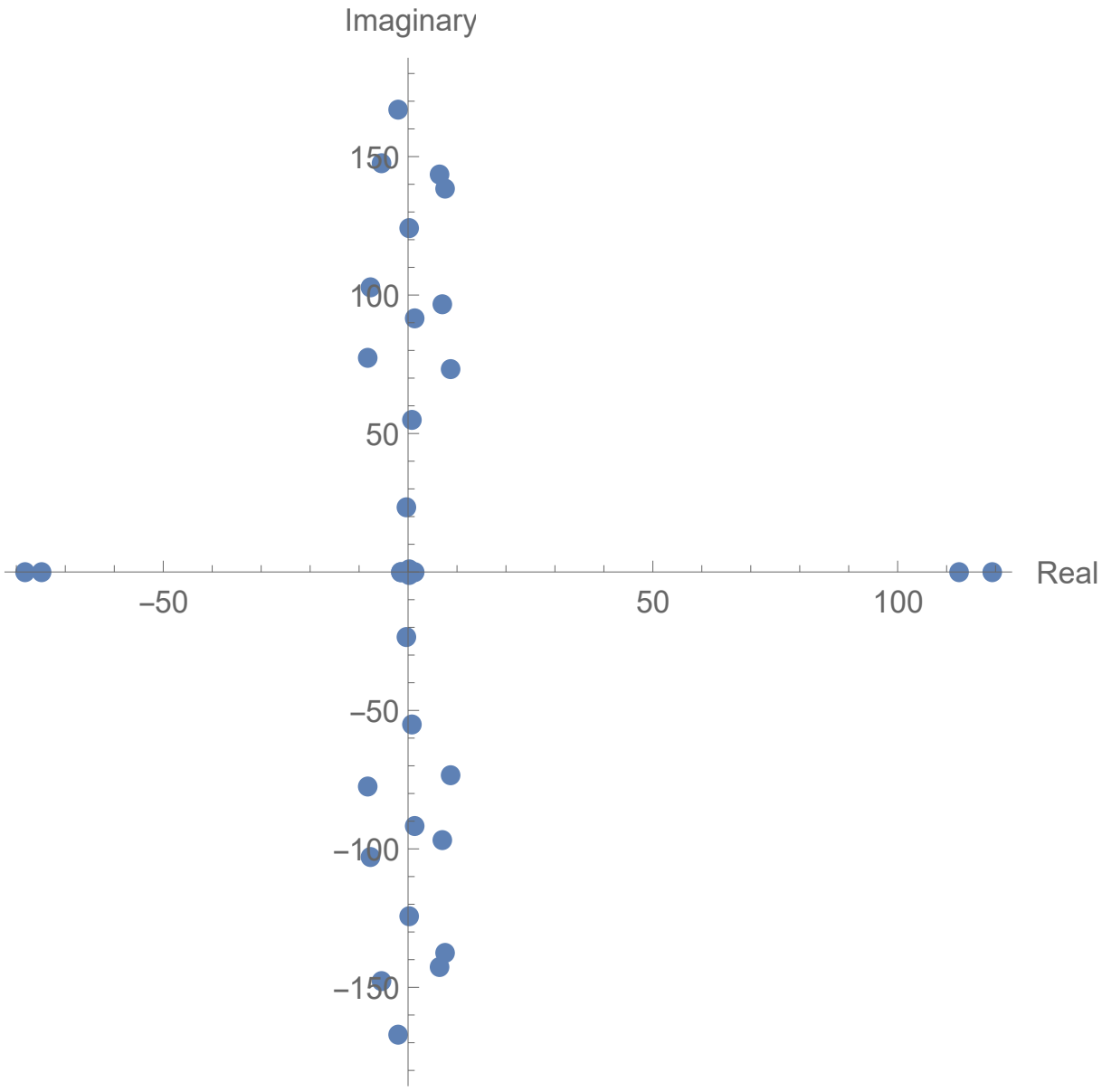

Figure 16.1: Openloop eigenvalues in complex plane.

Table 16.1: "Predominantly" rigid body frequencies.

Free vibration frequency (rad/s)	Open-loop frequency (rad/s)
0	**0.0040192**
0	-0.00401959
0	$\mathbf{1.25147 \times 10^{-7} + j0.0094443}$
0	$\mathbf{1.25147 \times 10^{-7} - j0.0094443}$
0	$-0.201524 + j0.395691$
0	$-0.201524 - j0.395691$
0	$\mathbf{0.382498 + j0.617026}$
0	$\mathbf{0.382498 - j0.617026}$
0	**0.860806**
0	**1.47968**
0	$-1.59771 + j0.158458$
0	$-1.59771 + j0.158458$

modes "predominantly" represent rigid body dynamics governed by state variables

$$\left\{p_{v_1},\, p_{v_2},\, p_{v_3},\, \theta_{VI_1},\, \theta_{VI_2},\, \theta_{VI_3},\, \dot{p}_{v_1},\, \dot{p}_{v_2},\, \dot{p}_{v_3},\, \dot{\theta}_{VI_1},\, \dot{\theta}_{VI_2},\, \dot{\theta}_{VI_3}\right\}^T,$$

due to their proximity to zero natural frequency. Selective modal analysis is carried out on the linear time-invariant system Eq.(15.7), where the state matrix A is a real $n \times n$ matrix assumed to have n distinct eigenvalues. The state matrix A may have complex eigenvalues, which are assured to appear in complex conjugate pairs. The corresponding eigenvectors $\{u_1,\, u_2,\, u_3, \ldots,\, u_n\}$ form a linearly independent eigenbasis in an n-dimensional complex space. Let the set of vectors representing the reciprocal basis be given by $\{v_1, v_2, v_3, \ldots,\, v_n\}$ such that

$$v_i^T u_j = \delta_{ij}, \qquad \forall\ \{i,\, j\} = 1,\, 2,\, 3,\, \ldots,\, n. \tag{16.1}$$

The unforced (open loop) response $x(t)$ of the system depends on the state variable vector, system's transient dynamics around the equilibrium, and the impulse applied at $t = 0$

$$x(t) = \exp(A\,t)\, x_0, \qquad \text{for } t \geq 0, \tag{16.2}$$

where $x(t)$ is a superposition of all the modal responses

$$x^{(i)}(t) = \exp(\lambda_i\, t)\, u_i v_i^T x_0, \qquad \text{for modes } i = 1,\, 2,\, 3, \ldots,\, n. \tag{16.3}$$

The vector $u_i v_i^T x_0$ is used to estimate the percent energy distribution among the state variables for the i^{th} mode due to a nonzero initial condition by computing element-wise percent magnitude of the vector. The resulting column vectors for all the other modes are stacked

Table 16.2: "Predominantly" axial-transvere vibration frequencies.

Free vibration frequency (rad/s)	Open-loop frequency (rad/s)
24.68151	$-0.210008 + j23.8296$
24.68151	$-0.210008 - j23.8296$
37.810596	$\mathbf{0.915295 + j55.0409}$
37.810596	$\mathbf{0.915295 - j55.0409}$
53.711302	$\mathbf{8.56901 + j72.8972}$
53.711302	$\mathbf{8.56901 + j72.8972}$
69.504044	-74.9713
69.504044	$-8.12703 + j77.192$
79.086391	$-8.12703 - j77.192$
79.086391	$\mathbf{6.92882 - j96.4825}$
93.51508	$\mathbf{6.92882 + j96.4825}$
93.51508	$-7.66359 + j102.625$
111.746287	$-7.66359 - j102.625$
111.746287	$\mathbf{119.267}$
123.390325	$\mathbf{0.323207 - j124.017}$
123.390325	$\mathbf{0.323207 + j124.017}$
135.48118	$\mathbf{7.30676 - j137.952}$
135.48118	$\mathbf{7.30676 + j137.952}$
151.72034	$-5.59079 + j147.4$
151.72034	$-5.59079 - j147.4$

together to form an $n \times n$ matrix, which we refer to as the percent modal participation factor (PMPF) matrix. Figures B.1 and B.2 present the percent modal participation factors (PMPF) for the "predominantly" rigid body modes. PMPF is a measure of the percent impact a given mode has on each of the 40 state variables.

Further, Table 16.2 presents a comparison between the axial-transverse free vibration modes and "predominatly" axial-transverse forced vibration modes. Note the jump in forced vibration frequency from mode 12 to 13 between Tables 16.1 and 16.2, where the frequency goes from 0.158458 rad/s to 23.8296 rad/s marking the end of predominantly rigid modes and the begining of flexible modes. Among flexible modes, the classification between "predominantly" axial-transverse and "predominantly" lateral-torsional modes is done by visually inspecting the PMPF distribution charts for the 28 flexible modes to follow. The frequency of the first "predominantly" axial-transverse mode is close to the first axial-transverse free vibration frequency. The forced vibration frequencies seem to follow the free vibration frequencies, where a few modes lag and a few modes lead. The modal energy associated with a given "predominantly" axial-transverse vibration mode is mostly distributed among those

Table 16.3: "Predominantly" lateral-torsional vibration frequencies.

Free vibration frequency (rad/s)	Open-loop frequency (rad/s)
54.05765	-78.3153
54.05765	$\mathbf{1.34903 - j91.6782}$
91.47149	$\mathbf{1.34903 - +j91.6782}$
91.47149	$\mathbf{112.376}$
130.27299	$\mathbf{6.40034 - j143.048}$
130.27299	$\mathbf{6.40034 + i143.048}$
168.28852	$-2.29565 - j167.122$
168.28852	$-2.29565 + j167.122$

modal coordinates representing such a motion during free vibration analysis:

$$\{\eta_1,\, \eta_2,\, \eta_3,\, \eta_5,\, \eta_6,\, \eta_8,\, \eta_9,\, \eta_{10},\, \eta_{12},\, \eta_{13},\, \dot{\eta}_1,\, \dot{\eta}_2,\, \dot{\eta}_3,\, \dot{\eta}_5,\, \dot{\eta}_6,\, \dot{\eta}_8,\, \dot{\eta}_9,\, \dot{\eta}_{10},\, \dot{\eta}_{12},\, \dot{\eta}_{13}\}^T.$$

Similarly, the states associated with "predominantly" lateral-torsional vibration modes are

$$\{\eta_4,\, \eta_7,\, \eta_{11},\, \eta_{14},\, \dot{\eta}_4,\, \dot{\eta}_7,\, \dot{\eta}_{11},\, \dot{\eta}_{14},\}^T.$$

Conclusions & Future Work

Chapter 17

Conclusions

Control-oriented modeling is expected to play a pivotal role in the design and development of future high speed aircraft. Design challenges to be encountered in the future stages will be dealt with early on in the design process in order to significantly reduce the cost involved. The present work develops a design framework ideal for integration with a multi disciplinary optimizer to carry out high-fidelity modeling of air-breathing hypersonic vehicles. Figure 17.1 presents an overview of the modeling framework developed, where design parameters are taken as inputs to compute free vibration mode shapes and natural frequencies, derive nonlinear equations of motion for the aircraft with respect to an inertial frame, estimate equilibrium configuration at the desired cruise altitude and Mach number, obtain linearized equations of motion about that equilibrium configuration, carry out open-loop stability analysis to study the aircraft's behavior about the chosen equilibrium, and finally design preliminary closed-loop control laws to keep the aircraft in that desired trajectory.

From the out set, the focus of this research has been to study the impact of high frequency vibration modes on the dynamics of a typical air-breathing hypersonic vehicle. In order to compute such high frequency modes for the purpose of modeling the overall dynamics of the aircraft, a novel scheme was developed that can compute higher vibration modes accurately. The scheme is described in Phase I and analysis on the effectiveness of this approach is conducted.

The nonlinear equations of motion derived in Phase III take into account longitudinal, lateral, and directional dynamics coupled with transverse and lateral bending, transverse and lateral shear, axial deformation, and torsion. Such a comprehensive flexible dynamical model for an air-breathing hypersonic vehicle hasn't been studied in the literature yet. Phase II describes the aerodynamic and control surface models used to compute the extreme aerodynamic loads experienced by the aircraft. These models have been inherited from the literature.

The nonlinear equations of motion derived are simplified by assuming that the aircraft is in steady state cruise condition. The associated equilibrium configuration is estimated in Phase IV and the nonlinear equations of motion are linearized about this equilibrium con-

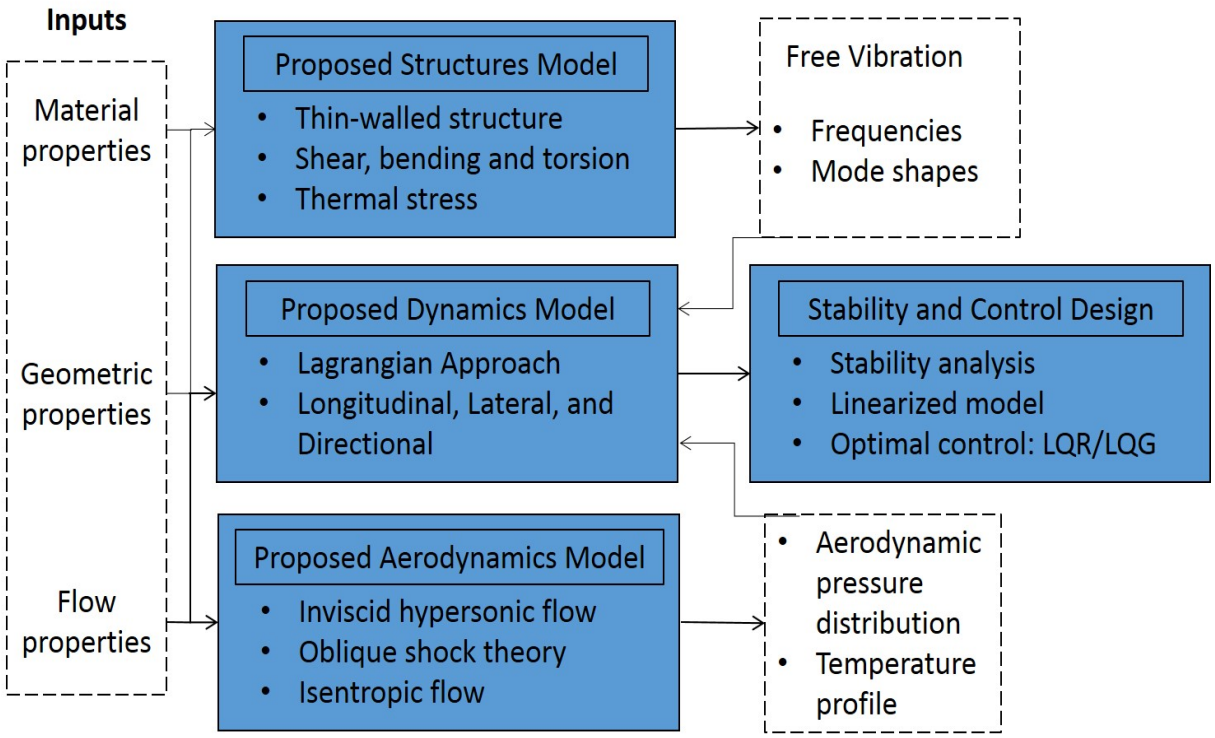

Figure 17.1: An overview of the control-oriented modeling framework.

dition. The linear system takes into consideration the dynamics due to 6 rigid body modes and 14 flexible modes, in first order form this leads to a 40×40 system. Further, open loop stability analysis is conducted where, the forced vibration frequencies are observed to follow the free vibration frequencies. Percent modal participation factors for the 40 modes is computed and the distribution of the modal energy among the 40 state variables is presented in the form of pie charts.

Chapter 18

Future Work

The framework developed has the potential to be transformed into a full fledged integrated control modeling and design tool that takes into account the flexibility effects on an air-breathing hypersonic vehicle due to aero-thermal loads. The present framework only takes into account the flexibility effects due to aerodynamic loads and the coupling that exists between the structure, the associated flow-field, and the control surfaces. This can be further extended to account for the flexibility effects due to thermal loads that turn out to be significant at such high speeds. The thermodynamic model to be implemented is presented in Appendix A.

As discussed earlier, a typical air-breathing hypersonic vehicle is expected to travel between two farthest land targets in less than two hours. Over such a high-speed, long range mission the total mass of the aircraft is reduced significantly (over 50%) and the average temperature gradually increases along the trajectory. The linearized equations of motion developed are valid for a constant mass and average temperature (when temperature effects are accounted for), which requires the linearized model to be parametrized in terms of these two slowly varying quantities. This system of parametrized equations will be used to develop efficient gain scheduling schemes to actively sabilize the aircraft. The expression for computing the instantaneous mass of the aircraft is

$$\begin{aligned} m(t) &= m_0 - \left(f_{st}\dot{m}_a\Phi\right)\, t, \\ &= m_0 - \left(f_{st}\frac{p_\infty}{RT_\infty}A_0 M_\infty c\left(T_\infty\right) l_{u_0}\Phi\right)\, t, \end{aligned} \tag{18.1}$$

and the effect of increase in average temperature can be accounted by solving for the sensitivities of the square of natural frequencies with respect to change in average temperature for all the significant free vibration modes modeled by solving the following modified Ritz

problem

$$\begin{aligned}\left(\omega^2\,[M]-[K_1]-[K_2]\,\Delta T_{avg}\right)C=0,\\ \left(\left(\frac{d\omega^2}{d\Delta T_{avg}}\right)[M]-[K_2]\right)C=0.\end{aligned}\tag{18.2}$$

The eigenvalues of the system (M, K_2) give us the sensitivities of the square of the natural frequencies for the first n significant modes with respect to change in average temperature. The intantaneous natural frequencies ω vector can be estimated element wise using

$$\omega^2=\omega_1^2+\left(\frac{d\omega^2}{d\Delta T_{avg}}\right)\Delta T_{avg},\tag{18.3}$$

where ω_1 represents one of the n eigenvalues of the initial Ritz problem

$$\left({\omega_1}^2\,[M]-K_1\right)C=0.\tag{18.4}$$

By incorporating the change in mass and average temperature through Eqs. (18.1) and (18.3), we have the parametrized system of linearized equations

$$M\,(m)\,\ddot{\delta q}+C\,\dot{\delta q}+K\,(m,\,\Delta T_{avg})\,\delta q=B\delta u\tag{18.5}$$

that can be used to implement gain scheduling over the entire trajectory.

However, a more pressing concern at this point is to develop a linear control strategy to compensate for the deviations from the perturbed trajectory. In this regard, output feedback control is considered as a more practical alternative as it doesn't involve full state feedback. Further, a linear quadratic gaussian control system will be designed to compensate for measurement and process noise. Alternatively, using a cascading H_∞ control may make the closed loop system robust.

Bibliography

[1] Lalith K. Abbas, Xiaoting Rui, P. Marzocca, M. Abdalla, and R. De. Breuker. Non-linear aero-thermo-visco-elastic behaviour of geometricaly imperfect curved skin panel: Flutter and post flutter analysis. In *50th AIAA/ASME/ASCE/AHS/ASC Structures, Structural Dynamics, and Materials Conference*, pages 1–17, Palm Springs, California, 2009.

[2] Randall J. Allemang. The modal assurance criterion – twenty years of use and abuse. *Journal of Sound and Vibration*, 37(8):14–23, 2003.

[3] N.S. Bardell. Chaldni figures for completely free parallelogram plates: An analytical study. *Journal of Sound and Vibration*, 174(5):655–676, 1994.

[4] R. B. Bhatt. Nature of stationarity of the natural frequencies at the natural modes in the rayleigh-ritz method. *Journal of Sound and Vibration*, 203(2):251–263, 1997.

[5] Robert D. Blevins. *Formulas for Natural Frequency and Mode Shape*. Van Nostrand Reinhold, New York, 1979.

[6] Michael A. Bolender. An overview on dynamics and controls modeling of hypersonic vehicles. In *2009 American Control Conference*, pages 1–6, St. Louis, MO, 2009.

[7] Michael A. Bolender and David B. Doman. Nonlinear longitudinal dynamical model of an air-breathing hypersonic vehicle. *Journal of Spacecraft and Rockets*, 44(2):374–387, 2007.

[8] Yang Chao, Li Guo Shu, and Wan Zhi Qiang. Aerothermal-aeroelastic two-way coupling method for hypersonic curved panel flutter. *Sci China Tech Sci*, 55, 2012.

[9] Frank R. Chavez and David K. Schmidt. Analytical aeropropulsive/aeroelastic hypersonic-vehicle model with dynamic analysis. *Journal of Guidance, Control, and Dynamics*, 17(6):1308–1319, 1994.

[10] Richard Colgren, Shahriar Keshmiri, and Maj Mirmirani. Nonlinear ten-degree-of-freedom dynamics model of a generic hypersonic vehicle. *Journal of Aircraft*, 46(3):800–813, 2009.

[11] Adam J. Culler, Trevor Williams, and Michael A. Bolender. Aerothermal modeling and dynamic analysis of a hypersonic vehicle. In *AIAA Atmospheric Flight Mechanics Conference and Exhibit*, pages 1–21, Hilton Head, South Carolina, 2007.

[12] H. Dal and O. K. Morgul. Vibrations of elastically restrained rectangular plates. *Scientific Research and Essays*, 6(34):6811–6816, 2011.

[13] Clarence W. de Silva. *Vibration: Fundamentals and Practice, Second Edition*. CRC Press, 2006.

[14] Zhou Ding. Natural frequencies of rectangular plates using a set of static beam functions in rayleigh-ritz method. *Journal of Sound and Vibration*, 189(1):81–87, 1996.

[15] E. H. Dowell. On asymptotic approximations to beam model shapes. *Journal of Applied Mechanics*, 51(2):439, 1984.

[16] Nathan J. Falkiewicz and Carlos E. S. Cesnik. A reduced-order modeling framework for integrated thermo-elastic analysis of hypersonic vehicles. In *50th AIAA/ASME/ASCE/AHS/ASC Structures, Structural Dynamics, and Materials Conference*, pages 1–18, Palm Springs, California, 2009.

[17] Nathan J. Falkiewicz, Carlos E. S. Cesnik, Michael A. Bolender, and David B. Doman. Thermoelastic formulation of a hypersonic vehicle control surface for control-oriented simulation. In *AIAA Guidance, Navigation, and Control Conference*, pages 1–18, Chicago, Illinois, 2009.

[18] Lisa Fiorentini, Andrea Serrani, Michael A. Bolender, and David B. Doman. Nonlinear control of a hypersonic vehicle with structural flexibility. In *47th IEEE Conference on Decision and Control*, pages 578–583, Cancun, Mexico, 2008.

[19] Lisa Fiorentini, Andrea Serrani, Michael A. Bolender, and David B. Doman. Robust nonlinear sequential loop closure control design for an air-breathing hypersonic vehicle model. In *American Control Conference 2008*, pages 3458–3463, Seattle, Washington, 2008.

[20] Lisa Fiorentini, Andrea Serrani, Michael A. Bolender, and David B. Doman. Nonlinear control of non-minimum phase hypersonic vehicle models. In *American Control Conference 2009*, pages 3160–3165, St. Louis, MO, 2009.

[21] A. Ghobarah and T. A. Baumber. Seismic behaviour of tall industrial masonry chimneys. In *Earthquake Engineering, Tenth World Conference*, pages 5043–5048, Balkema, Rotterdam, 1992.

[22] Herbert Goldstein, Charles Poole, and John Safko. *Classical Mechanics, Third Edition*. Addison Wesley, 2000.

[23] H. T. D. Grigg and Sivakumar B. J. Gallacher. Efficient parametric optimisation of support loss in mems beam resonators via an enhanced rayleigh-ritz method. In *Modern Practice in Stress and Vibration Analysis 2012*, pages 1–6, Glasgow, UK, 2012.

[24] P. Hagedorn. The rayleigh-ritz method with quasi-comparison functions in nonself-adjoint problem. *Transactions of the ASME, Journal of Vibration and Acoustics*, 115(3):280–284, 1993.

[25] J. W. Jaworski and E. H. Dowell. Free vibration of a cantilevered beam with multiple steps: Comparison of several theoretical methods with experiment. *Journal of Sound and Vibration*, 312(4):713–725, 2008.

[26] Shahriar Keshmiri. Nonlinear and linear longitudinal and lateral-directional dynamical model of air-breathing hypersonic vehicle. In *15th AIAA International Space Planes and Hypersonic Systems and Technologies Conference*, pages 1–24, Dayton, Ohio, 2008.

[27] Ryan J. Klock and Carlos E.S. Cesnik. Aerothermoelastic simulation of air-breathing hypersonic vehicles. In *55th AIAA/ASME/ASCE/AHS/ASC Structures, Structural Dynamics, and Materials Conference*, pages 1–16, 2014.

[28] Chalitphan Kunaporn, Mahendra P. Singh, Mayuresh J. Patil, and Rakesh K. Kapania. Analysis of thin-walled beam with crack of random location and size. *AIAA Journal*, 50(6):1265–1280, 2012.

[29] Chalitphan Kunaporn, Mahendra P. Singh, Mayuresh J. Patil, and Rakesh K. Kapania. Aeroelastic divergence of a randomly cracked thin-walled beam. *Journal of Aircraft*, 51(2):390–401, 2014.

[30] Wen L. Li. Free vibrations of beams with general boundary conditions. *Journal of Sound and Vibration*, 237(4):709–725, 2000.

[31] Wen L. Li. Vibration analysis of rectangular plates with general elastic boundary supports. *Journal of Sound and Vibration*, 273(3):619–635, 2004.

[32] A. G. J. MacFarlane. Use of power and energy concepts in the analysis of multivariable feedback controllers. *Proceedings of the Institution of Electrical Engineers*, 116(8):1449–1452, 1969.

[33] Jack J. McNamara, Adam J. Culler, and Andrew R. Crowell. Aerothermoelastic modeling considerations for hypersonic vehicles. In *16th AIAA/DLR/DGLR International Space Planes and Hypersonic Systems and Technologies Conference*, pages 1–38, Bremen, Germany, 2009.

[34] Jack J. McNamara and Peretz P. Friedmann. Aeroelastic and aerothermoelastic analysis of hypersonic vehicles: Current status and future trends. In *48th AIAA/ASME/ASCE/AHS/ASC Structures, Structural Dynamics, and Materials Conference*, pages 1–55, Honolulu, Hawaii, 2007.

[35] Leonard Meirovitch. *Computational Methods in Structural Dynamics*. Sijhoff & Noodhoff, Alphen aan den Rijin, the Netherlands, 1980.

[36] Leonard Meirovitch and P. Hagedorn. A new approach to the modelling of distributed non-self adjoint systems. *Journal of Sound and Vibration*, 178(2):227–241, 1994.

[37] Leonard Meirovitch and Moon K. Kwak. Convergence of the classical rayleigh-ritz method and the finite element method. *AIAA Journal*, 28(8):1509–1516, 1990.

[38] Leonard Meirovitch and Moon K. Kwak. On the modelling of flexible multi-body systems by the rayleigh-ritz method. In *AIAA Dynamics Specialist Conference*, pages 517–526, Long Beach, CA, USA, 1990.

[39] Leonard Meirovitch and Moon K. Kwak. Inclusion principle for the rayleigh-ritz based substructure synthesis. *AIAA Journal*, 30(5):1344–1351, 1992.

[40] L. E. Monterrubio and S. Illanko. Proof of convergence for a set of admissible functions for the rayleighritz analysis of beams and plates and shells of rectangular planform. *Journal of Computers & Structures*, 147:236–243, 2015.

[41] Theodore G. Mordfin and Sivakumar S. K. Tadikonda. Modeling controlled articulated flexible systems using assumed modes - part i: Theory. In *Proceedings of the ASME Design Engineering Technical Conference*, pages 383–390, Pittsburgh, PA, USA, 2001.

[42] J . E. Van Ness, F. M. Brasch, G. L. Landgren, and S. T. Naumann. Analytical investigation of dynamic instability occuring at powerton station. *IEEE Transactions on Power Apparatus and Systems*, (4):1386–1395, 1980.

[43] Ashok Kumar Pandey and Rudra Pratap. Effect of flexural modes on squeeze film damping in mems cantilever resonators. *Journal of Micromechanics and Microengineering*, 17(12):2475–2484, 2007.

[44] Armando A. Rodriguez, Jeffery J. Dickeson, Oguzhan Cifdaloz, Robert McCullen, Jose Benavides, Srikanth Sridharan, Atul Kelkar, Jeral M. Vogel, and Don Soloway. Modeling and control of scramjet-powered hypersonic vehicles: Challenges, trends, & tradeoffs. In *AIAA Guidance, Navigation and Control Conference and Exhibit*, pages 1–40, Honolulu, Hawaii, 2008.

[45] M.B. Rosales and C.P. Filipich. Vibration of orthotropic plates: Discussion on the completeness of the solutions used in direct methods. *Journal of Sound and Vibration*, 261:751–757, 2003.

[46] Melvin R. Scott and Herman A. Watts. Computational solution of linear two-point boundary value problems via orthonormalization. *SIAM Journal of Numerical Analysis*, 14(1):40–70, 1977.

[47] David O. Sigthorsson, Pete Jankocsky, Andrea Serrani, Stephen Yurkovich, Michael A. Bolender, and David B. Doman. Robust linear output feedback control of an air-breathing hypersonic vehicle. volume 31, pages 1052–1066, 2008.

[48] David O. Sigthorsson, A. Serrani, Michael A. Bolender, and David B. Doman. Lpv control design for over-actuated hypersonic vehicles models. In *AIAA Guidance, Navigation, and Control Conference*, pages 1–24, Chicago, Illinois, 2009.

[49] Sarvesh Singhvi and Rakesh K. Kapania. Comparison of simple and chebychev polynomials in rayleigh-ritz analysis. *Journal of Engineering Mechanics*, 120(10):2126–2135, 1994.

[50] Martin Sippel and Josef Klevanski. Preliminary definition of supersonic and hypersonic airliner configuration. In *14th AIAA/AHI Space Planes and Hypersonic Systems and Technology Conference*, pages 1–17, 2006.

[51] Lawrence B. Smith. Measurement of winds between 100, 000 and 300, 000 ft by use of chaff rockets. *Journal of Meteorology*, 17, 1960.

[52] Ryan P. Starkey, Danny D. Liu, P. C. Chen, Ayan Sengupta, K. T. Chang, and Falcon Rankins. Integrated aero-servo-thermo-propulso-elasticity (astpe) methodology for hypersonic scramjet vehicle design/analysis. In *48th AIAA Aerospace Sciences Meeting Including the New Horizons Forum and Aerospace Exposition*, pages 1–23, Orlando, Florida, 2010.

[53] Praneeth Reddy Sudalagunta, Cornel Sultan, Rakesh K. Kapania, Layne T. Watson, and Pradeep Raj. A novel scheme to accurately compute higher vibration modes using the ritz method and a two-point bvp solver. In *56th AIAA/ASCE/AHS/ASC Structures, Structural Dynamics, and Materials Conference*, pages 1–18, Kissimmee, Florida, 2015.

[54] Sean M. Torrez, James F. Driscoll, Michael A. Bolender, Michael W. Oppenheimer, and David B. Doman. Effects of improved propulsion modeling on the flight dynamics of hypersonic vehicles. In *AIAA Atmospheric Flight Mechanics Conference and Exhibit*, pages 1–22, Honolulu, Hawaii, 2008.

[55] George C. Varghese, Ignaci0 C. Perez-Arriaga, and Fred C. Schweppe. Selective modal analysis with applications to electric power systems, part i: Heuristic introduction. *IEEE Transactions on Power Apparatus and Systems*, (9):3117–3125, 1982.

[56] K. P. Venkatesh and Rudra Pratap. Capturing higher modes of vibration of micromachined resonators. In *Journal of Physics: Conference Series 181 012079*, pages 5043–5048, 2009.

[57] Tyler J. Vick, Jonathan A. Muse, and Michael A. Bolender. Hypersonic vehicle model generator for masiv. In *AIAA Modeling and SImulation Technologies Conference*, pages 1–38, Minneapolis, Minnesota, 2012.

[58] J. M. Vogel, A. G. Kelkar, G. Inger, C. Whitmer, A. Sidlinger, and A. Rodriguez. Control-relevant modeling of hypersonic vehicles. In *2009 American Control Conference*, pages 1–6, St. Louis, MO, 2009.

[59] Randall T. Voland, Lawrence D. Huebner, and Charles R. McClinton. X-43a hypersonic vehicle technology development. *Acta Astronautica*, 59, 2006.

[60] Donald T. Ward and Thomas W. Stragnac. *Introduction to Flight Test Engineering.* Kendall Hunt Publishing, Iowa, 2006.

Appendix:

Appendix A

Thermal Loads

A typical air-breathing hypersonic vehicle may cruise at a Mach number ranging from $5-10$, depending on its mission profile. At such high speeds, the aircraft will experience extreme aerodynamic and thermal loads that cause significant flexing of the airframe. These loads are a consequence of the associated flow field over the aircraft characterized by extreme and sudden changes in flow properties such as pressure, temperature, density, etc. under the influence of incident shock waves and due to the viscous/skin friction effects. In the present analysis the aerodynamic and thermal loads are assumed to be caused only due to the former, while the skin friction effects, although considerable, have been neglected from the present analysis. The thermal loads are modeled as equivalent forces and moments of a rigid cross section in order to facilitate their direct inclusion in the equations of motion.

The airframe modeled as a monocoque, thin-walled structure under the assumption that plane sections remain plane but not necessarily perpendicular to the longitudinal axis is an effort to idealize an aircraft fuselage with internal support structures such as frames and ribs to ensure that the in-plane strains are zero. It is assumed that these support structures prevent thermal loads to result in axial or tangential strains.

Consider a cylindrical coordinate system $(r,\, \theta,\, x_1)$, the strain-displacement relations are

$$\epsilon_{11} = \frac{\partial u_1}{\partial x_1}, \qquad \gamma_{r\theta} = \frac{1}{r}\frac{\partial u_r}{\partial \theta} + \frac{\partial u_\theta}{\partial r} - \frac{u_\theta}{r},$$

$$\epsilon_{rr} = \frac{\partial u_r}{\partial r}, \qquad \gamma_{r1} = \frac{\partial u_1}{\partial r} + \frac{\partial u_r}{\partial x_1},$$

$$\epsilon_{\theta\theta} = \frac{u_r}{r} + \frac{1}{r}\frac{\partial u_\theta}{\partial \theta}, \qquad \gamma_{r\theta} = \frac{1}{r}\frac{\partial u_1}{\partial \theta} + \frac{\partial u_\theta}{\partial x_1}.$$

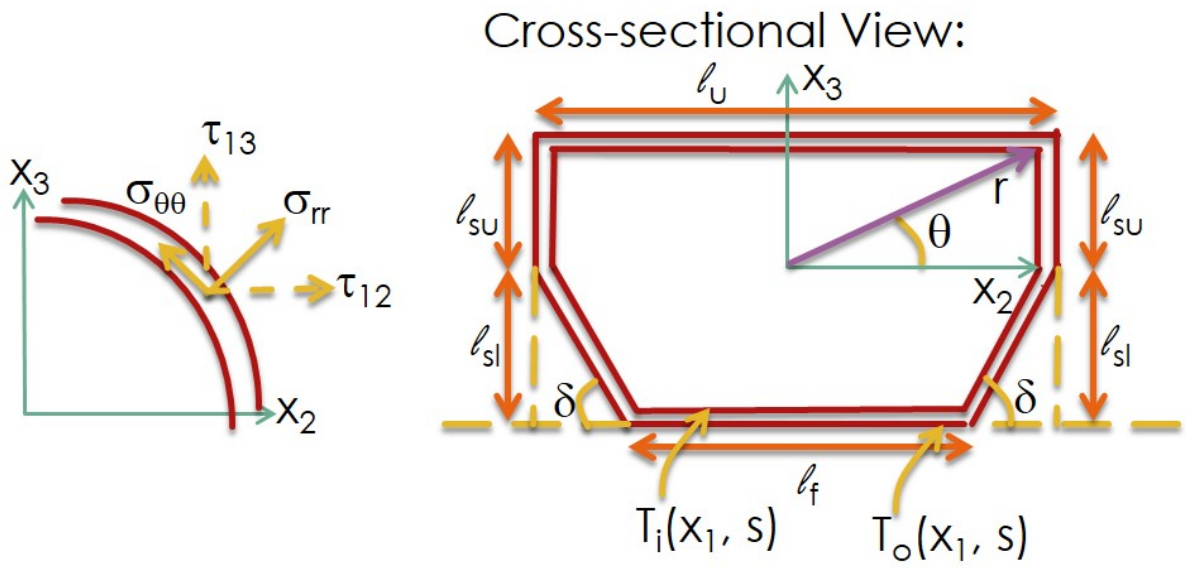

Figure A.1: Cross-sectional view of the air-breathing hypersonic vehicle with the inner and outer wall temperatures.

The stress-strain relations are

$$\begin{aligned} \sigma_{rr} &= \lambda(\epsilon_{rr} + \epsilon_{\theta\theta} + \epsilon_{11}) + 2\mu\epsilon_{rr}, & \tau_{r\theta} &= \mu\gamma_{r\theta}, \\ \sigma_{\theta\theta} &= \lambda(\epsilon_{rr} + \epsilon_{\theta\theta} + \epsilon_{11}) + 2\mu\epsilon_{\theta\theta}, & \tau_{r1} &= \mu\gamma_{r1}, \\ \sigma_{11} &= \lambda(\epsilon_{rr} + \epsilon_{\theta\theta} + \epsilon_{11}) + 2\mu\epsilon_{11}, & \tau_{1\theta} &= \mu\gamma_{1\theta}. \end{aligned}$$

Under the assumption of internal support structures the only nonzero strain component is radial strain

$$\epsilon_{rr}(x_1, s) = \alpha(x_1)\left(T_o(x_1, s) - T_i(x_1, s)\right), \tag{A.1}$$

where α is the coefficient of thermal conductivity, $T_o(x_1, s)$ is the temperature profile on the outer wall, $T_i(x_1, s)$ is the temperature profile on the inner wall, and s is a piecewise linear coordinate along the circumference of the cross-section. This assumption significantly simplifies the analysis and results in

$$\sigma_{rr} = (\lambda + 2\mu)\epsilon_{rr}, \tag{A.2}$$
$$\sigma_{\theta\theta} = \lambda\epsilon_{rr}, \tag{A.3}$$
$$\sigma_{11} = \lambda\epsilon_{rr}. \tag{A.4}$$

Further, from Fig. A.1 the expressions for the out of plane shear stresses τ_{12} and τ_{13} can be obtained as

$$\tau_{12} = \sigma_{rr}\left(\frac{\partial x_3}{\partial s}\right) + \sigma_{\theta\theta}\left(\frac{\partial x_2}{\partial s}\right), \tag{A.5}$$

$$\tau_{13} = -\sigma_{rr}\left(\frac{\partial x_2}{\partial s}\right) + \sigma_{\theta\theta}\left(\frac{\partial x_3}{\partial s}\right), \tag{A.6}$$

where, the gradient terms in these expressions are piecewise constants in the piecewise linear coordinate, s. When integrated over the circumference these gradient terms would come out of the various piecewise integrals, thus simplifying the computation of forces and moments. The five thermal stresses listed in Eqs. (A.2) - (A.6) are used to compute the equivalent forces and moments acting on the rigid cross section

$$N_{1T}(x_1) = \int_{\mathcal{C}} \sigma_{11}(x_1,\, s)\, t(x_1)\, ds, \qquad M_{1T}(x_1) = \int_{\mathcal{C}} \sigma_{\theta\theta}(x_1,\, s)\, r(x_1,\, s)\, t(x_1)\, ds,$$

$$V_{2T}(x_1) = \int_{\mathcal{C}} \tau_{12}(x_1,\, s)\, t(x_1)\, ds, \qquad M_{2T}(x_1) = \int_{\mathcal{C}} x_3\, \sigma_{11}(x_1,\, s)\, t(x_1)\, ds,$$

$$V_{3T}(x_1) = \int_{\mathcal{C}} \tau_{13}(x_1,\, s)\, t(x_1)\, ds, \qquad M_{3T}(x_1) = \int_{\mathcal{C}} x_2\, \sigma_{11}(x_1,\, s)\, t(x_1)\, ds,$$

where N_{1T}, N_{2T}, N_{3T} are axial forces along x_1, x_2, x_3 respectively, M_{1T}, M_{2T}, M_{3T} are moments about x_1, x_2, x_3 respectively, and V_{2T}, V_{3T} are out of plane shear forces. These forces on the rigid cross section can be used to compute virtual work due to external forces. The present model does not include thermal loads at this moment. However, the existing codes have a provision to include these effects in the model.

Appendix B

Percent Modal Participation Factors

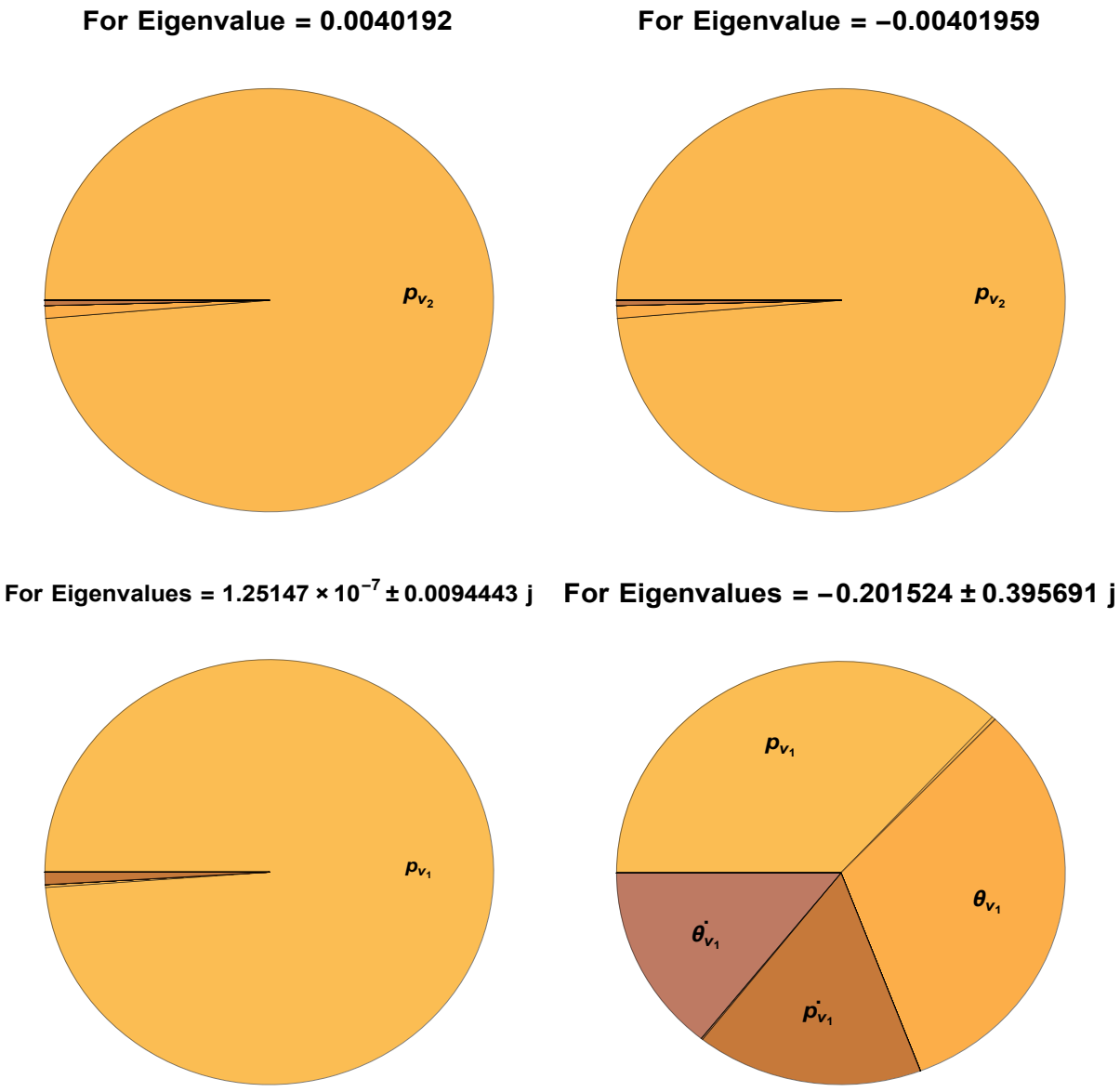

Figure B.1: Percentage modal participation factors for the "predominantly" rigid body modes 1 to 6.

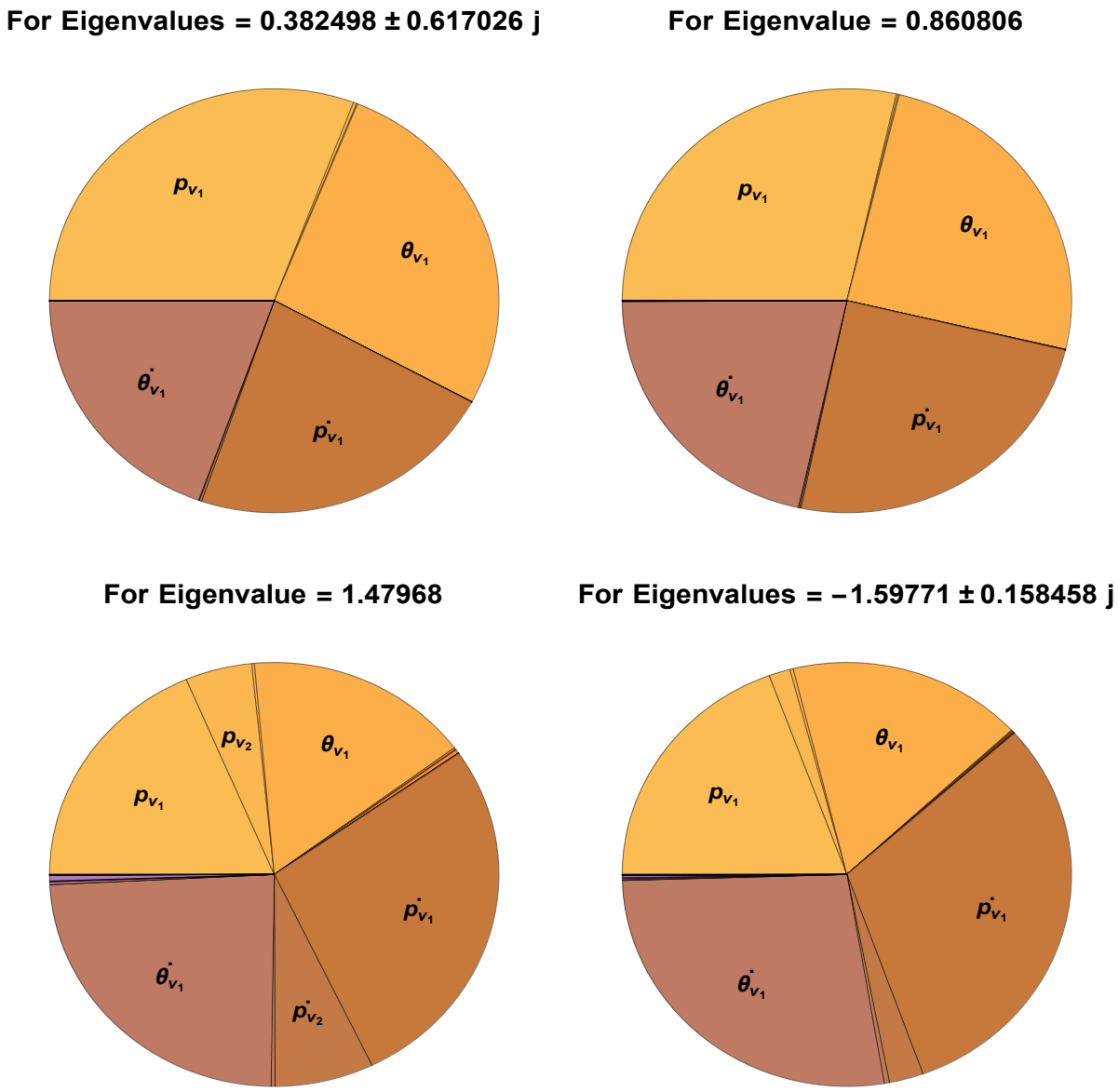

Figure B.2: Percentage modal participation factors for the "predominantly" rigid body modes 7 to 12.

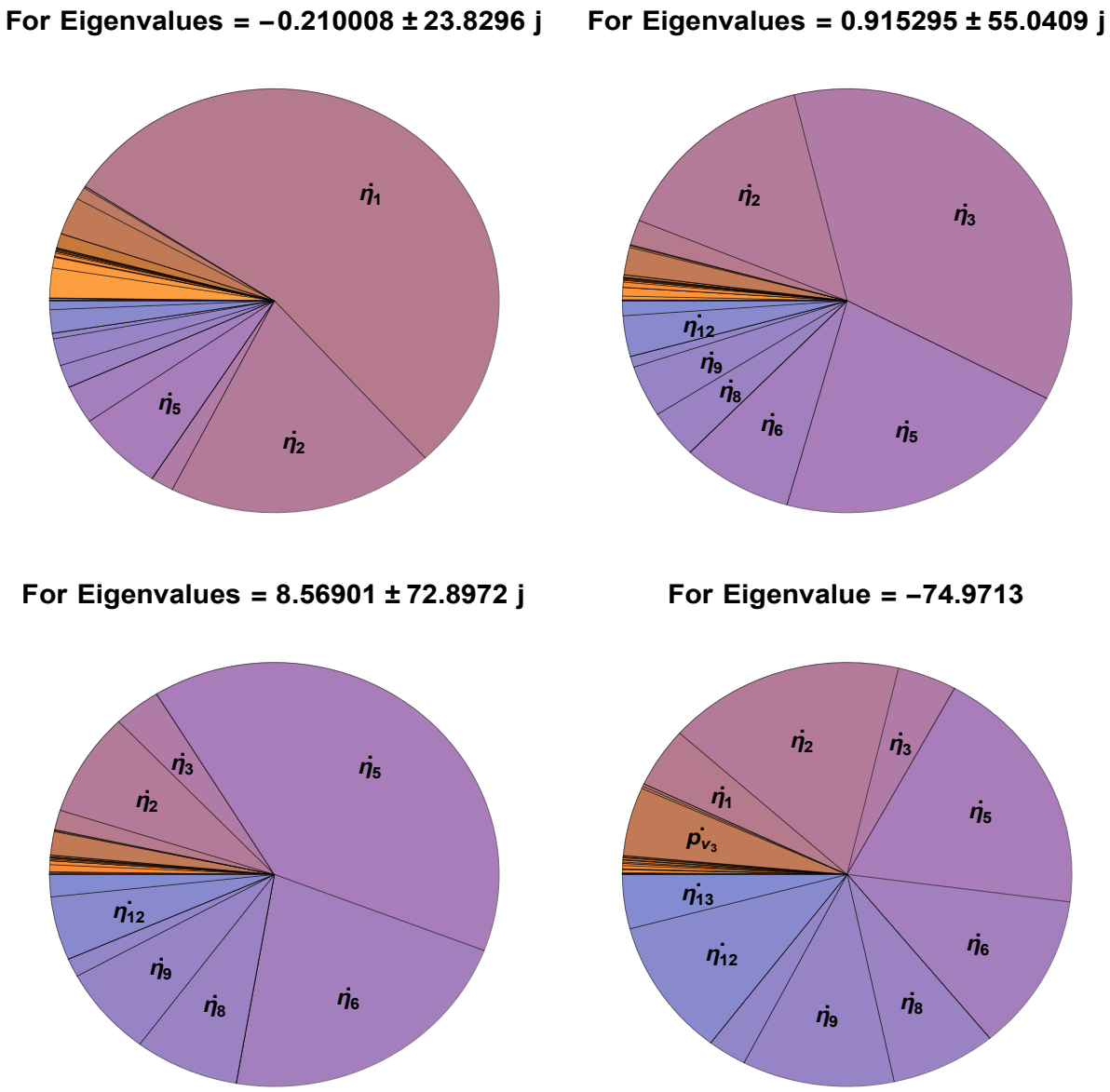

Figure B.3: Percentage modal participation factors for the "predominantly" axial-transverse vibration modes 13 to 19.

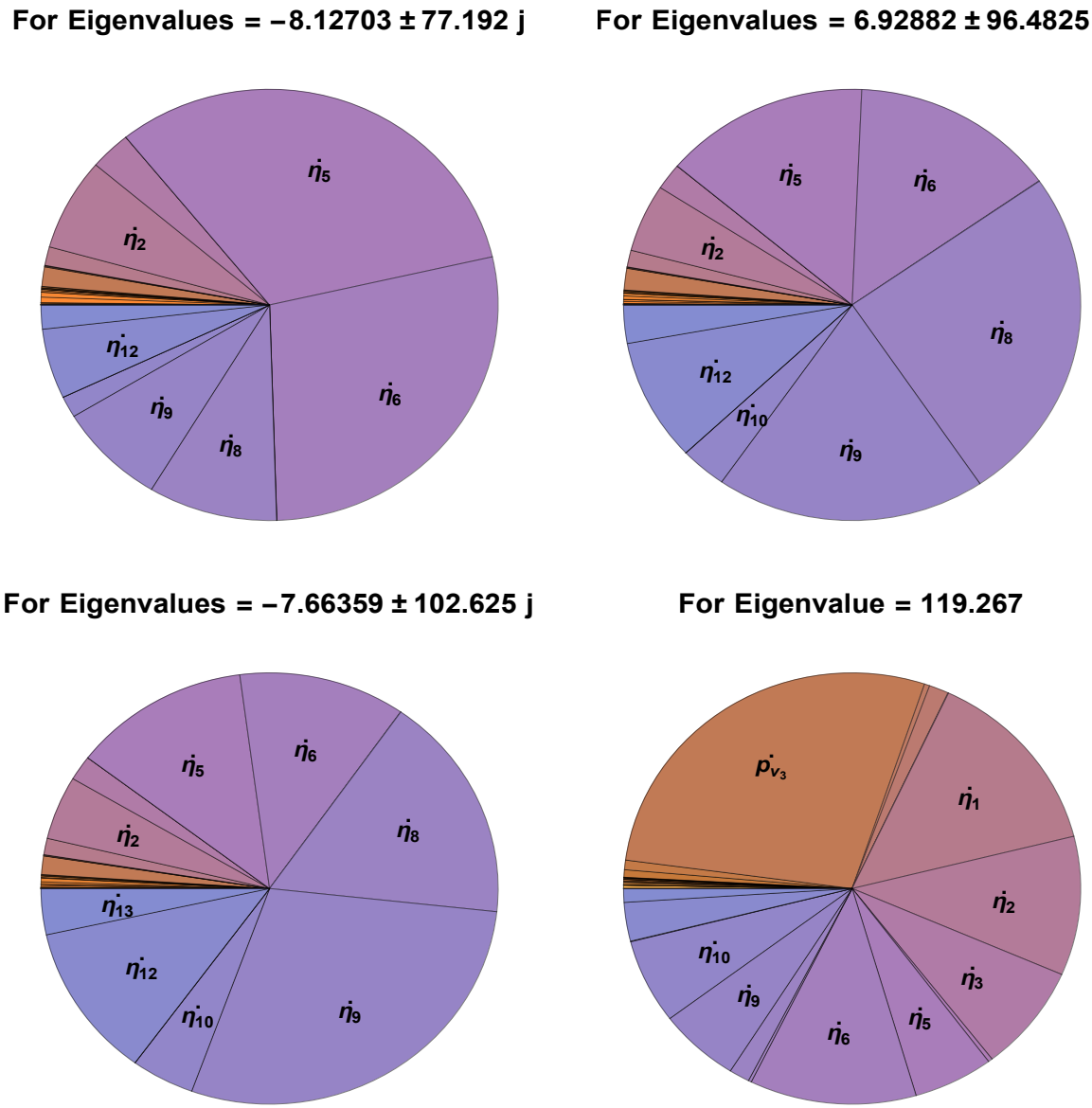

Figure B.4: Percentage modal participation factors for the "predominantly" axial-transverse vibration modes 20, 21, 25, 26, 27, 28, and 30.

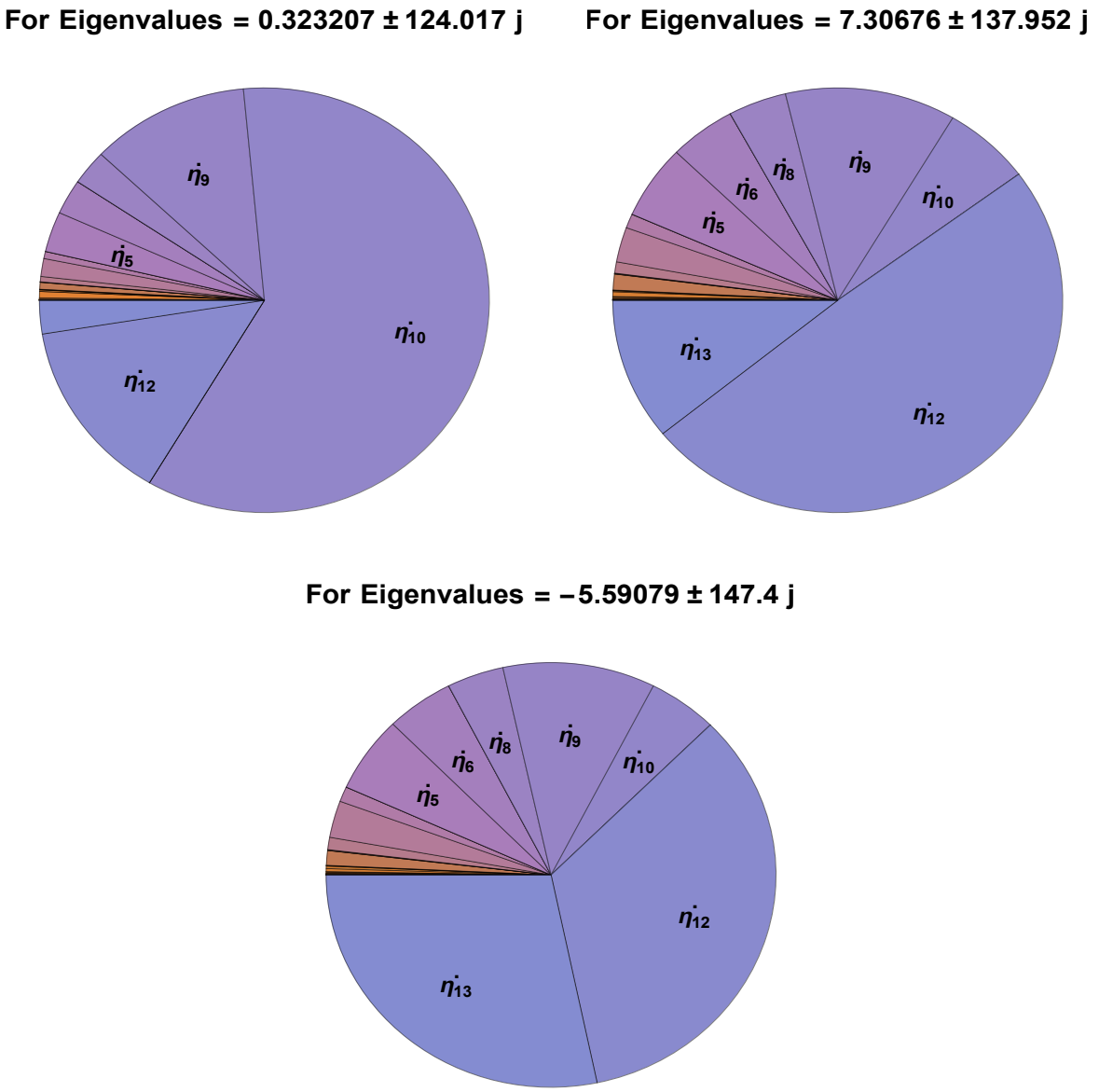

Figure B.5: Percentage modal participation factors for the "predominantly" axial-transverse vibration modes 31, 32, 33, 34, 37, and 38.

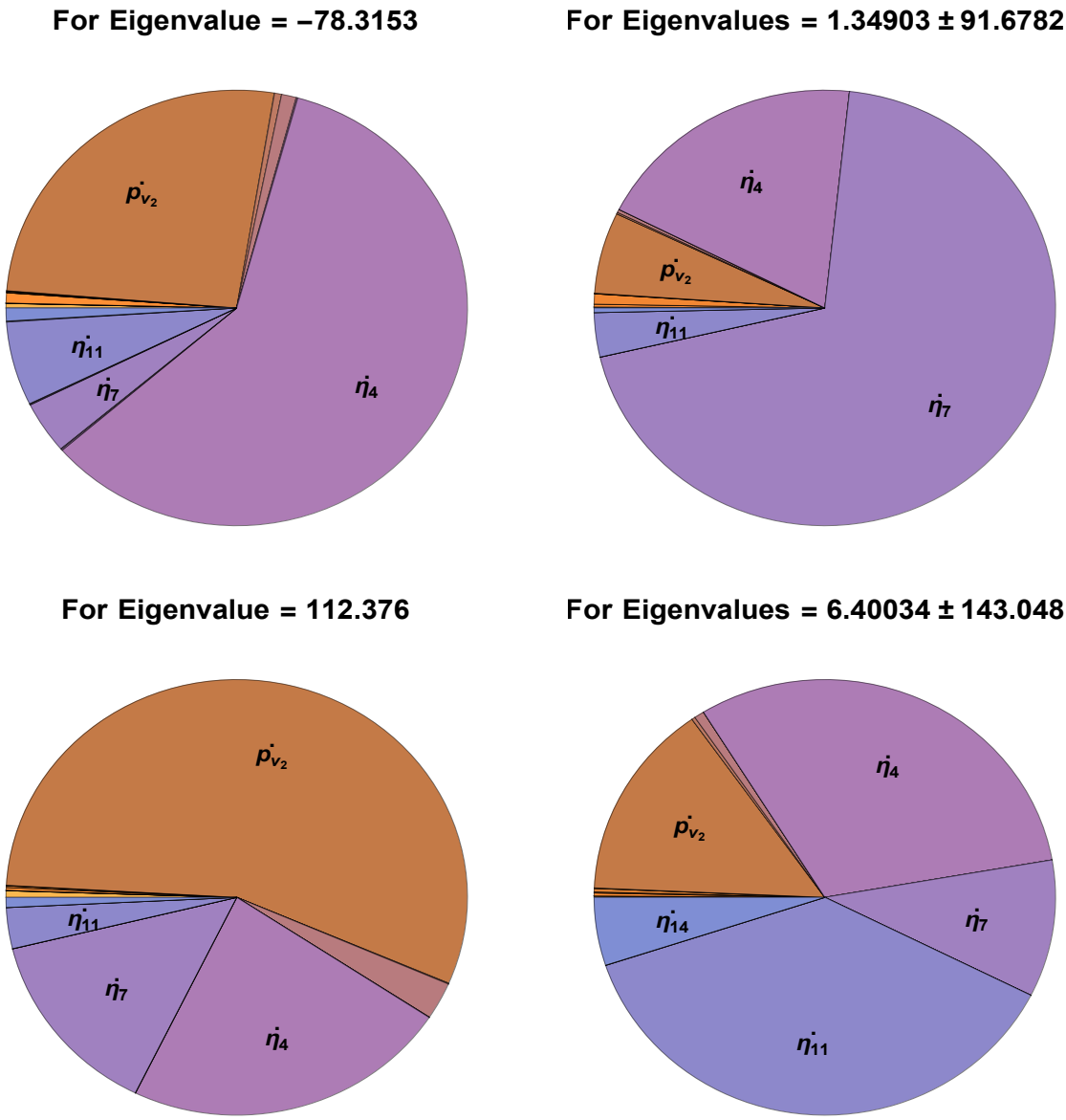

Figure B.6: Percentage modal participation factors for the "predominantly" lateral-torsional vibration modes 22, 23, 24, 29, 35, and 36.

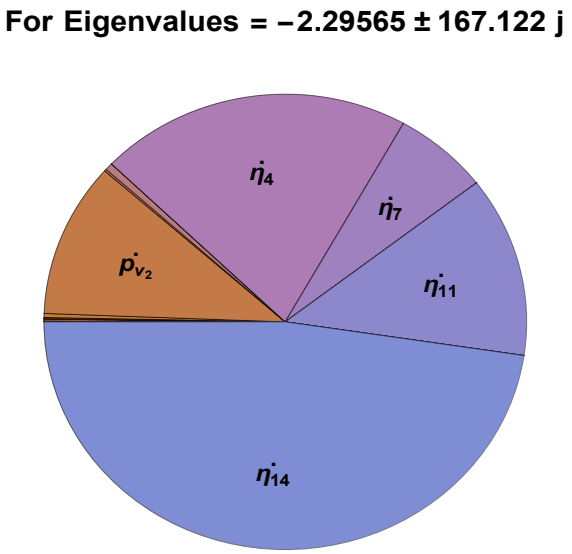

Figure B.7: Percentage modal participation factors for the "predominantly" lateral-torsional vibration modes 39 and 40.